Cu_2O thin films for p-type metal oxide thin film transistors

Sanggil Han

Department of Engineering
University of Cambridge

This dissertation is submitted for the degree of
Doctor of Philosophy

Darwin College November 2018

Declaration

I hereby declare that except where specific reference is made to the work of others, the contents of this dissertation are original and have not been submitted in whole or in part for consideration for any other degree or qualification in this, or any other university. This dissertation is the result of my own work and includes nothing which is the outcome of work done in collaboration except where specifically indicated in the text. In accordance with the Department of Engineering guidelines, this dissertation does not exceed 65,000 words including references, tables and equations, and it contains less than 150 figures.

Sanggil Han

November 2018

Acknowledgements

I remain ever grateful to my supervisor, Prof. Andrew Flewitt, for broadening my perspective for scientific work and his encouragement throughout my PhD. I am grateful for having been a member of his research group in Cambridge.

I am indebted to Dr. Kham Niang and Dr. Girish Rughoobur. They helped me a great deal, particularly when I was first starting out, and trained me how to use various deposition and characterisation techniques.

I would also like to thank all the wonderful people outside of work who have helped make the last 3 years in Cambridge so enjoyable. My friends (Myungun Kim, Alex Young Il Seo, Jisu Cho, Minkyung Kim, Youngchan Park, and many others) especially have kept me laughing and kept me inspired. I hope that I can repay all of your kindness and spend more time with all of you.

Finally, I am ever grateful to my parents, Moonsoo Han and Heseon Ha, for their continued belief and support, and, of course, my wife, Seonmin Won. Without her love and support, none of this would have been possible.

This work was supported by the Engineering and Physical Sciences Research Council under Grant No. EP/M013650/1.

Abstract

The rapid progress of n-type metal oxide thin film transistors (TFTs) has motivated research on p-type metal oxide TFTs in order to realise metal oxide-based CMOS circuits which enable low power consumption large-area electronics. Cuprous oxide (Cu_2O) has previously been proposed as a suitable active layer for p-type metal oxide TFTs. The two most significant challenges for achieving good quality Cu_2O TFTs are to overcome the low field-effect mobility and an unacceptably high off-state current that are a feature of devices that have been reported to date. This dissertation focuses on improving the carrier mobility, and identifying the main origins of the low field-effect mobility and high off-state current in Cu_2O TFTs.

This work has three major findings. The first major outcome is a demonstration that vacuum annealing can be used to improve the carrier mobility in Cu_2O without phase conversion, such as oxidation (CuO) or oxide reduction (Cu). In order to allow an in-depth discussion on the main origins of the very low carrier mobility in as-deposited films and the mobility enhancement by annealing, a quantitative analysis of the relative dominance of the main conduction mechanisms (i.e. trap-limited and grain-boundary-limited conduction) is performed. This shows that the low carrier mobility of as-deposited Cu_2O is due to significant grain-boundary-limited conduction. In contrast, after annealing, grain-boundary-limited conduction becomes insignificant due to a considerable reduction in the energy barrier height at grain boundaries, and therefore trap-limited conduction dominates. A further mobility improvement by an increase in annealing temperature is explained by a reduction in the effect of trap-limited conduction resulting from a decrease in tail state density.

The second major outcome of this work is the observation that grain orientation ([111] or [100] direction) of sputter-deposited Cu_2O can be varied by control of the incident ion-to-Cu flux ratio. Using this technique, a systematic investigation on the effect of grain orientation on carrier mobility in Cu_2O thin films is presented, which shows that the [100] Cu_2O grain orientation is more favourable for realising a high carrier mobility.

In the third and final outcome of this thesis, the temperature dependence of the drain current as a function of gate voltage along with the C-V characteristics reveals that minority carriers (electrons) cause the high off-state current in Cu_2O TFTs. In addition, it is observed that an abrupt lowering of the activation energy and pinning of the Fermi energy occur in the off-state, which is attributed to subgap states at 0.38 eV below the conduction band minimum.

These findings provide readers with the understanding of the main origins of the low carrier mobility and high off-state current in Cu_2O TFTs, and the future research direction for resolving these problems.

List of publications

Most of this dissertation has been published as seen in the publication list.

International journals

Sanggil Han, Kham M. Niang, Girish Rughoobur and Andrew J. Flewitt, "Effects of post-deposition vacuum annealing on film characteristics of p-type Cu_2O and its impact on thin film transistor characteristics,"
Applied Physics Letters **109**, 173502 (2016).

Sanggil Han and Andrew J. Flewitt, "Analysis of the conduction mechanism and copper vacancy density in p-type Cu_2O thin films,"
Scientific Reports **7**, 5766 (2017).

Sanggil Han and Andrew J. Flewitt, "The origin of the high off-state current in p-type Cu_2O thin film transistors,"
IEEE Electron Device Letters **38** (10), 1394 (2017).

Sanggil Han and Andrew J. Flewitt, "Control of grain orientation and its impact on carrier mobility in reactively sputtered Cu_2O thin films,"
Manuscript in preparation.

Conference

Sanggil Han and Andrew J. Flewitt, "The effects of post-deposition vacuum annealing temperature on electrical characteristics of p-type Cu_2O thin film transistors,"
Presented at European Materials Research Society (E-MRS), Lille, France, May 2-6 (2016)

Contents

List of figures

List of tables

List of abbreviations and symbols

Abbreviations

Abbreviation	**Description**
CBM	Conduction band minimum
CMOS	Complementary metal-oxide-semiconductor
cps	Counts per sec
C-V	Capacitance-voltage
DC	Direct current
DFT	Density functional theory
DI	Deionised
FWHM	Full width at half maximum
GLC	Grain-boundary-limited conduction
HiTUS	High target utilisation sputtering
ICP	Inductively coupled plasma
IPA	Isopropyl alcohol
IR	Infrared
JCPDS	Joint committee on powder diffraction standards
LO	Longitudinal optical
MN	Meyer-Neldel
RF	Radio frequency
sccm	Standard cubic centimetres per minute

S/D	Source/drain
SEM	Scanning electron microscopy
SPM	Sulphuric acid and hydrogen peroxide mixture ($H_2SO_4 + H_2O_2$)
TFTs	Thin film transistors
TLC	Trap-limited conduction
TLM	Transmission line method
TO	Transverse optical
UV	Ultraviolet
VBM	Valence band maximum
VRH	Various range hopping
XPS	X-ray photoelectron spectroscopy
XRD	X-ray diffraction

Symbols

Symbol	Description	Unit
Al	Aluminium	
Ar	Argon	
Au	Gold	
α	Optical absorption coefficient	cm^{-1}
α_0	Prefactor of the photon energy-dependent α equation	cm^{-1}
α_{GLC}	GLC coefficient	
β	FWHM corrected by $(\beta_m^2 - \beta_i^2)^{1/2}$	rad
β_m, β_i	Measured and instrumental FWHM	rad

β_{TLC}	Ratio of p_{free} to $p_{free}+p_{trap}$	
β_{TLC0}, β_{TLC500}, β_{TLC600}, β_{TLC700}	β_{TLC} before and after annealing at 500, 600 and 700 ℃	
C_i	Gate insulator capacitance per unit area	F/cm^2
Cu, CuO, Cu_2O	Copper, Cupric oxide, Cuprous oxide	
Cu_i	Copper interstitials	
D_{it}	The area density of traps at the channel/gate insulator interface	cm^{-2}·eV^{-1}
E_a	Activation energy	eV
E_B	Potential energy barrier height at grain boundaries	eV
E_C	Energy at the bottom of the conduction band	eV
E_F	Fermi energy	eV
E_{F0}, E_{F500}, E_{F600}, E_{F700}	E_F before and after annealing at 500, 600 and 700 ℃	eV
E_g	Band gap energy	eV
E_g^{opt}	Optical band gap	eV
E_u	Urbach energy	eV
E_V	Energy at the top of the valence band	eV
$E_{V_{Cu}}$	Energy level of copper vacancies	eV
ε_0	Vacuum permittivity (8.854×10^{-14})	F/cm
ε_{Cu2O}	Cu_2O dielectric constant (7.5 at 293 K)	
Φ_b	Cu_2O bulk potential, $\Phi_b=\{E_g/2-(E_F-E_V)\}/q$	V
Φ_B	Schottky barrier height	eV
Φ_m	Metal work function	eV
$F(E)$	Fermi-Dirac distribution function	
g_A	Acceptor-site degeneracy factor	

h	Planck’s constant (4.135667662×10^{-15})	eV·s
$h\upsilon$	Photon energy	eV
I_{DS}	Drain-source current per unit channel width	A/μm
I_{D0}	Prefactor of the temperature-dependent I_{DS} equation	A/μm
IGZO	Indium gallium zinc oxide	
χ_s	Semiconductor electron affinity	eV
k	Boltzmann constant (8.617×10^{-5})	eV/K
kT	Thermal energy (~26 at 300 K)	meV
kT_t	Tail state energy	eV
L	Channel length of TFTs	μm
L_g	Grain size	nm
l	Distance between localised states (i.e. hopping sites)	nm
l_0	Extension of the wavefunction	nm
λ	X-ray wavelength of Cu K$_{\alpha1}$ radiation (0.154)	nm
υ	Photon frequency	s^{-1}
ν_0	Attempt-to-escape frequency from localised states	s^{-1}
m_0	Electron rest mass (9.10938356×10^{-31})	kg
m_h^*	The density-of-states effective mass of holes	kg
m_{lh}	Band mass of light holes	kg
μ_{FE}	Field-effect mobility	cm^2/V·s
$\mu_{i,FE}$	Intrinsic channel field-effect mobility corrected for R_C	cm^2/V·s
μ_{Hall}	Hall mobility	cm^2/V·s
μ_i	Mobility limited by an individual degradation mechanism	cm^2/V·s
μ_{ii}	Ionised impurity scattering-limited mobility	cm^2/V·s
μ_{ph}	Phonon scattering-limited mobility	cm^2/V·s

μ_0	Free carrier mobility	cm^2/V·s
μ_{GLC}	Mobility limited by GLC	cm^2/V·s
$\mu_{0,GLC}$	Effective carrier mobility degraded by GLC $\left(\mu_{0,GLC}^{-1} = \mu_0^{-1} + \mu_{GLC}^{-1}\right)$	cm^2/V·s
μ_{TLC}	Mobility limited by TLC	cm^2/V·s
$\mu_{0,TLC}$	Effective carrier mobility degraded by TLC $\left(\mu_{0,TLC}^{-1} = \mu_0^{-1} + \mu_{TLC}^{-1}\right)$	cm^2/V·s
n	Free electron concentration	cm^{-3}
n_{trap}	Trapped electron concentration	cm^{-3}
N_A^-	The density of ionised acceptors	cm^{-3}
N_D^+	The density of ionised donors	cm^{-3}
N_{TS}^+	The density of ionised tail states	cm^{-3}
$N_{V_{Cu}}^-$	The density of ionised copper vacancies	cm^{-3}
$N_{V_{Cu}}$	The density of copper vacancies	cm^{-3}
N_V	Effective density of states for free holes	cm^{-3}
N_{ch}	Carrier density in the channel layer	cm^{-3}
N_{SS}	The density of bulk traps in the channel layer	cm^{-3}·eV^{-1}
$N_{VBtail}(E)$	The density of tail states at the valence band	cm^{-3}·eV^{-1}
N_{tc}	The density of tail states at $E = E_C$	cm^{-3}·eV^{-1}
N_{tv}	The density of tail states at $E = E_V$	cm^{-3}·eV^{-1}
N_T	The density of the total traps ($N_{SS}t_{ch} + D_{it}$)	cm^{-2}·eV^{-1}
$\mathrm{O_i}$	Oxygen interstitials	
P	Hopping probability between localised states	
p, p_{free}	Free hole concentration	cm^{-3}
p_{trap}	Trapped hole concentration	cm^{-3}

$p_{trap(DOS)}$	p_{trap} calculated from extracted $N_{VBtail}(E)$	cm^{-3}
$p_{trap(Hall)}$	p_{trap} calculated from measured μ_{Hall}	cm^{-3}
p_{total}	Total hole concentration ($p_{free} + p_{trap}$)	cm^{-3}
p^+-Si	Heavily doped p-type silicon (0.01~0.02 Ω·cm)	
q	Elementary charge ($1.6021766208\times10^{-19}$)	C
R_C	S/D contact resistance	kΩ
R_CW	Width normalised contact resistance	kΩ·mm
R_{ch}	Channel resistance per unit channel length	kΩ/μm
R_{CH}	Channel resistance ($R_{ch}L$)	kΩ
R_T	Total resistance ($R_T = R_{ch}L + 2R_C$)	kΩ
SiO_2	Silicon dioxide	
SS	Sub-threshold slop	V/dec
σ	Conductivity	S/cm
σ_0	Pre-exponential factor of the temperature-dependent σ equation	S/cm
θ	Bragg angle	°
t_{ch}	Channel layer thickness	nm
T	Measurement temperature	K
T_A	Annealing temperature	℃
T_t	Characteristic temperature of the tail states	K
T_0	Characteristic temperature of the VRH model	K
V_{Cu}	Copper vacancies	
V_O	Oxygen vacancies	
V_D, V_G	Voltage at the drain and gate	V
V_{DS}, V_{GS}	Drain-source and gate-source voltage	V

$V_{DS,eff}$, $V_{GS,eff}$	Effective V_{DS} and effective V_{GS} applied to the channel	V
W	Channel width of TFTs	µm
x_{dT}	Maximum depletion width	µm

Chapter 1

Introduction

This chapter introduces the motivation behind the work presented in this thesis and the outline of the thesis chapters.

1.1 Motivation

The Internet of Things (IoT) enables a truly ubiquitous electronic environment in which people are always connected by intuition to the internet by touch, sight, sound and even without conscious action. This can be realised by using large-area electronics to integrate all functional devices (e.g. various sensors, radio frequency identification (rfID), logic circuits, memories, power supplies and displays) into everyday objects [1]. Metal oxide thin films have come into the spotlight as promising materials in terms of achieving high performance large-area electronics because the performance of thin film transistors (TFTs) using metal oxides is known to be superior to that of hydrogenated amorphous silicon (a-Si:H) and organic TFTs [2].

IoT-enabled electronics (e.g. wearable devices) require not only high performance but also a low power technology since the limited battery lifetime is a challenge to the operation of the wearable devices [3]. In order to meet this requirement, it is necessary to use complementary metal-oxide-semiconductor (CMOS) circuits, consisting of a pair of n- and p-type TFTs, as the fundamental building block for complex integrated circuits and digital logic. This is because one TFT of the pair is always in the off-state and thus CMOS circuits ideally have almost no static power dissipation. However, contrary to the rapid progress of n-type metal oxide TFTs, p-type oxide TFTs are still at a low technology readiness level and their performance is very poor compared to their n-type counterparts [2]. For this reason, most of metal oxide-based logic circuits such as inverters and ring oscillators have been fabricated using conventional monotype digital designs (e.g. the diode-load design), leading to high power dissipation and low noise margin [4-6]. As a design solution, pseudo-CMOS circuits have been developed, but this technique has its limitations relative to CMOS (e.g. increased circuit complexity and higher static power consumption) [6]. As an alternative, the use of a hybrid complementary technology combining n-type metal oxide and p-type organic TFTs has been proposed, but its limitations (e.g. complex process integration, asymmetry of performance and worse lifetime of organic) hinder its use for practical applications [7, 8]. In this regard, the importance of research on p-type metal oxide TFTs cannot be overemphasised.

Many researchers have proposed cuprous oxide (Cu_2O) as a promising channel layer for p-type metal oxide TFTs [2]. This is because it has intrinsically stable p-type conductivity due to the ease of formation of native acceptors (i.e. copper vacancies) with a shallow acceptor level and the lack of potential hole killers (i.e. copper interstitials and oxygen vacancies) [9]. Furthermore, in contrast to most metal oxides where the valence band maximum (VBM) is strongly localised by O 2*p* orbitals, Cu_2O has a unique orbital configuration with the comparable energy levels of the Cu 3*d* and O 2*p* orbitals, leading to considerable covalency in the ionic metal-oxygen bonds. This not only decreases the localisation nature of the VBM but also broadens the valence band, resulting in more effective carrier transport [10, 11].

However, the existing literature on p-type Cu_2O TFTs has shown a very low field-effect mobility (< 1 $cm^2/V{\cdot}s$) in spite of a rather higher Hall-effect mobility of Cu_2O thin films. Furthermore, Cu_2O TFTs suffer from a high off-state current, leading to a low on/off current switching ratio (typically $10{\sim}10^4$) [12–14]. These are significant challenges to the development of metal oxide-based CMOS circuits, but their main causes have not been clearly explained yet. Against this background, this thesis focuses on improving the carrier mobility of Cu_2O thin films, and on investigating the causes behind the poor performance of Cu_2O TFTs.

1.2 Outline of this thesis

Chapter 2 presents an introduction to Cu_2O with a particular emphasis on the fundamental Cu_2O properties and degradation mechanisms of the carrier mobility. Chapter 3 describes the techniques used for copper oxide deposition, thin film characterisation, and TFT analysis. Chapter 4 describes the process of finding the optimum sputtering condition for stoichiometric Cu_2O thin films using a high target utilisation sputtering system which is known to give better process control than magnetron sputtering [15].

Chapter 5 demonstrates that vacuum annealing can be used for improving the carrier mobility in Cu_2O thin films without phase conversion to either CuO by oxidation or Cu by reduction. Using the vacuum annealing technique, annealing effects on the sputtered Cu_2O thin films are investigated based on the crystallographic, optical and electrical characteristics. In addition, a quantitative analysis as regards the relative dominance of the main conduction mechanisms (i.e. trap-limited and grain-boundary-limited conduction) in Cu_2O films is presented. This particularly provides detailed insight into a change in the carrier mobility by annealing.

Chapter 6 shows that grain orientation of sputtered Cu_2O films can be varied in the direction of either [111] or [100] relative to the surface normal through control of the incident ion-to-Cu flux ratio. Using this technique, this chapter mainly focuses on which one of the two is more favourable in terms of the carrier mobility.

Chapter 7 first shows a TFT-level investigation on the annealing effects, and then proceeds to a discussion on the main reason why Cu_2O TFTs exhibit a significantly lower field-effect mobility compared to the Cu_2O Hall mobility. In addition, this chapter identifies the main origin of the high off-state current in Cu_2O TFTs.

The final chapter summarises key findings in this thesis and provides future research directions for realising high performance p-type Cu_2O TFTs.

Chapter 2

Background

This chapter briefly reviews the fundamental knowledge and concepts that will be used in this thesis. This starts with a historical overview of metal oxide TFTs, and then proceeds to explain why Cu_2O has received much attention as a p-type metal oxide material. Subsequently, the fundamental Cu_2O properties and degradation mechanisms of the carrier mobility in metal oxides are introduced.

2.1 Historical background of metal oxide TFTs

The concept of the field-effect transistor was proposed for the first time by Julius Edgar Lilienfeld in 1925 and patented in 1930 [2]. In this patent, the basic principle of what is called today as the metal-semiconductor field-effect transistor (MESFET, Figure 2.1 (a)) was introduced [2, 16]. Lilienfeld's later patent from 1933 described the concept of the so-called metal-insulator-semiconductor field-effect transistor (MISFET) where an insulator layer (aluminium oxide) is inserted between the copper sulphide (Cu_2S) channel and the Al gate electrode [2, 17].

The first working TFT using polycrystalline cadmium sulphide (CdS) as an active layer was demonstrated by Weimer at the RCA Laboratories in 1962 (see its schematic structure in Figure 2.1 (b)) [18]. In 1964, Klasens and Koelmans proposed a metal oxide TFT using SnO_2 for the first time [19] and Boesen and Jacobs reported a TFT with lithium-doped ZnO in 1968 [20]. However, in the mid-1960s, the emergence of crystalline silicon-based MOSFET technology gave rise to a decrease in TFT development activity by the end of the 1960s [21].

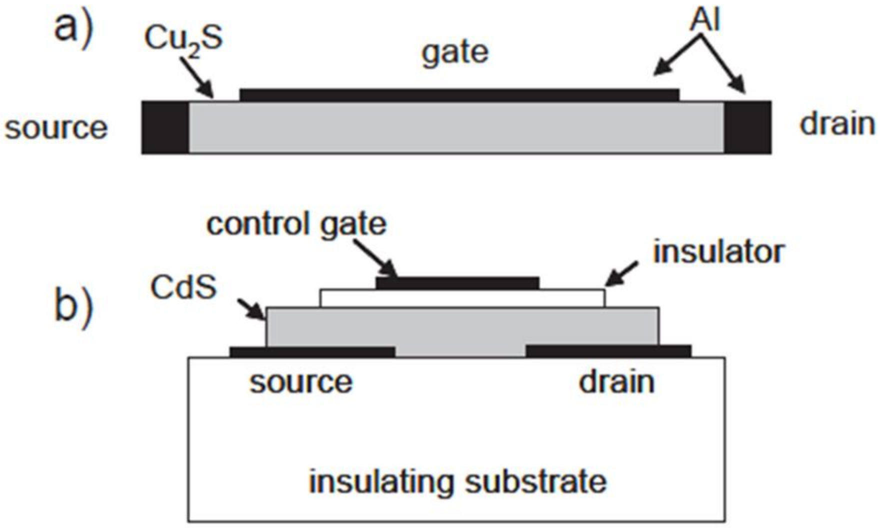

Figure 2.1. Simplified cross-sectional views of (a) an MESFET, the first field-effect transistor proposed by Lilienfeld, and (b) the first working TFT fabricated by Weimer. Image reproduced from [21].

TFT technology was back in the spotlight in the 1970s because some applications (e.g. active matrix flat-panel displays) required large arrays of low cost transistors [21]. Brody *et al.* successfully demonstrated the first active matrix liquid crystal display (AM-LCD) using a CdSe TFT as a switching device for each pixel in 1973 [22]. After the first hydrogenated amorphous silicon (a-Si:H) TFT was demonstrated by LeComber and Spear in 1979 [23], many laboratories started to develop AM-LCDs using a-Si:H TFTs [21]. Since the mid-1980s, the silicon-based TFTs, either based on a-Si:H or polycrystalline silicon, have successfully dominated the large area AM-LCD market [21, 24].

However, a-Si:H TFTs have drawbacks such as a low field-effect mobility (< 1 $cm^2/V\cdot s$) and instability under electrical bias stress (i.e. a change in threshold voltage (V_{th})) [25, 26]. Specifically, a-Si:H has a strong tailing (i.e. a broad distribution of localised tail states) in its band gap, and carrier trapping in the tail states is known as the main cause of the low carrier mobility. The instability corresponding to the V_{th} change is generally explained by two mechanisms: defect (i.e. dangling bond) creation in the a-Si channel and charge trapping in the gate insulator [27]. The low mobility and instability are not critical for AM-LCDs operating at a low frame rate (e.g. 60 Hz) since a field effect mobility of only ~0.5 $cm^2/V\cdot s$ is sufficient to drive AM-LCD panels up to 90 inches in size and the instability can be compensated by LCD driver circuits. However, TFTs with a high mobility are required in active matrix organic light-emitting-diode (AM-OLED) displays because an OLED is a current-driving device and therefore TFTs must provide high currents. Furthermore, a small variation in V_{th} of only ±0.1 V results in a change in the OLED luminance by 16 % [26, 28]. This leads to an unacceptable difference in the brightness of OLED pixels, which causes a serious *mura* problem. For this reason, the OLED displays using a-Si:H and organic TFTs with poor V_{th} stability must employ complex compensation circuits (e.g. 4T2C or 5T2C circuits where T and C denote the number of transistors and capacitors). As seen in Figure 2.2, displays with higher resolution, a faster frame rate and a larger panel size also require a higher carrier mobility; for instance, it was reported that AM-LCDs > 55 inches and operating at high frame rates

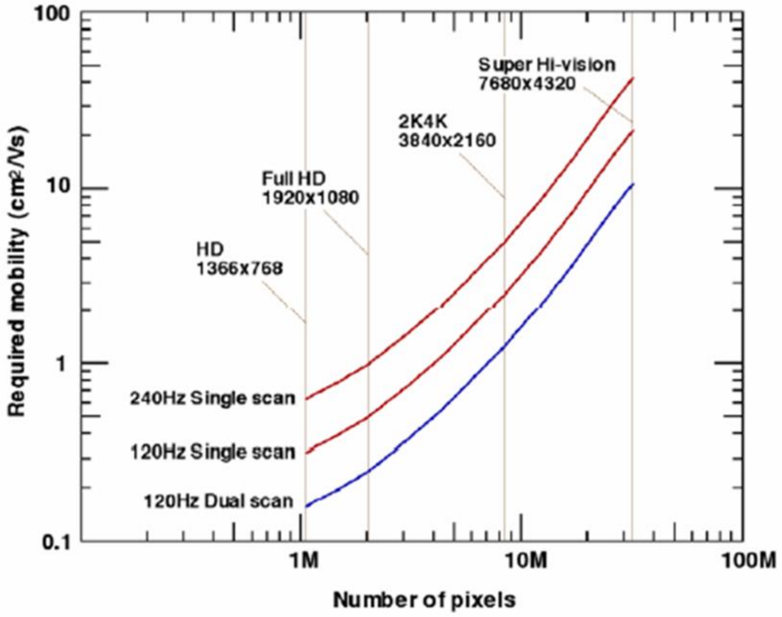

Figure 2.2. Required carrier mobility according to resolution, frame rate and panel size. Image reproduced from [26].

> 120 Hz cannot be driven by low-mobility a-Si:H TFTs. In the case of three-dimensional (3D) displays, since the displays must provide two or more alternating image frames for the left and right eyes, a higher frame rate (e.g. 480 Hz) is required to enhance their image quality [26].

With a demand for high-mobility TFTs compatible with high-frame-rate LCDs, OLED and 3D displays, metal oxide TFTs have come into the spotlight again since 2003 [25, 26]. In particular, polycrystalline ZnO (poly-ZnO) TFTs were researched intensively [29–32] because it was expected that poly-ZnO TFTs should have better performance compared to a-Si:H and organic TFTs based on the high Hall-effect mobility (200 $cm^2/V\cdot s$) of single-crystal ZnO [25]. However, ZnO is actually a transparent conductive oxide containing a high density of intrinsic free electrons (typically > 10^{17} cm^{-3}) because of a large number of native point defects (e.g. oxygen vacancies and zinc interstitials), thereby leading to difficulty in controlling the channel conductance and the threshold voltage, and fabricating normally-off TFTs [26]. As a solution to this problem, in 2003, Nomura *et al.* (in the Hosono Group at Tokyo Institute of Technology) proposed single-crystalline $InGaO_3(ZnO)_5$ (sc-IGZO) with a low intrinsic carrier concentration as a channel layer of TFTs, and demonstrated normally-off TFTs with impressive performance: a high field-effect mobility of ~80 $cm^2/V\cdot s$ and an on/off current ratio of ~10^6 [33]. Although a very high annealing temperature of 1400 ℃ was required to obtain the sc-IGZO layer, this paper drew worldwide attention because it demonstrated that high-performance metal oxide TFTs are a reality [2]. The Hosono group also found that, contrary to transparent conductive oxides such as amorphous Sn-doped In_2O_3 (a-ITO) and poly-ZnO, a low carrier concentration can be obtained in amorphous IGZO (a-IGZO) [26]. This is because, as demonstrated by first-principles density-functional calculations [34], Ga ions have much stronger chemical bonds with oxygen than In and Zn ions and thus the incorporation of Ga into multicomponent oxides suppresses the formation of oxygen vacancies and the consequent creation of electrons. However, the addition of a high Ga content lowers the carrier mobility and therefore it is important to use an appropriate amount of the Ga ions for obtaining the optimum TFT performance [25]. Using the a-IGZO as a channel layer, Nomura *et al.* demonstrated the room-temperature fabrication of fully transparent TFTs on a flexible substrate in late 2004 [35]. Although the a-IGZO TFTs exhibited inferior performance compared to the sc-IGZO TFTs, a field-effect mobility of ~6–9 $cm^2/V\cdot s$ and an on/off current ratio of ~10^3 could still be obtained using room-temperature processing [2, 35].

Nomura's work showed the enormous potential of metal oxide materials for TFT applications, and led to intensive research into TFTs using various amorphous multicomponent oxides such as indium gallium zinc oxide (IGZO) [36–39], indium zinc oxide (IZO) [40, 41] and zinc tin oxide (ZTO) [42–46]. Thanks to continuous improvements in the performance of these TFTs, metal oxide TFTs currently show remarkable performance such as a field-effect mobility > 10 $cm^2/V\cdot s$ and an on/off current ratio > 10^7; this performance is vastly superior to that of a-Si:H and organic TFTs [2]. Figure 2.3 summarises these main breakthroughs in TFT technology.

Contrary to the significant progress of n-type metal oxide TFTs, p-type oxide TFTs still exhibit very poor performance such as a very low field-effect mobility and a high off-state current [2]. For this reason, the use of metal oxide TFTs are limited to n-type switching devices for display backplanes as in a-Si:H TFTs. As pointed out in Chapter 1,

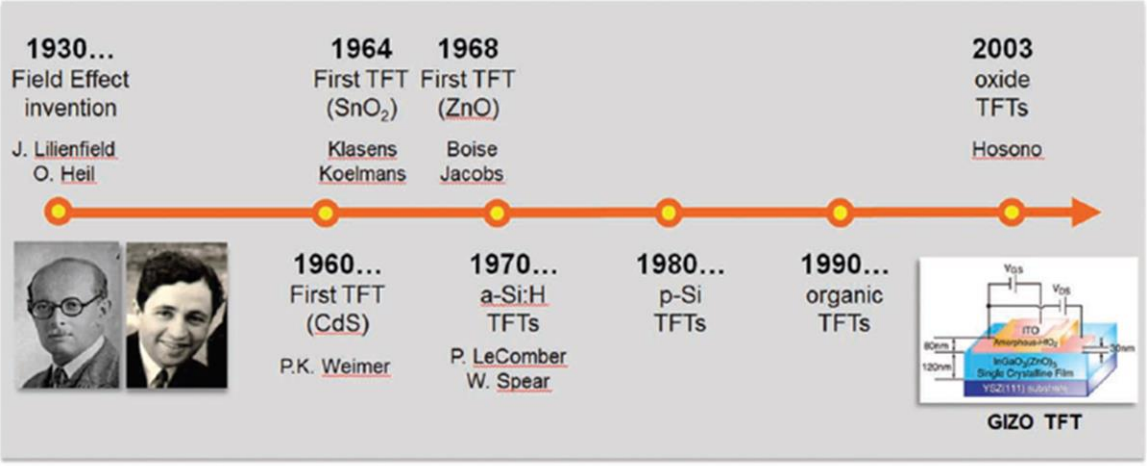

Figure 2.3. Main breakthroughs of the TFT technology. Image reproduced from [2].

in order to extend the use of the oxide TFTs into IoT-enabled electronics (e.g. wearable devices), research on p-type metal oxide TFTs is required for realising metal oxide-based CMOS circuits enabling low power consumption of the electronics. This is because a low power technology is critical for operating the IoT-enabled mobile electronics due to their limited battery lifetime.

2.2 p-type metal oxide semiconductors

2.2.1 Problems and challenges

Most of metal oxide conductors and semiconductors (e.g. ZnO, In_2O_3, SnO_2) are naturally n-type and cannot easily be doped p-type since their charge neutrality levels (CNLs) lie very close to or even above the conduction band minimum (CBM) as seen in Figure 2.4 [47]. The CNLs lie far above the valence band maximum (VBM) in ZnO, In_2O_3 and SnO_2,

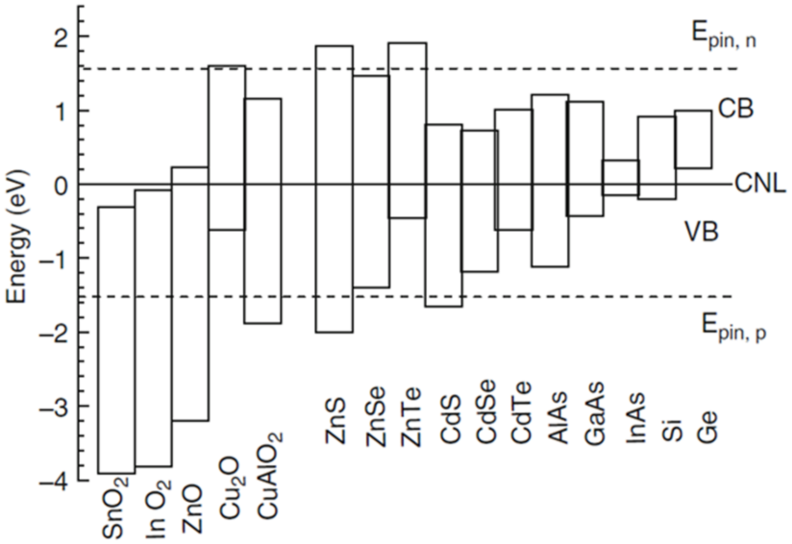

Figure 2.4. Band diagrams of various semiconductors aligned according to their charge neutrality levels (CNLs) with dopant pinning levels ($E_{pin,n}$ and $E_{pin,p}$). Image reproduced from [47].

which indicates the difficulty in p-type doping in these materials. To be specific, in the case of ZnO, it cannot be doped p-type by native defects (e.g. zinc vacancies, V_{Zn}) under thermal equilibrium although the V_{Zn} have a negative charge state V_{Zn}^{2-} in ZnO (see Figure 2.5). This is because native donors (e.g. oxygen vacancies, V_O, and zinc interstitials, Zn_i) have much lower formation enthalpies compared to V_{Zn} and therefore a large number of inherent V_O and Zn_i defects compensate p-type doping [48]. In addition, since nitrogen (N) was regarded as a shallow acceptor in ZnO based on its acceptor level (~0.4 eV above the VBM) calculated by density functional theory within the local density approximation (DFT-LDA) [49], there were many attempts to realise p-type ZnO using extrinsic N

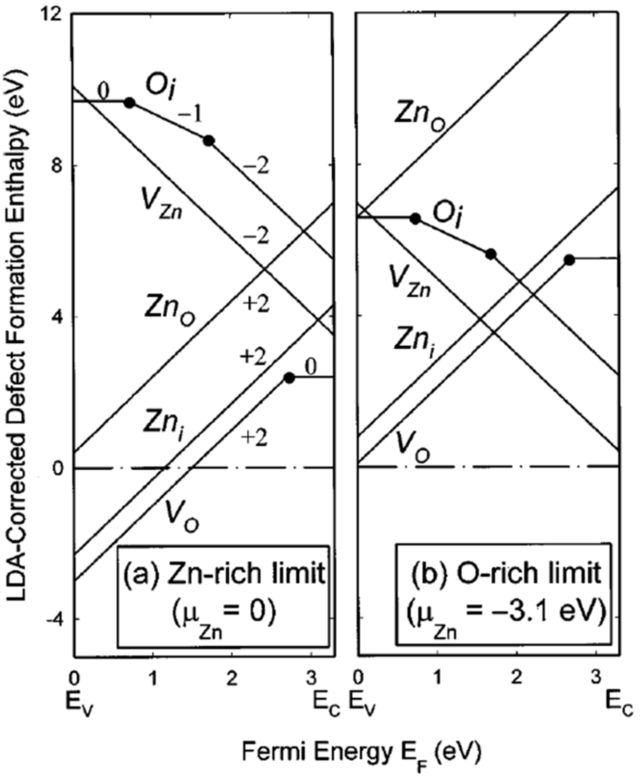

Figure 2.5. Defect formation energies in ZnO as a function of the Fermi energy E_F at (a) Zn-rich and (b) O-rich limits. Here, -2, -1, 0 and +2 denote the charge states of the defects, and the defect transition (i.e. ionisation) energies $\varepsilon(q/q')$ are indicated with solid dots. Image reproduced from [48].

doping (see reference [50, 51] for a thorough list of studies in this field). It was also proposed by theoretical calculations that simultaneous codoping using N with reactive codopants (Al, Ga or In) can not only improve the solubility of the N acceptor but also lower its ionisation energy [52]. Using this codoping method, Joseph *et al.* reported p-type conductivity in N-doped ZnO [53], but the experimental results have not been reproduced. Furthermore, based on advanced first-principles calculations (DFT with hybrid functionals), Lyons *et al.* have recently demonstrated that N in fact acts as a deep acceptor with the ionisation energy of 1.3 eV, which explains why N doping cannot lead to reproducible p-type conductivity in ZnO [51].

Another serious problem with metal oxides is a very low hole mobility. This can be understood based on the bandgap formation mechanism in ionic oxide semiconductors (Figure 2.6). The difference in electron affinity between metal (M) and oxygen atoms causes electron transfer from metal n*s* orbitals to oxygen 2*p* orbitals as seen in Figure 2.6 (a) (here n is the principle quantum number). The Madelung potential formed by the ionised atoms stabilises the ionic charge distribution, raising the energy levels in the metal cations (M^{2+}) and lowering the levels in the oxygen anions (O^{2-}). As a result, the CBM mainly consists of unoccupied *s* orbitals of the metal cations and the VBM is formed by

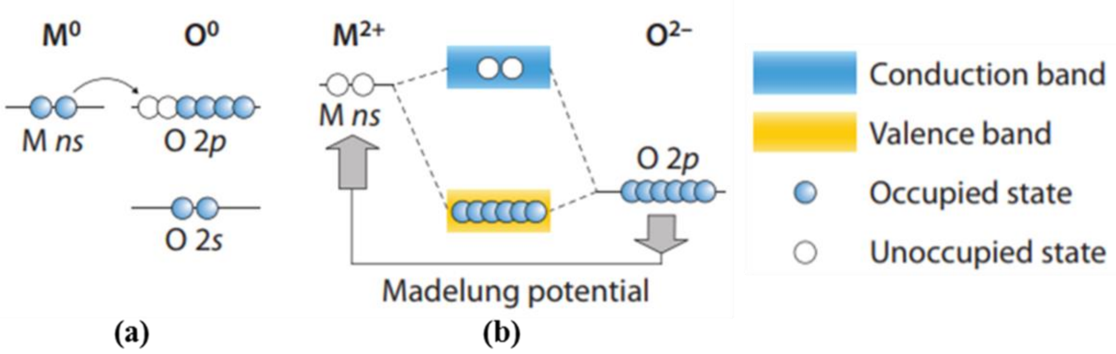

(a) (b)

Figure 2.6. Schematic diagram showing the bandgap formation mechanism in ionic oxide semiconductors. Image reproduced from [25].

fully occupied O 2*p* orbitals as seen in Figure 2.6 (b). The *s* orbitals of the heavy metal cations have large spatial sizes and spread spherically. This results in broad band dispersion of the CBM and therefore a small electron effective mass (i.e. a high electron mobility) [25, 34]. By contrast, the VBM tends to be strongly localised by 2*p* orbitals of oxygen anions and thus has a small dispersion (i.e. a large hole effective mass), which is the reason for the very poor hole mobility [10, 47].

2.2.2 Solution: Chemical modulation of the valence band

In order to reduce the strong localisation nature of the VBM, Kawazoe *et al.* [10, 11] proposed a method of hybridising the O 2*p* orbitals with *d* orbitals of cations, which is called chemical modulation of the valence band (CMVB). Figure 2.7 (a) represents the

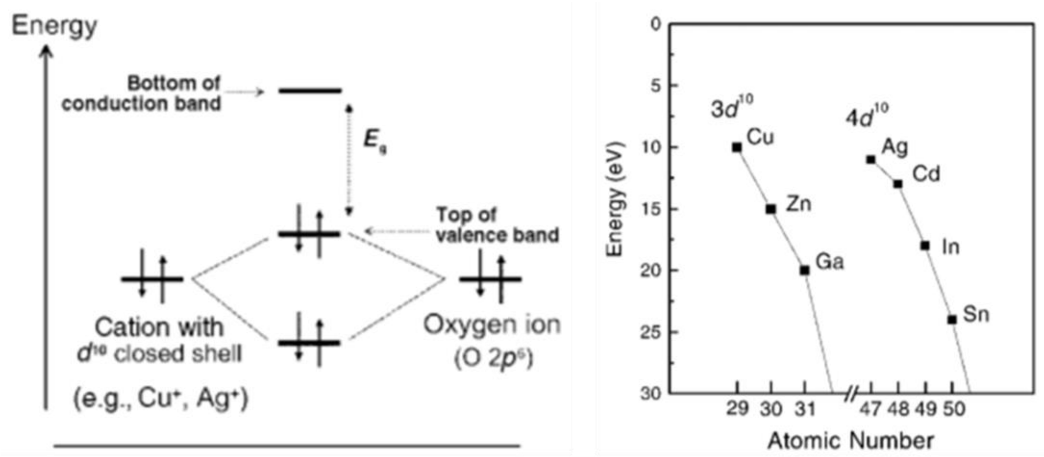

(a) (b)

Figure 2.7. (a) Schematic illustration of modulation of the energy band structure and (b) variations in the energy levels of $3d^{10}$ orbitals on Period 4 atoms and those of $4d^{10}$ orbitals on Period 5 atoms with an increase in atomic number. In (a), the cation is assumed to have a closed *d* shell whose energy is equivalent to that of O 2*p* orbitals. Image reproduced from [11].

requirements of metallic cations. The outermost *d* orbitals of cations should have a closed shell electronic configuration (i.e. d^{10}) whose energy is comparable to that of the O 2*p* orbitals. The closed *d* shell is required to prevent coloration caused by electron transitions between a lower energy *d* orbital and a higher energy *d* orbital (i.e. *d*-*d* transitions). The comparable energy levels of the outermost cation *d* and O 2*p* orbitals increase the efficiency of their hybridisation, which leads to considerable covalency for their bonding and anti-bonding levels. Since both of the orbitals are fully occupied by electron pairs, the anti-bonding level becomes the highest occupied level. Consequently, the VBM shifts from the O 2*p* orbitals to the anti-bonding level as shown in Figure 2.7 (a) [10, 11]. This not only reduces the localisation nature of the VBM but also increases the dispersion of the VBM and this in turn leads to a reduction in the effective hole mass (i.e. an improvement in a hole mobility) [10, 47]. The Cu $3d^{10}$ orbital is the best case of this because its energy level is the closest to that of the O 2*p* orbital (see Figure 2.7 (b)) [10, 11]. For this reason, copper oxides, particularly Cu_2O, have received much attention as a p-type oxide material.

2.3 Fundamental properties of cuprous oxide (Cu_2O)

2.3.1 Origin of p-type conductivity

There are three requirements for p-type doping via native defects in metal oxides [9]:
(a) Low formation energy of native acceptors (e.g. cation vacancies and anion interstitials);
(b) Small ionisation energy of the acceptors (i.e. a shallow acceptor level with respect to the VBM) in order to effectively produce holes;
(c) High formation energy of native donors that compensate holes (e.g. cation interstitials and anion vacancies).

Figure 2.8 represents the calculated formation energies (solid lines) and transition (i.e. ionisation) energies of intrinsic point defects in Cu_2O under both Cu-rich/O-poor and Cu-poor/O-rich conditions, which clearly shows that Cu_2O satisfies all the above requirements. Specifically, there are two possible native acceptors in Cu_2O: copper vacancies (V_{Cu}) and

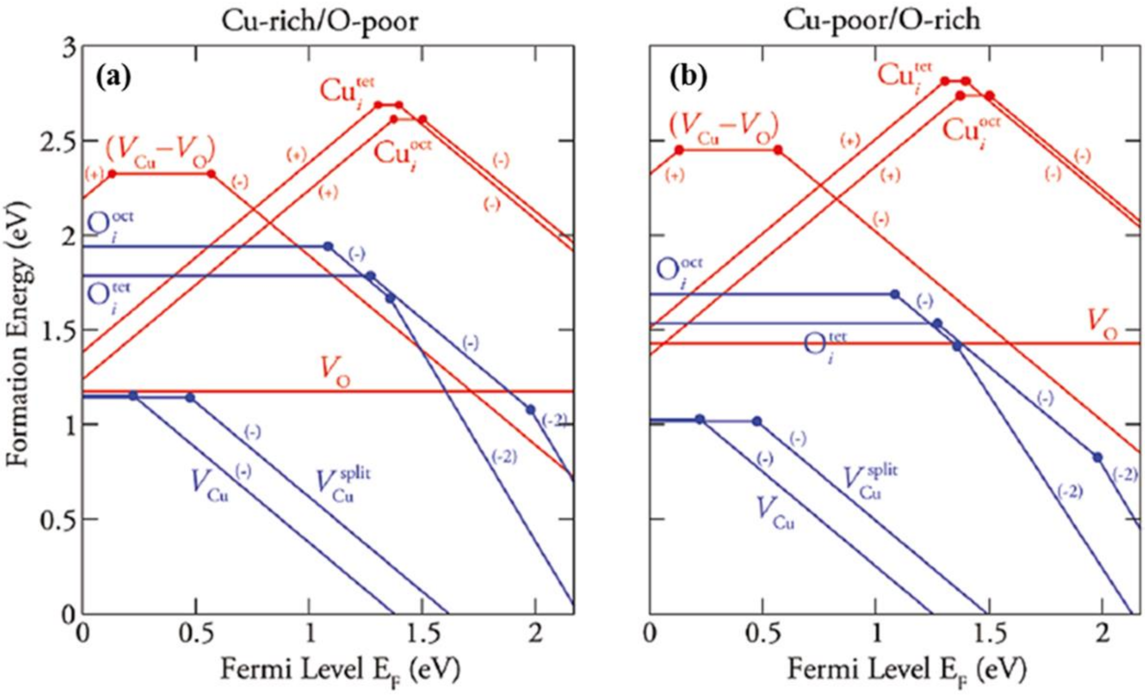

Figure 2.8. Defect formation energies in Cu_2O as a function of the Fermi energy E_F under (a) Cu-rich/O-poor and (b) Cu-poor/O-rich conditions. Here, (-2), (-) and (+) denote the charge states of the defects, and the superscripts, tet and oct, mean the tetrahedral and octahedral interstitial positions. The defect transition energies $\varepsilon(q/q')$ are indicated with solid dots. Image reproduced from [54].

oxygen interstitials (O_i). Since O_i (in tetrahedral and octahedral positions) have deep acceptor levels (i.e. very high $\varepsilon(0/–)$ and $\varepsilon(–/2–)$ transition levels with respect to the VBM), they cannot produce holes. Here, the terminology $\varepsilon(q/q')$ means the transition level that the charge state of defects changes (i.e. $q \rightarrow q'$); for example, $\varepsilon(0/–)$ means the transition level that the charge state changes from the charge-neutral state to the (-1) charge state. In contrast, under both the Cu-rich and Cu-poor conditions, V_{Cu} have the lowest formation energy with a shallow acceptor level (i.e. small $\varepsilon(0/–)$ ionisation energy of $E_V + 0.28$ eV) [9]. This indicates that V_{Cu} are the main origin of holes in Cu_2O and fulfil the requirements (a) and (b).

Potential native donors in Cu_2O are oxygen vacancies (V_O) and copper interstitials (Cu_i). As seen in Figure 2.8, although V_O have a rather low formation energy, they do not have a charge transition level inside the band gap. This means that they are only stable in the charge-neutral state and therefore cannot compensate holes created by V_{Cu}. Furthermore, even though Cu_i have a positive charge state Cu_i^+, their formation energy is considerably higher than that of V_{Cu} and they are thus incapable of efficiently compensating holes [9]. For these reasons, p-type conductivity attributable to V_{Cu} dominates in Cu_2O and therefore Cu_2O has intrinsically stable p-type conductivity under all growth conditions.

2.3.2 Crystalline structure

Cu_2O has the cuprite structure which is a simple cubic Bravais lattice with the symmetry of the 224th space group (i.e. $Pn\bar{3}m$ or O_h^4) as seen in Figure 2.9. Inside the unit cell, the

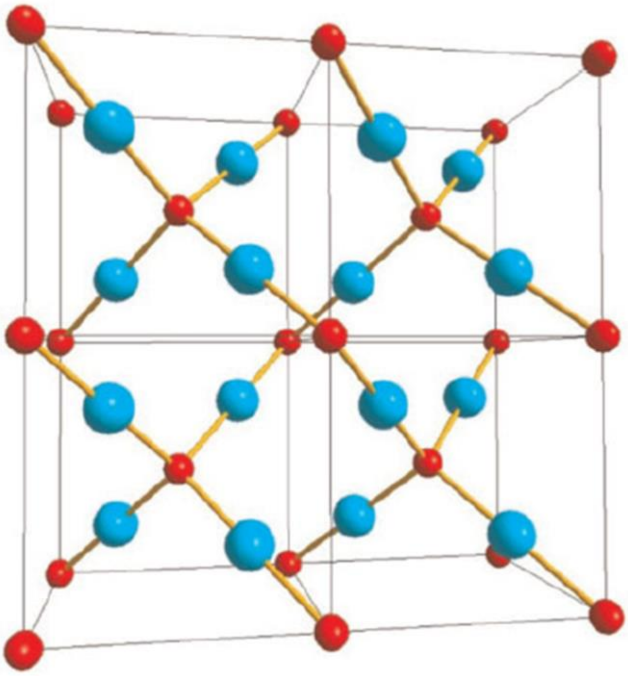

Figure 2.9. Cu_2O crystal structure represented by four unit cells. The big blue and small red spheres are copper and oxygen atoms, respectively. Image reproduced from [55].

copper atoms are positioned in a face-centred cubic (fcc) sub-lattice (blue spheres) and the oxygen atoms are located on a body-centred cubic (bcc) sub-lattice (red spheres). As a result, the copper atoms are located on the vertices of a tetrahedron centred on the oxygen atom and are linearly twofold coordinated with the oxygen atoms as nearest neighbours, while the oxygen atoms are fourfold coordinated with the copper atoms as nearest neighbours [55, 56].

As for crystallographic properties of Cu_2O, the lattice constant, Cu-O bond length, O-O separation and Cu-Cu separation are a = 4.27 Å, $d_{\text{Cu-O}}$ = 1.85 Å, $d_{\text{O-O}}$ = 3.68 Å and $d_{\text{Cu-Cu}}$ = 3.01 Å, respectively. The molar mass and molar volume are M = 143.092 g/mol and V_{m} = 23.46 cm^3/mol and thus the density of Cu_2O is ρ = 6.10 g/cm^3 [56].

2.3.3 Band structure and effective masses

Figure 2.10 shows the band structure of Cu_2O schematically. The valence band ($\Gamma_{25'}$) is split by spin-orbit interaction into Γ_7^+ and Γ_8^+ states, and the lowest conduction-band state derived from Γ_1 has the same parity (Γ_6^+). For this reason, the lowest absorption transitions (i.e. $\Gamma_7^+ \rightarrow \Gamma_6^+$ and $\Gamma_8^+ \rightarrow \Gamma_6^+$) are not allowed. In contrast, the second lowest conduction-band state has the allowed parity (Γ_8^-) and thus strong optical absorption occurs at the transitions (i.e. $\Gamma_7^+ \rightarrow \Gamma_8^-$ and $\Gamma_8^+ \rightarrow \Gamma_8^-$) [55].

Table 2.1 shows calculated effective masses at Γ along the $\Gamma - X$ (100), $\Gamma - M$ (110) and $\Gamma - R$ (111) directions as well as their experimental data. The electron (m_e^*) and light hole effective masses (m_{lh}^*) are isotropic whereas other hole effective masses (i.e. heavy hole, m_{hh}^*, and spin-orbit hole masses, m_{soh}^*) are anisotropic. As mentioned above, due to the spin-orbit splitting of the valence band at Γ, the top of the valence band has the Γ_7^+ state with m_{lh}^* which is even smaller than m_e^* [55, 57]. This is contrary to n-type metal oxides where the hole effective mass is much larger than the electron effective mass, and this is an attractive property for a p-type TFT channel layer. In addition, the effective masses calculated by DFT-LDA are smaller compared to the experimental data, which is related to the bandgap underestimation of the LDA calculations [57].

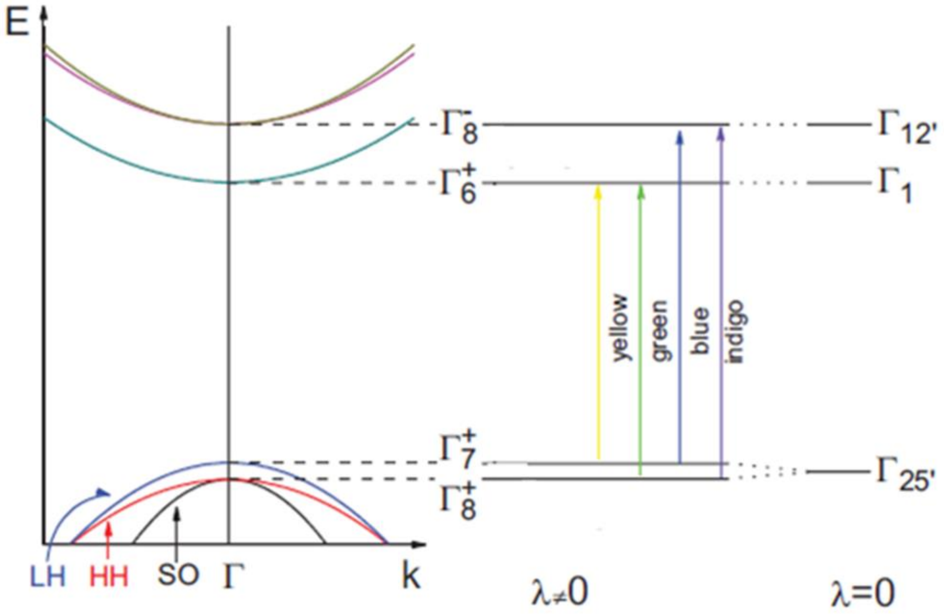

Figure 2.10. The *E*-*k* diagram of Cu_2O near the Brillouin zone centre (left); a simplified band diagram at the Γ-point with ($\lambda \neq 0$) and without spin-orbit interaction ($\lambda = 0$), representing the interband transitions (right). Here, LH, HH and SO denote the light hole, heavy hole and spin-orbit hole, respectively. Image reproduced from [55].

Table 2.1. Electron and hole effective masses (in unit of the electron rest mass, m_0) from DFT-LDA calculations and from experiment. Subscripts (e, lh, hh, soh) denote electron, light hole, heavy hole and spin-orbit hole, respectively. Table reproduced from [55]

Mass	**Band**	$\boldsymbol{\Gamma - X}$ **(100)**	$\boldsymbol{\Gamma - M}$ **(110)**	$\boldsymbol{\Gamma - R}$ **(111)**	**Average**	**Experiment**
m_e^*	Γ_6^+	0.92	0.92	0.92	0.92	0.99 (0.93[a])
m_{lh}^*	Γ_7^+	0.36	0.36	0.36	0.36	0.58 (0.56[a])
m_{hh}^*	Γ_8^+	2.83	0.91	0.72	1.49	
m_{soh}^*	Γ_8^+	0.21	0.25	0.27	0.24	

[a] Polaron correction value (see reference [58]).

2.3.4 Dominant intrinsic scattering mechanisms

The free carrier mobility is affected by intrinsic scattering mechanisms. Based on the theory of carrier-lattice interactions in polyatomic crystals, Shimada and Masumi [59] calculated the theoretical limit of the free carrier (hole) mobility in Cu_2O by longitudinal-optical (LO) phonon scattering (see $\mu_{\mathrm{LO\ phonon}}$ in Figure 2.11), and Lee *et al.* [60] calculated its theoretical limit by ionised impurity scattering (see $\mu_{\mathrm{H,ii}}$ in Figure 2.11). This shows that the dominant intrinsic scattering mechanisms in Cu_2O are phonon scattering at high temperatures and ionised impurity scattering at low temperatures (< 200 K).

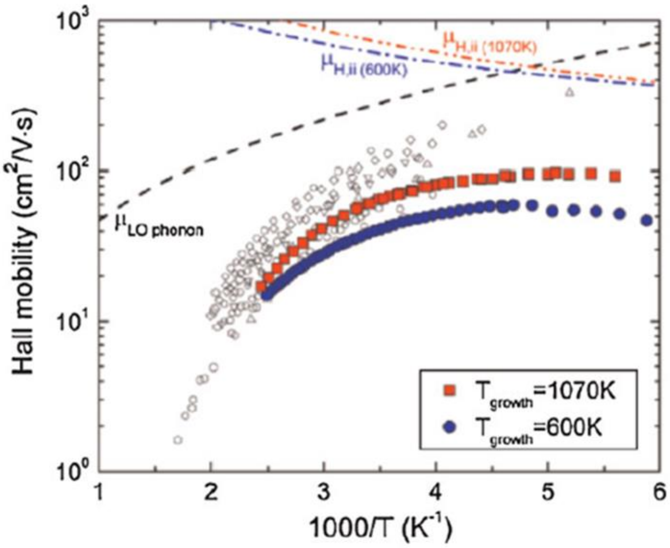

Figure 2.11. Theoretical limits of the free carrier mobility in Cu_2O. Lines show its limits by LO phonon scattering and ionised impurity scattering. Open symbols represent temperature-dependent Hall mobilities of monocrystalline Cu_2O from various references (see reference [60]), and close symbols represent Hall mobilities of Cu_2O sputtered at temperatures (600 and 1070 K). Image reproduced from [60].

2.4 Carrier mobility degradation mechanisms in metal oxides

Apart from the intrinsic scattering mechanisms, the carrier mobility in metal oxides is strongly affected by other degradation mechanisms: grain-boundary-limited conduction, percolation conduction and trap-limited conduction. For this reason, in order to fully understand the carrier transport property in metal oxide materials, the degradation mechanisms should be considered.

Polycrystalline metal oxides (e.g. ZnO and In_2O_3) have potential energy barriers at grain boundaries, which impedes carrier transport (grain-boundary-limited conduction, see Figure 2.12 (a)) [61]. Mixing of two or more metal cations with different sizes and ionic charges (e.g. Ga^{3+} and Zn^{2+}) forms amorphous multicomponent oxides such as a-IZO, a-ZTO and a-IGZO [25]. However, random distribution of the metal cations leads to potential fluctuations in the CBM, which results in a distribution of percolation barriers in the CBM [62, 63]. For this reason, electrons take a longer winding path and this gives rise to degradation of the carrier mobility (percolation conduction, see Figure 2.12 (b)) [25].

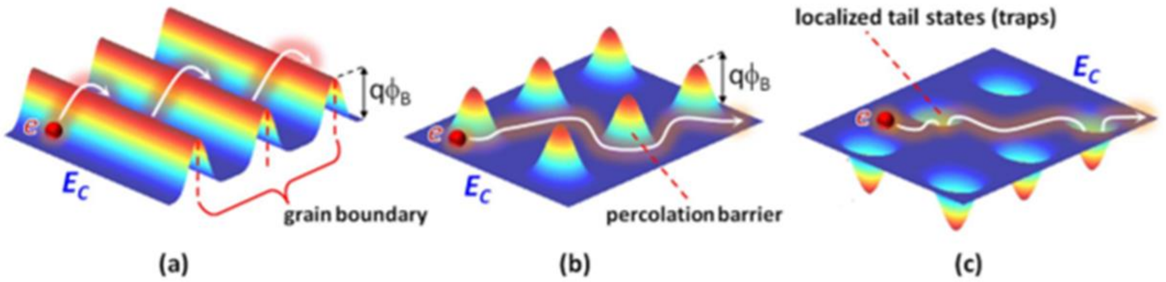

Figure 2.12. Schematic illustration of three degradation mechanisms of the carrier mobility in metal oxides: (a) grain-boundary-limited conduction, (b) percolation conduction and (c) trap-limited conduction related to localised tail states. Here, '*e*' denotes a free electron. ϕ_B means the potential barrier height at grain boundaries in (a) and the percolation barrier height caused by random distribution of various metal cations (e.g. Ga^{3+} and Zn^{2+}). Image reproduced from [63].

Since the work of Anderson [64], it is well known that structural disorder causes localised tail states below the CBM and above the VBM [47]. The carrier mobility is strongly affected by multiple carrier trapping and thermal release at the localised tail states (trap-limited conduction, see Figure 2.12 (c)) [65, 66].

In fact, electron transport in metal oxides is not significantly affected by the trap-limited conduction due to a very small effect of disorder on the CBM mainly consisting of metal *s* orbitals. To be specific, spherical overlapping *s* orbitals are insensitive to angular disorder and ion packing keeps the metal-metal distance rather constant (i.e. insignificant bonding distance disorder) because of the large spatial size of the metal ions [47]. In contrast, hole transport in p-type Cu_2O is significantly degraded by the trap-limited conduction. The reason for this is that non-spherical Cu 3*d* orbitals mainly forming the VBM cause considerable angular disorder and this gives rise to a strong tailing (i.e. a broad distribution of localised tail states) near the VBM [47]. Given that the low carrier mobility in a-Si:H is mainly due to severe carrier trapping by a strong band tailing stemming from *p* states around its band gap [47, 65], p-type Cu_2O is expected to have a low carrier mobility as a-Si:H.

In the case of p-type Cu_2O, percolation conduction is excluded from the main degradation mechanisms of the carrier mobility since it is a binary oxide. Based on its polycrystalline phase and the highly disordered nature of the VBM, it is expected that the carrier mobility in Cu_2O is strongly affected by grain-boundary-limited and trap-limited conduction. This will be discussed in detail in section 5.5 (relative dominance of conduction mechanisms).

Chapter 3

Experimental methodology

3.1 Thin film deposition: High target utilisation sputtering

This section introduces the high target utilisation sputtering (HiTUS) system used in this study for deposition of copper oxide thin films and discusses effects of the main sputtering parameters on film properties.

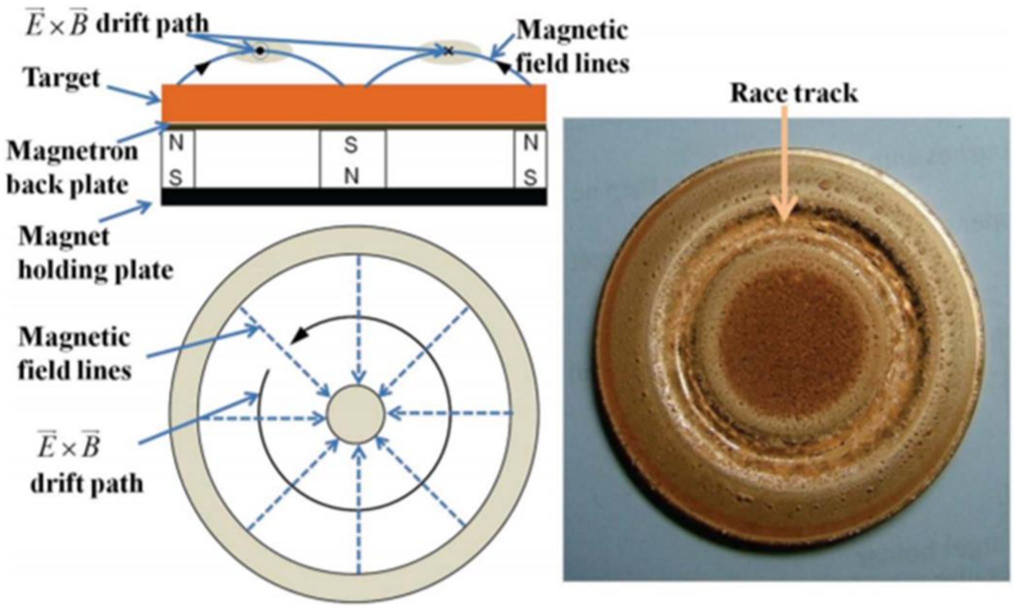

Figure 3.1. Schematic diagrams showing the principle of the racetrack formation in a circular planer magnetron target (left side) and a photograph of a copper target with a racetrack (right side). Image reproduced from [68].

Originally, the HiTUS deposition system (Plasma Quest Limited) was designed in order to maximise target utilisation through eliminating the racetrack which occurs in magnetron sputtering systems [69]. To be specific, in a magnetron sputtering system (see Figure 3.1), a permanent magnet array is placed behind the target, creating a static magnetic field parallel to the target surface. Secondary electrons emitted from the target are constrained by this magnetic field, forming a current loop of drifting secondary electrons (i.e. $\vec{E} \times \vec{B}$ drift ring). Collisions of the electrons and Ar gas atoms lead to an extremely dense plasma in this drift ring and as a result, a deep groove (i.e. race-track) forms by heavy sputter erosion over the drift ring as seen in the right hand side of Figure 3.1 [68, 70]. Because of this phenomenon, only about 25 % of the magnetron target is utilised in the sputtering process [69].

As seen in a schematic diagram of the HiTUS system (Figure 3.2), a high density Ar plasma is generated in a sidearm to the main sputtering vacuum chamber by an inductively coupled RF (13.56 MHz) plasma (ICP) source. The Ar plasma is then guided to the target by a combination of two electromagnets [15], which enables formation of a high density Ar plasma at the target surface without the addition of the magnet array behind the target. Therefore, the HiTUS system in which the magnet array of the target is eliminated allows > 90 % target utilisation with uniform target erosion (i.e. without a racetrack). This is why this system is named as high target utilisation sputtering [69].

Another striking feature of this system is to enable independent and precise control of the Ar ion density and ion energy [15]. Specifically, the remote plasma source generates a high density Ar plasma with a low ion energy due to the inductive coupling (ion density > 10^{13} cm^{-3} and ion energy < 10 eV) [71]. For this reason, sputtering only occurs when a sufficient DC target bias is applied to accelerate the initially low energy ions towards the target surface. This decouples the ion density (controlled by the remote RF antenna power supply) from the ion energy (controlled by the target bias power supply) [15, 72], which is not possible under a conventional sputtering system where the Ar plasma is generated in a main chamber by a single (DC or RF) power supply.

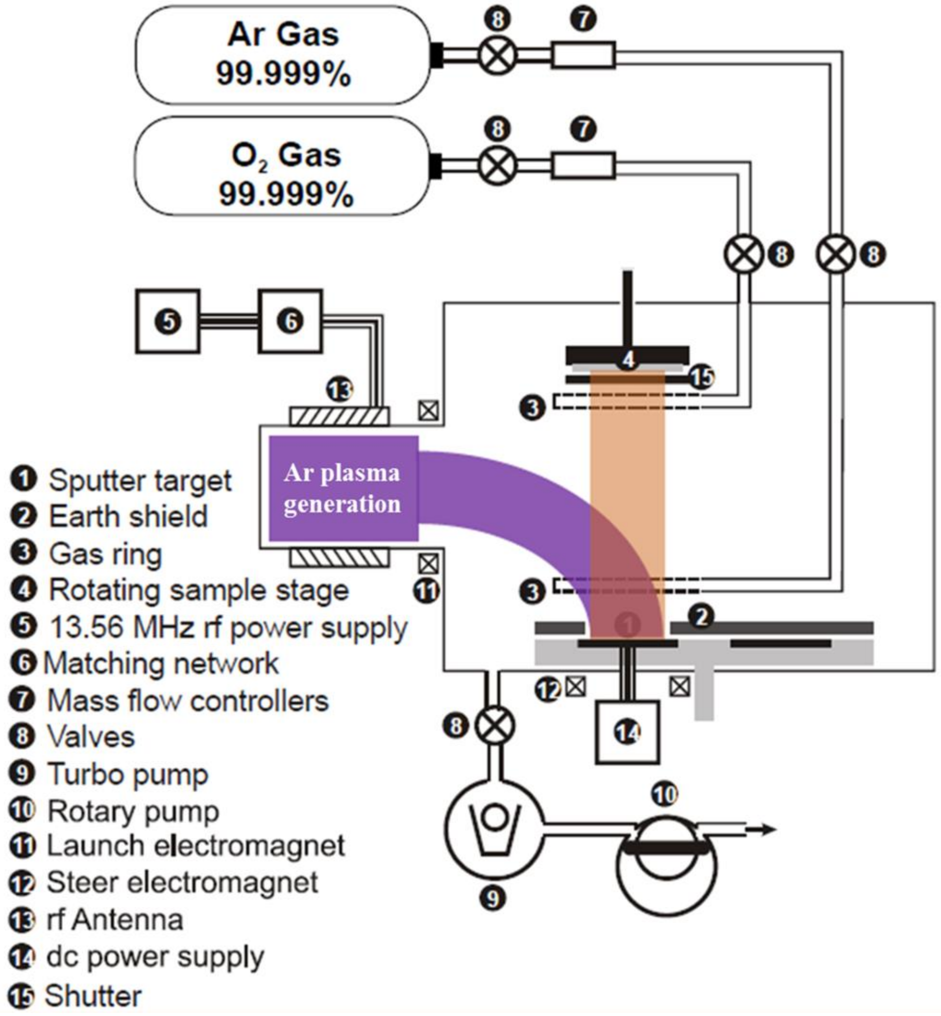

Figure 3.2. A schematic diagram of the HiTUS system with a remote Ar plasma chamber. Image reproduced from [15].

There are four main sputtering parameters affecting film properties in the HiTUS system: (1) oxygen flow rate, (2) target bias voltage, (3) ion current and (4) process pressure. Here, the ion current is a parameter related to the Ar plasma density at the surface of the Cu target. The oxygen flow rate is related to the amount of oxygen being able to react with sputtered Cu atoms while the target bias voltage and ion current are associated with the number of sputtered Cu atoms (i.e. a Cu flux). Thus, these sputtering parameters have a significant effect not only on film stoichiometry but also on the formation energies of intrinsic defects (see Figure 2.8 in Chapter 2). Furthermore, a combination of these parameters determines the dominant phase (i.e. Cu_2O or CuO) of copper oxide films. The process pressure has an influence on the film morphology (e.g. grain size, film densification and roughness) [73]. To be specific, A lower process pressure (i.e. a lower Ar flow rate) decreases the probability of collisions with the Ar background gas during the transit of the sputtered atoms from the target to the substrate, which leads to an increase in kinetic energy of the adatoms. This improves the surface and bulk diffusion ability of the adatoms, resulting in a dense film with a larger grain size.

3.2 Thin film characterisation

This section briefly describes the techniques used for characterisation of copper oxide thin films. Unless specifically stated otherwise, all work was carried out solely by the author.

3.2.1 X-ray diffraction

X-ray diffraction (XRD) is a powerful tool used for investigating crystallographic characteristics (e.g. the phase of a crystalline material, crystallographic orientation and film crystallinity). Intense diffraction peaks (i.e. Bragg peaks) are observed when x-ray beams scattered from lattice planes undergo strong constructive interference. Specifically, as seen in Figure 3.3, when incident two beams with an identical wavelength and phase are scattered from lattice planes with the inter-planar spacing d, beam 2 traverses an extra length of $2d\sin\theta$. The strongest constructive interference occurs when the path difference between two beams is a multiple of the x-ray wavelength (λ) based on Bragg's law [74],

$$n\lambda = 2d\sin\theta, \tag{3.1}$$

where n and θ are a positive integer and the incident angle, respectively. Bragg peaks satisfying this Bragg condition determine the unique angle (i.e. Bragg angle) for each crystal plane (e.g. 2θ = 32.6°, 36.4°, 42.3° for CuO (110), Cu_2O (111), Cu_2O (200)). Thus,

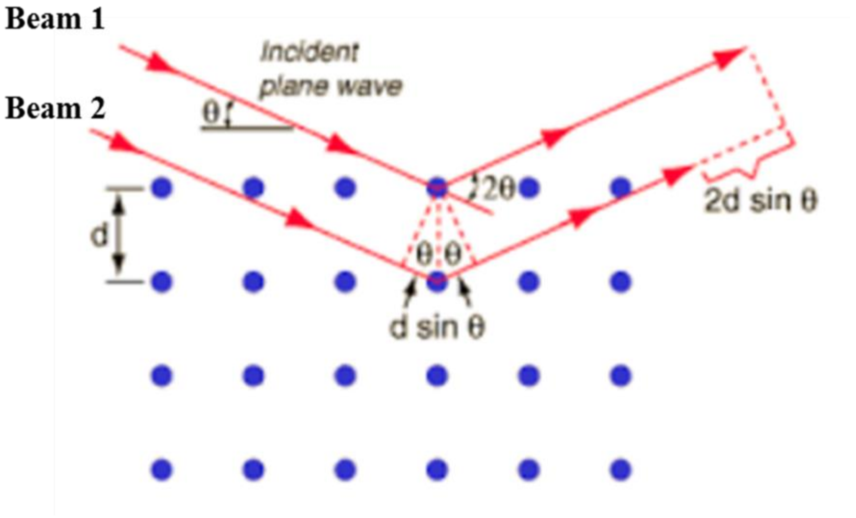

Figure 3.3. Schematic illustration explaining Bragg's law. Image reproduced from [75].

the phase of copper oxide films (i.e. CuO, Cu_2O or a mixed phase) can be determined through observation of Bragg peaks.

In this dissertation, XRD patterns were used for the purpose of examining the phase and crystallographic orientation of sputtered copper oxide films and estimating the grain size L using the Scherrer equation [76],

$$L = \frac{0.94\lambda}{\beta\cos\theta}, \tag{3.2}$$

where λ and θ denote the X-ray wavelength of Cu $K_{\alpha 1}$ radiation (0.154 nm) and the Bragg angle in degrees, respectively. Here, β is the full width at half maximum (FWHM) corrected by $(\beta_m^2 - \beta_i^2)^{1/2}$ where $\beta_m$and β_i are the measured and instrumental FWHM in radians [77]. XRD was carried out by a Bruker D8 Discover X-ray diffractometer using a Cu $K_{\alpha 1}$ x-ray source (λ = 0.154 nm) in the Cavendish Laboratory. Diffraction peaks were analysed based on JCPDS database files with reference numbers 80-1917 (CuO), 04-007-9767 (Cu_2O) and 85-1326 (Cu). The peak intensities were obtained by subtracting each baseline (i.e. background noise) from the peak maximum.

3.2.2 UV-visible spectroscopy

UV-visible spectroscopy is used for analysing optical characteristics (e.g. transmission, absorption coefficient, optical band gap and Urbach energy) of thin films. Transmission spectra of copper oxide films deposited on quartz (Spectrosil B) were obtained as a function of wavelength by an ATI Unicam UV/Vis spectrometer (UV2–200). Based on the Beer-Lambert law, $I = I_0 e^{-\alpha t}$ [78], the absorption coefficient (α) is given as follows,

$$\alpha = \frac{1}{t} \ln \frac{I_0}{I}, \tag{3.3}$$

where I_0 and I denote the optical intensities of incident light and transmitted light respectively, and t is the film thickness. Assuming minimal reflection relative to absorption based on the fact that copper oxide thin films have low reflectance [79], I_0/I can be obtained by the reciprocal of transmission (i.e. $1/T$), and thus α can be roughly calculated using the measured transmission data and film thickness [80]. Although α values can be overestimated to a certain degree due to the assumption of minimal reflection, this has no effect on extracting the optical band gap (E_g^{opt}) and Urbach energy (E_u). This is because E_g^{opt} and E_u are estimated from the intercept of the linear portion of the $(\alpha h\upsilon)^2$ versus photon energy ($h\upsilon$) plot at $\alpha = 0$ and the reciprocal of the slope of the linear region in the $\ln(\alpha)$ versus $h\upsilon$ plot, respectively. The detailed extraction methods for E_g^{opt} and E_u will be discussed in section 4.4 and subsection 5.3.2, respectively.

3.2.3 Raman spectroscopy

For the purpose of confirming a change in the copper oxide phase according to the oxygen flow rate, Raman spectra were recorded with a Renishaw inVia Raman microscope using a ×100 objective. This was performed by Dr. Philipp Braeuninger in the Hofmann Group, University of Cambridge. For sample excitation, an Ar laser with 488 nm emission wavelength was used. Characteristic phonon modes related to Cu_2O and CuO were identified based on references [81–84].

3.2.4 Scanning electron microscopy

With the purpose of examining a change in grain size according to annealing temperature, scanning electron microscopy was performed by a Phillips LEO GEMINI 1530VP FEG-SEM in the Nanoscience Centre, University of Cambridge.

3.2.5 Van der Pauw method Hall measurements

Van der Pauw demonstrated that the sheet resistance (R_s) of samples with arbitrary shape can be calculated using resistances measured along a vertical edge and a horizontal edge (i.e. $R_{vertical}$ and $R_{horizontal}$, see Figure 3.4) based on the following relation [85],

$$\exp\left(-\pi\frac{R_{vertical}}{R_s}\right)+\exp\left(-\pi\frac{R_{horizontal}}{R_s}\right)=1. \tag{3.4}$$

Using the four-probe van der Pauw method, the sheet resistance (or electrical resistivity) of thin films can be determined from a total of eight resistance measurements as seen in

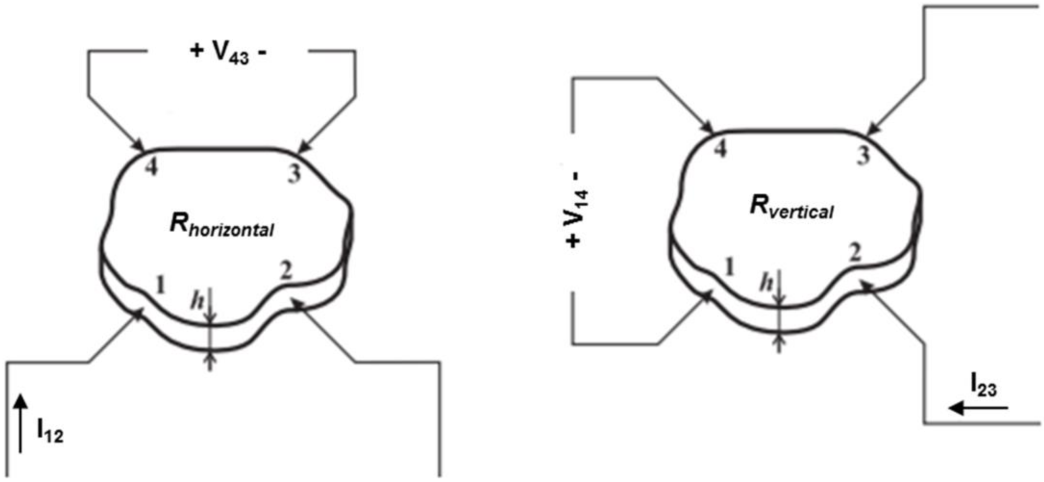

Figure 3.4. Horizontal direction resistance $R_{horizontal}$ and vertical direction resistance $R_{vertical}$ of a flat sample with arbitrary shape.

Figure 3.5. Specifically, for each resistance measurement, a current is supplied along one edge of the thin film (e.g. I_{12}) and the voltage across the opposite edge (e.g. V_{43}) is measured by a voltage metre, then the resistance (in this case, $R_{12,43}$) is obtained using Ohm’s law. An improvement in the accuracy of $R_{horizontal}$ and $R_{vertical}$ is obtained by making reciprocal measurements, based on the reciprocity theorem (i.e. $R_{12,43} = R_{43,12}$ for $R_{horizontal}$ and $R_{14,23} = R_{23,14}$ for $R_{vertical}$), and by repeating reversed polarity measurements (i.e. $R_{21,34}$, $R_{34,21}$ for $R_{horizontal}$ and $R_{41,32}$, $R_{32,41}$ for $R_{vertical}$), and then by averaging them respectively. Using the average values of $R_{horizontal}$ and $R_{vertical}$, the sheet resistance is determined by solving Equation (3.4) numerically. The electrical resistivity ρ [Ω·cm] is calculated by $\rho = R_s t$ where t is a film thickness [86].

A Hall measurement is very useful for semiconductor material characterisation since electrical properties (i.e. the majority carrier type, density and mobility) can be obtained

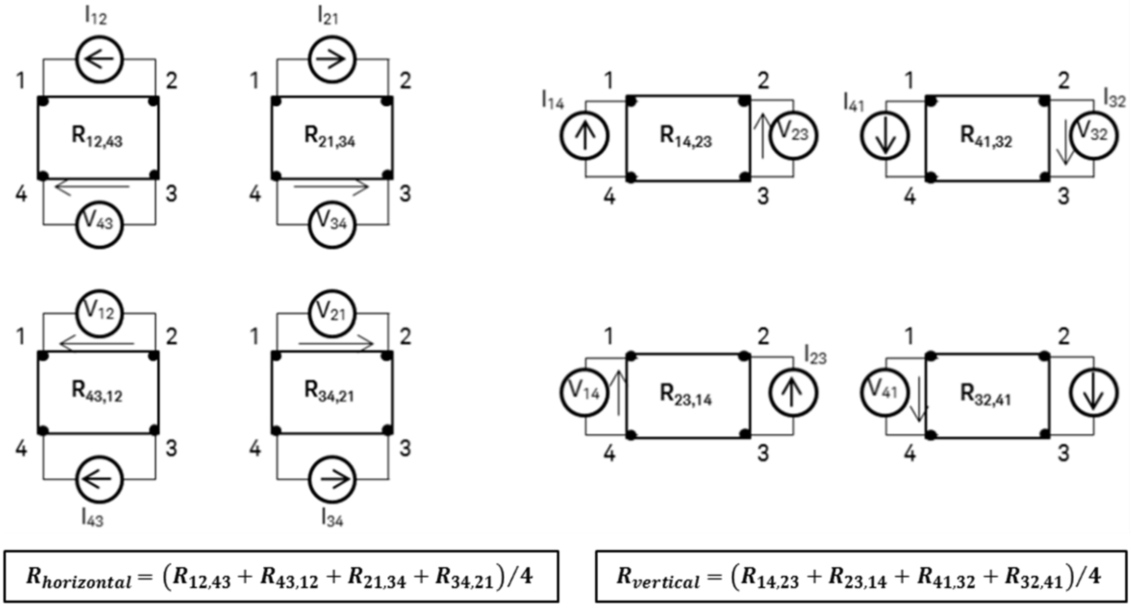

$$\boxed{R_{horizontal} = (R_{12,43} + R_{43,12} + R_{21,34} + R_{34,21})/4}$$

$$\boxed{R_{vertical} = (R_{14,23} + R_{23,14} + R_{41,32} + R_{32,41})/4}$$

(a) $R_{horizontal}$ measurement **(b) $R_{vertical}$ measurement**

Figure 3.5. Eight resistance measurements for obtaining average $R_{horizontal}$ and $R_{vertical}$ of thin films. Image reproduced from [87].

from the induced Hall voltage. The Hall voltage (V_H) can be measured using the same van der Pauw sample with an applied magnetic field (B) as seen in Figure 3.6. Here, V_{24P} denotes the Hall voltage measured across contacts 2 and 4 for the applied I_{13} and a magnetic field in the positive z-direction. For improving the accuracy of the measured Hall voltage, as in the resistivity measurement, reciprocal (i.e. V_{13P} for I_{24}) and reversed polarity measurements (i.e. V_{42P} for I_{31} and V_{31P} for I_{42}) are performed. Additionally, in order to correct for the offset voltage occurring during the measurement, the Hall voltage measurements (V_{24N}, V_{13N}, V_{42N} and V_{31N}) are repeated under a reversed (i.e. negative) magnetic field [86]. The overall Hall voltage is then calculated by

$$V_H = \frac{(V_{13P} - V_{13N}) + (V_{24P} - V_{24N}) + (V_{31P} - V_{31N}) + (V_{42P} - V_{42N})}{8}. \qquad (3.5)$$

The type of the majority carrier is determined by the polarity of this Hall voltage; if V_H is positive, the majority carrier is holes (i.e. p-type). The Hall coefficient R_H [cm^3/C] is calculated using the measured V_H and the following equation [88],

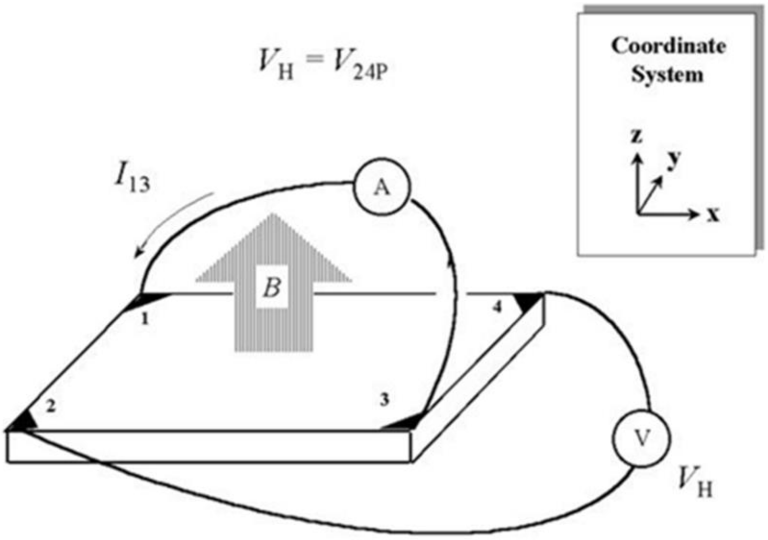

Figure 3.6. Hall voltage measurement using the four-probe van der Pauw configuration. Image reproduced from [89].

$$R_H = \frac{V_H t}{IB} = \frac{1}{qp}; \quad p \gg n, \tag{3.6}$$

where q and p are the elementary charge and carrier (i.e. hole) density for a p-type sample, respectively. The carrier density is determined from the calculated R_H and Equation (3.6). Finally, using the Hall coefficient and $\rho^{-1} \approx qp\mu_{Hall}$ (i.e. when $p \gg n$) [88], the Hall mobility (μ_{Hall}) is given as

$$\mu_{Hall} = (qp)\mu_{Hall}\left(\frac{1}{qp}\right) = \frac{R_H}{\rho}. \tag{3.7}$$

Thus, μ_{Hall} is obtained by a simple calculation using the calculated R_H and ρ.

In order to obtain the electrical characteristics (i.e. electrical resistivity, carrier density and mobility) of Cu_2O thin films, the van der Pauw samples (see Figure 3.7) were fabricated by forming Au electrodes at the four corners of the Cu_2O films deposited on square glass substrates (8 mm×8 mm) using a thermal evaporator (Edwards E306A) and a shadow mask. The resistivity and Hall measurements were performed using an MMR Technologies Hall Effect Measurement System (K2500-7) at room temperature.

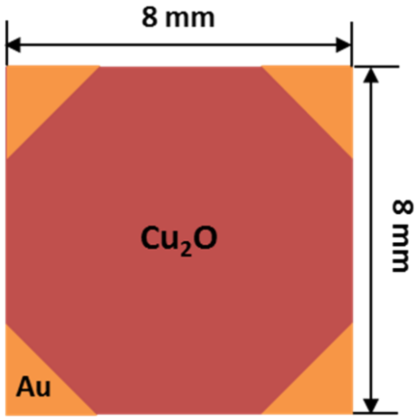

Figure 3.7. Schematic van der Pauw geometry for the Hall measurement.

3.3 Thin film transistor analysis

This section describes important parameters used for evaluating TFT performance and the techniques that were used for identifying the main origins of the poor performance of p-type Cu_2O TFTs.

3.3.1 Current-voltage characteristics

The conventional equations describing the current-voltage (I-V) characteristics of TFTs are derived from the charge control model based on Shockley's gradual channel approximation as in MOSFETs [26, 27, 65, 90, 91]. Since the gradual channel approximation is based on the assumption that the change in the electric field perpendicular to the channel (y-component) is much larger than the change in the lateral electric field along the channel (x-component) [92], this model is only valid for long channel devices.

This model begins by describing the mobile accumulation charge (Q_{acc}) per unit area of the TFT channel with consideration for the channel potential ($V_C(x)$), that is,

$$Q_{acc} = C_i\big(V_{GS} - V_T - V_C(x)\big), \tag{3.8}$$

where C_i, V_{GS} and V_T are the capacitance per unit area of the gate insulator, gate-source voltage and threshold voltage, respectively. Neglecting the diffusion current, the drain-source current (I_{DS}) can be written as

$$I_{DS} = WQ_{acc}\mu_{FE}E(x), \tag{3.9}$$

where $E(x) = dV_C(x)/dx$ is the magnitude of the electric field in the channel, W and μ_{FE} denote the channel width and the field-effect mobility. By substituting Q_{acc} with Equation (3.8) and $E(x)$ with $dV_C(x)/dx$, Equation (3.9) can be rewritten as

$$I_{DS}dx = W\mu_{FE}C_i\big(V_{GS} - V_T - V_C(x)\big)dV_C(x). \tag{3.10}$$

By integrating both sides of Equation (3.10) over x along the channel from x = 0 (source) to L (drain) and over $V_C(x)$ from 0 to V_{DS}, respectively, the I_{DS} equation in the linear operating region of TFTs is given as

$$I_{DS} = \frac{W}{L}\mu_{FE}C_i\left[(V_{GS} - V_T)V_{DS} - \frac{V_{DS}^2}{2}\right]; \quad V_{DS} \leq V_{GS} - V_T, \tag{3.11}$$

where L and V_{DS} are the channel length and drain-source voltage. When $V_{DS} = V_{GS} - V_T$, the drain current saturates due to channel pinch-off and thus Equation (3.11) is no longer valid for $V_{DS} \geq V_{GS} - V_T$. In fact, a further increase in V_{DS} above $(V_{GS} - V_T)$ causes the pinch-off point to move slightly away from the drain. However, since this slight reduction in the effective channel length (i.e. channel shortening) can be negligible for long channel TFTs [93, 94], the drain saturation current ($I_{DS,sat}$) can be obtained by substituting $V_{GS} - V_T$ for V_{DS} as follows,

$$I_{DS,sat} = \frac{W}{2L}\mu_{sat}C_i(V_{GS} - V_T)^2; \quad V_{DS} \geq V_{GS} - V_T. \tag{3.12}$$

Several other models with modifications to account for the localised states near the band edges and nonidealities such as contact resistance have been also proposed, which allows accurate and reliable TFT circuit simulation [95–97]. However, it is a convention to extract μ_{FE} of TFTs based on Equations (3.11) and (3.12) [2, 26]. Therefore, in this thesis, the conventional I_{DS} model is used for estimating μ_{FE} and comparing it with previous reported μ_{FE} values.

3.3.2 TFT parameters

The performance of TFTs is assessed by using several parameters: field-effect mobility, off-state current, on/off current ratio and subthreshold slope.

Field-effect mobility (μ_{FE}): On-state current (I_{on}) depends on the TFT geometry (i.e. channel length L and width W), gate insulator capacitance C_i (i.e. dielectric constant and thickness of the gate insulator) and applied voltages (see Equations (3.11) and (3.12)) [26]. For this reason, instead of I_{on}, the μ_{FE} is used for evaluating the efficiency of carrier transport in TFTs, and this parameter has direct effects on the maximum I_{on} and operating frequency of TFTs [2]. The μ_{FE} measured using a TFT should be expected to differ from the actual carrier mobility (i.e. μ_{Hall}) of a channel material due to the effects of the vertical field induced by V_{GS} and contact resistance (R_C). To be specific, since carriers accumulated by the vertical field flow in the vicinity of the interface between the channel layer and the gate insulator, carrier transport can be significantly degraded by severe carrier trapping at the interface if there exists a high density of interface traps. Furthermore, the R_C of source/drain contacts can also lead to a lower μ_{FE} than its actual intrinsic value in the channel region [98, 99]. These will be discussed in more detail in section 7.4.

The μ_{FE} can be estimated using different approximations from the saturation or linear operating region. The saturation mobility (μ_{sat}) is obtained from the slope of a $\sqrt{I_{DS,sat}}$ versus V_{GS} plot (i.e. when $V_{DS} \geq V_{GS} - V_T$) using the following equation derived from Equation (3.12),

$$\mu_{sat} = \left(\frac{\partial\sqrt{I_{DS,sat}}}{\partial V_{GS}}\right)^2 \frac{2L}{WC_i}. \tag{3.13}$$

μ_{FE} in the linear operating region of TFTs is obtained from the transconductance ($g_m = \partial I_{DS,lin}/\partial V_{GS}$) using the following equation,

$$\mu_{FE} = g_m \frac{L}{WC_iV_{DS}}. \tag{3.14}$$

This equation is derived from the approximated I_{DS} equation (i.e. $I_{DS} \approx (W/L)\mu_{FE}C_iV_{DS}(V_{GS} - V_T)$) based on the assumption of $V_{DS} \ll V_{GS}$.

Off-state current (I_{off}) and on/off current ratio (I_{on}/I_{off}): I_{off} is also a significant parameter since it determines the minimum power consumption of TFTs [26]. I_{off} (scaled for channel width) < 1 pA/μm is required for display applications [100]. The on/off current ratio is simply defined as I_{on}/I_{off} and a large on/off ratio (> 10^6) is required for TFTs to be used as electronic switches [2].

Subthreshold slope (S): The sub-threshold slope is another critical parameter since it determines the minimum change in V_{GS} necessary to turn TFTs from the off-state to the on-state [26]. It is defined as the value of V_{GS} required to increase I_{DS} by one decade in the subthreshold region [2]:

$$S = \left(\left. \frac{\partial \log(I_{DS})}{\partial V_{GS}} \right|_{\max} \right)^{-1}. \tag{3.15}$$

A small S value is required for low power consumption and a high operating frequency of TFTs [2]. In addition, the S value provides significant information on the trap density in the bulk channel layer and at the channel/gate insulator interface [101], which will be discussed more in detail in subsection 7.4.2.

These TFT parameters are obtained from transfer characteristics where I_{DS} is plotted as a function of V_{GS} at a fixed V_{DS}. The channel pinch-off (i.e. I_{DS} saturation) is observed in the output characteristics where I_{DS} is plotted as a function of V_{DS} for various V_{GS}. The transfer and output characteristics were measured using an HP 4140B pA meter/dual DC voltage source in a dark box.

3.3.3 Transmission line method

The transmission line method (TLM) is a well-known technique for determining the contact resistance of a metal/semiconductor contact. Specifically, a semiconductor with two metal contacts can be considered as a semiconductor resistance (R_{semi}) in series with two contact resistances ($2R_C$) and thus a measured total resistance (R_T) between the two contacts is simply expressed as [102]

$$R_T = R_{semi} + 2R_C = \frac{R_s}{W}L + 2R_C. \tag{3.16}$$

Here, R_s is the sheet resistance of the semiconductor, and L and W denote the length and width of the semiconductor area between the contacts. By fabricating a series of metal contacts separated by different L on a semiconductor layer (see Figure 3.8 on the left), R_T as a function of L can be measured and plotted as shown in Figure 3.8 on the right. Based on Equation (3.16), R_C can be obtained from the intercept when $L = 0$ (i.e. $2R_C$) of the linear fit of the measured R_T values. As a secondary benefit, R_s can also be obtained from the slope of the linear fit [102].

For estimating the S/D contact resistance and the channel resistance per unit channel length of fabricated Cu_2O TFTs, TFT structures with a channel width W = 1 mm and different channel lengths L in the range of 10~100 μm were used as the TLM patterns, and each R_T was measured using an HP 4140B pA meter/dual DC voltage source.

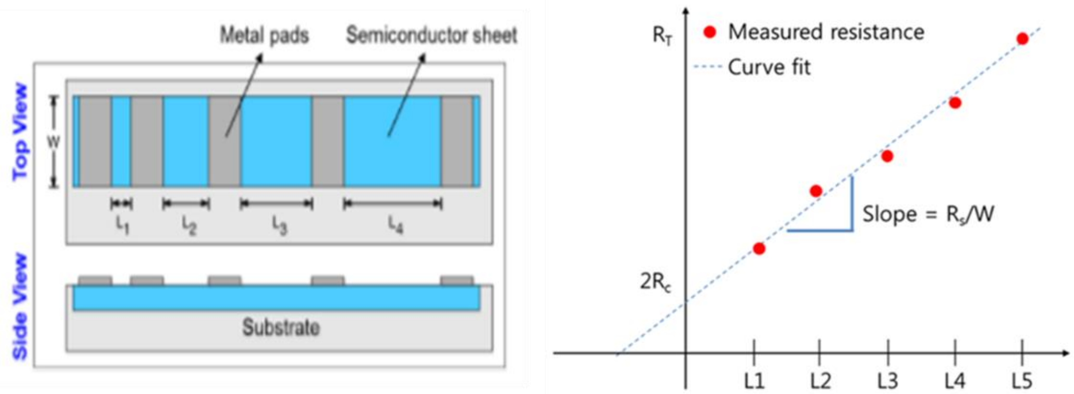

Figure 3.8. Schematic structure of a standard TLM array (left) and an R_T versus L plot determining the contact and sheet resistances (right). Image reproduced from [103].

3.3.4 Capacitance-voltage measurements

If the source and drain of a TFT have equal potential, the gate-insulator-channel structure of the TFT can be regarded as a MIS capacitor having the metal-insulator-semiconductor structure. Thus, a capacitance-voltage (C-V) curve of the MIS capacitor can be used for studying the charge response in the TFT channel layer to an applied gate voltage: majority carrier accumulation, depletion and inversion (i.e. minority carrier accumulation). Specifically, the capacitance (C_{MIS}) of the MIS structure can be represented as a series connection of the insulator capacitance (C_i) and the depletion layer capacitance (C_{dep}) [104],

$$C_{MIS} = \frac{C_i C_{dep}}{C_i + C_{dep}}. \tag{3.17}$$

If the MIS structure is biased into accumulation mode, majority carriers are accumulated at the insulator/semiconductor interface, and a change in the AC voltage only affects the majority carrier charge at the interface, thereby $C_{MIS} \approx C_i$. In the depletion mode, the majority carriers are depleted, and the C_{MIS} decreases steadily until the depletion width reaches its maximum value or the semiconductor is fully depleted. If an accumulation of minority carriers occurs at the interface between the insulator and the semiconductor, a change in the AC voltage primarily affects the minority carrier charge at the interface, and thus the C_{MIS} increases to $C_{MIS} \approx C_i$ again.

In this thesis, C-V characteristics of a metal-oxide-semiconductor (MOS) capacitor with a p^+-Si/SiO_2/Cu_2O structure and an Au top contact were measured using an Agilent B1500A semiconductor parameter analyzer at room temperature for the purpose of identifying the origin of the high off-state current in Cu_2O TFTs (subsection 7.5.1). The measurement frequency and AC voltage were set to 500 kHz and 250 mV, respectively, and the DC-bias voltage was swept from –8 to 8 V.

3.3.5 Temperature-dependent electrical characterisation

Transfer characteristics at various temperatures (323~373 K in steps of 5 K) were measured on a thermocouple hotplate probe-station using an HP 4140B pA meter/DC voltage source. V_{GS} was swept from –10 to +10 V in steps of 0.5 V at a fixed V_{DS} of –1 V, and each temperature was allowed to stabilise for 5 min. In subsection 7.5.2, the measured data were used for examining a change in activation energy (i.e. E_F position) within the channel as a function of V_{GS} and demonstrating the dominant conduction mechanism of the high off-state current in Cu_2O TFTs.

Chapter 4

Sputtering condition optimisation for Cu_2O

4.1 Introduction

It is difficult to obtain pure Cu_2O films since moderate excess of oxygen leads to the formation of CuO in lieu of Cu_2O and even slight excess or shortage of oxygen gives rise to a mixed phase (i.e. Cu_2O/CuO or Cu/Cu_2O, respectively) as seen in Figure 4.1. Thus, it is required to control the stoichiometry of copper oxide precisely in order to form pure Cu_2O films [72].

In this chapter, the film stoichiometry is precisely controlled by the oxygen flow rate during deposition, and the copper oxide phases in films sputtered at various oxygen flow

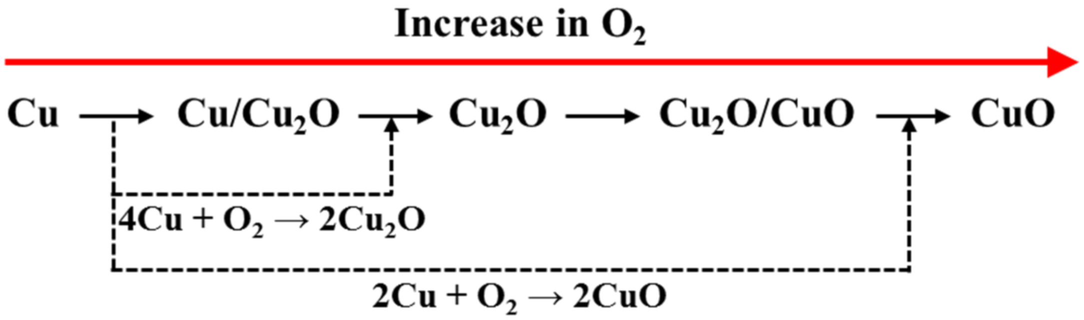

Figure 4.1. Schematic illustration representing a change in the copper oxide phase according to an increase in oxygen.

rates are examined using UV-visible spectroscopy, Raman spectroscopy and XRD in order to find the optimum sputtering condition for stoichiometric Cu_2O thin films.

4.2 Experimental details

Quartz and silicon substrates were firstly cleaned by acetone in an ultrasonic bath for 10 min in order to remove oils and organic contaminants on substrate surfaces, and then soaked in isopropyl alcohol (IPA) for 5 min to remove acetone residues on the surfaces. This is followed by a rinse in deionised (DI) water and a nitrogen blow to dry the substrates. A dehydration step was then performed on a hot plate in air at 150 ℃ for 5 min to remove moisture on the substrate surface completely.

Copper oxide thin films were deposited on the cleaned substrates by reactive sputtering using the HiTUS system without intentional substrate heating, from a 4-inch diameter copper target of 99.999 % purity (Kurt J. Lesker Company) in an atmosphere of argon and oxygen gases (BOC Gases Ltd). After pumping to a base pressure of about 6.0×10^{-6} mbar, the chamber was filled to a process pressure of 1.5×10^{-3} mbar with the Ar gas. The sputtering process consists of four steps: 1) Ar plasma surface treatment, 2) target cleaning, 3) stabilisation of the sputtering condition and 4) film deposition. To be specific, a low-intensity Ar plasma treatment on the substrate surfaces (RF launch power of 600 W without DC bias power) is performed for 5 min in order to not only remove organic residues completely but also improve thin film adhesion. This is followed by a copper target cleaning step (RF launch power of 1200 W and DC bias power of 800 W) for 10 min to remove surface contaminants on the target. After reactive sputtering is performed for 15 min with the shutter closed in order to stabilise the sputtering condition, a copper oxide thin film is finally deposited on substrates. Here, the oxygen flow rate was varied at two different target bias conditions (230 and 690 V) in order to find a sputtering condition for stoichiometric Cu_2O. The thickness of deposited films was obtained by measuring a step edge, provided by kapton tape masking, using surface profilometry (Veeco Dektak 200SI).

Table 4.1. Comparison of characterisation methods for confirming the copper oxide phase.

Techniques	**XRD**	**XPS**	**Raman**
Detection area (Bulk or surface)	Bulk	Surface (usually 0-10 nm depth)	Both
Detection structure (Crystalline or amorphous)	Crystalline	Both	Both
Detection information	Film phase Film orientation Crystallite size	Film phase Chemical and electronic states of elements	Film phase Film orientation

There are three characterisation techniques for confirming the copper oxide phase (i.e. Cu_2O or CuO): XRD, XPS and Raman. Since the XPS only provides information on the film surface, XRD and Raman were used for confirming the phase in copper oxide films in this thesis. The XRD was also used for obtaining the information on grain orientation and size in Cu_2O films.

4.3 Results and discussion

Figure 4.2 shows the optical transmittance spectra and absorption coefficient (α) of copper oxide films deposited at various oxygen flow rates and a fixed target bias voltage of 230 V. A notable change in optical characteristics of copper oxide films is observed for low oxygen flow rates (6.5–7.5 sccm): an increase in optical transmittance in the visible wavelength regime and a left shift of the absorption edge from approximately 680 nm (9.5–13.5 sccm) to 520 nm. This is indicative of an increase in the optical band gap.

Since Cu_2O has a wider optical band gap (2.2–2.6 eV) than that of CuO (1.4–1.9 eV) [13, 105–109], by extracting the optical band gap, it can be roughly decided whether the

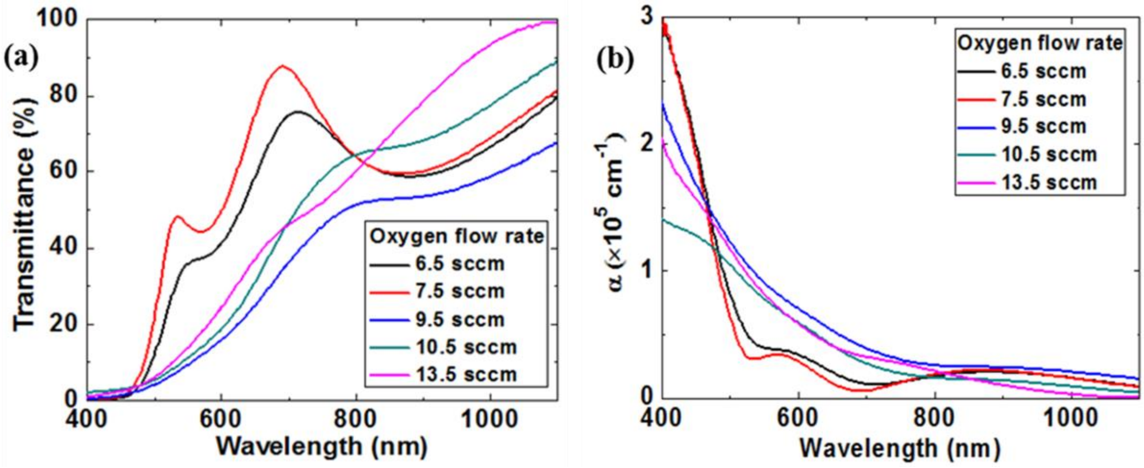

Figure 4.2. (a) Transmittance spectra and (b) absorption coefficient α of copper oxide films formed at various oxygen flow rates and a target bias voltage of 230 V.

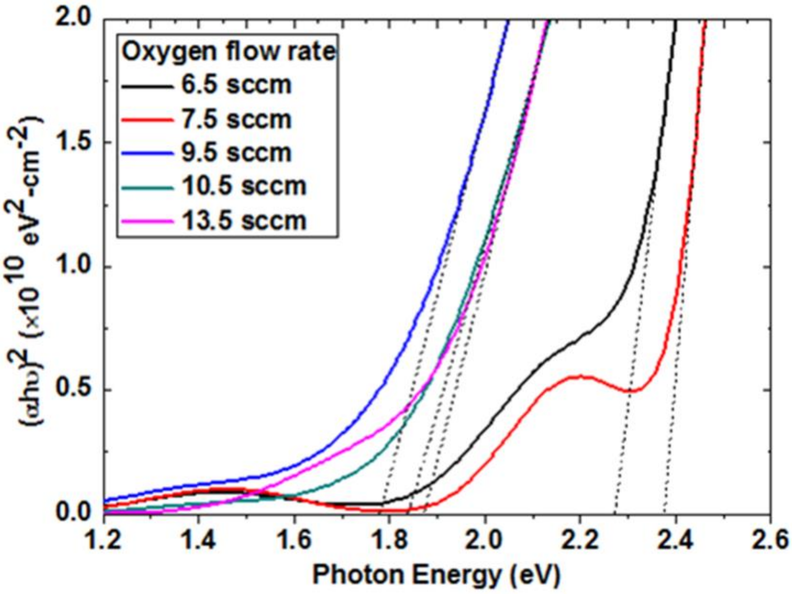

Figure 4.3. $(\alpha h\nu)^2$ versus photon energy plots of copper oxide films deposited at various oxygen flow rates and a fixed target bias voltage of 230 V for extracting the optical band gap.

film is predominantly either Cu_2O or CuO. The optical band gap (E_g^{opt}) can be estimated using the Tauc relation [110, 111]:

$$\alpha h\upsilon = \alpha_0\left(h\upsilon - E_g^{opt}\right)^n, \tag{4.1}$$

where α_0 and $h\upsilon$ are a prefactor and the incident photon energy (eV). Here, the value of the exponent n depends on the type of an optical transition: n = 1/2, 3/2, 2, 3 for direct allowed, direct forbidden, indirect allowed and indirect forbidden optical transitions, respectively [111]. All the reported E_g^{opt} values of copper oxide films were obtained by assuming a direct allowed transition [105–109]. Based on this convention, n was assumed to be 1/2, and therefore the E_g^{opt} was extracted from the intercept of the linear portion of the $(\alpha h\upsilon)^2$ versus photon energy ($h\upsilon$) plots at α = 0 as seen in Figure 4.3. The extracted E_g^{opt} increases from 1.8–1.9 eV to 2.3–2.4 eV for a decrease in the oxygen flow rate from 9.5–13.5 sccm to 6.5–7.5 sccm. These values are in the range of the reported E_g^{opt} values of CuO and Cu_2O thin films respectively [105–109], which indicates the formation of Cu_2O (6.5–7.5 sccm) and CuO (9.5–13.5 sccm).

In order to confirm this, a Raman scattering investigation was performed (Raman raw data were obtained by Dr. Philipp Braeuninger in the Hofmann Group, University of Cambridge). Here, an Ar (488 nm) laser was used as an excitation source. This is because the 488 nm excitation (2.55 eV) is in near-resonance with the bandgap energy of Cu_2O and therefore several forbidden Raman modes (e.g. 150 and 211 cm^{-1} lines) of Cu_2O are detected when excited with 488 nm [81]. As seen in Figure 4.4, seven distinct Raman lines are observed at ~150, 210, 294, 344, 418, 630 and 640 cm^{-1}. The 150, 210, 418 and 640 cm^{-1} lines are related to Cu_2O while 294, 344 and 630 cm^{-1} lines are associated with CuO [81]. To be specific, the copper oxide films deposited at higher oxygen flow rates (10.5 and 13.5 sccm) show three Raman peaks at 294 (A_g mode), 344 (B_g mode) and 630 cm^{-1} (B_g mode) which are the Raman-allowed optical phonon modes of CuO [81, 82]. This confirms that the films are composed of the CuO phase. With regard to a lower oxygen flow rate of 7.5 sccm, five Raman lines are detected at 150, 210, 294, 418 and 640 cm^{-1}.

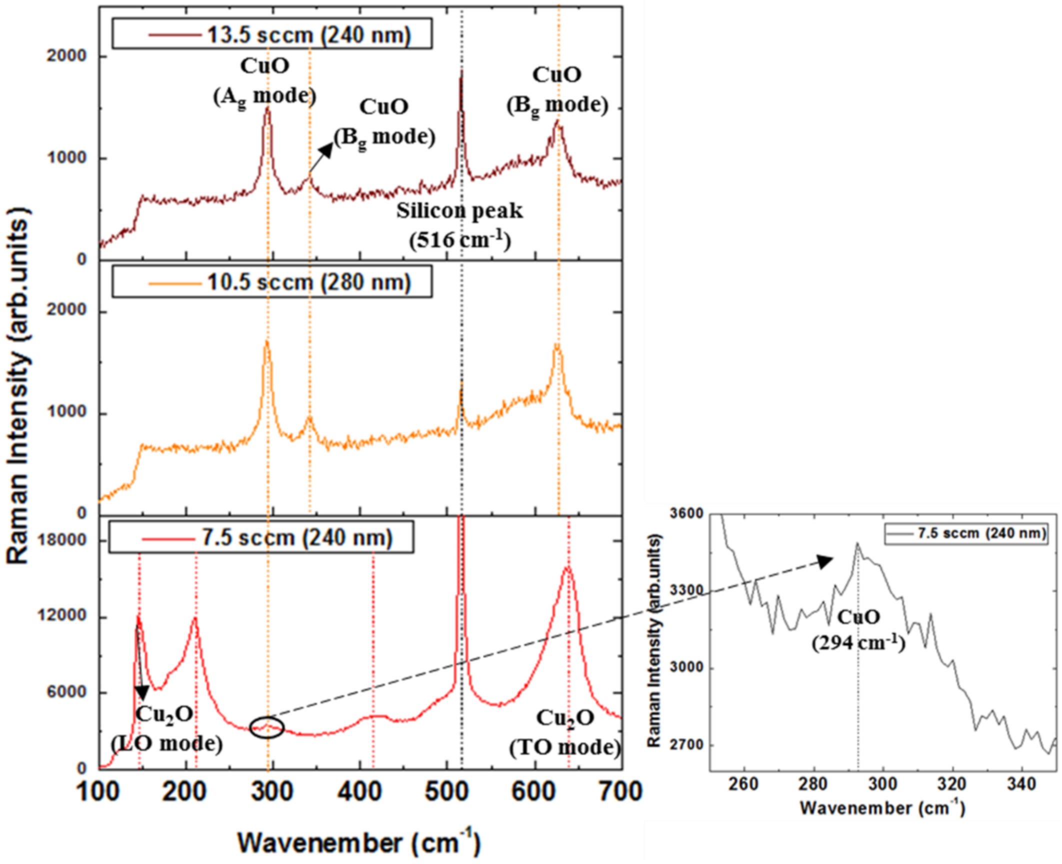

Figure 4.4. Raman spectra of copper oxide thin films deposited at various oxygen flow rates using Ar 488 nm laser excitation at room temperature. Inset shows an enlarged CuO peak of the film formed at an oxygen flow rate of 7.5 sccm.

The 150 and 640 cm^{-1} lines are related to the longitudinal optical (LO) and transverse optical (TO) phonon scattering of Cu_2O, respectively. The 210 cm^{-1} line is associated with a two-phonon scattering of the 110 cm^{-1} mode of Cu_2O [81, 83, 84]. However, the 294 cm^{-1} Raman peak (i.e. CuO A_g mode) is also observed in this film as seen in the inset of Figure 4.4. The intense peaks of the Cu_2O forbidden Raman modes are due to resonance enhancement by 488 nm excitation [81], and therefore the higher intensities of the Cu_2O Raman peaks compared to the CuO peak do not necessarily mean that the film is mainly composed of the Cu_2O phase. For this reason, the copper oxide phases in the film formed at an oxygen flow rate of 7.5 sccm were examined by an X-ray diffractometer. As seen in Figure 4.5, three peaks are detected at 32.6°, 36.4° and 43.3° which are related to the CuO

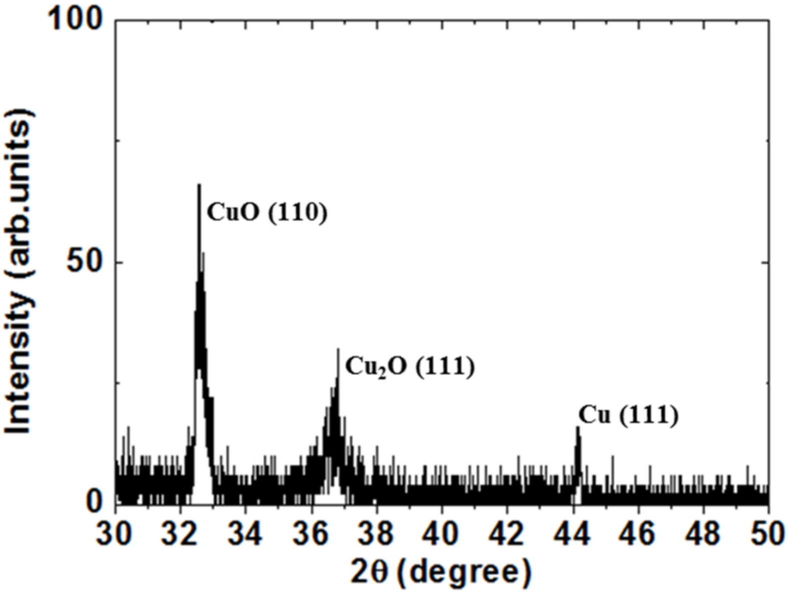

Figure 4.5. An X-ray diffraction pattern of the copper oxide film deposited at an oxygen flow rate of 7.5 sccm and a target voltage of 230 V.

(110) [JCPDS 80-1917], Cu_2O (111) [JCPDS 04-007-9767] and Cu (111) [JCPDS 85-1326], respectively. This shows that the film actually consists of a mixed phase of Cu_2O and CuO with a small trace of the Cu phase.

In order to find a sputtering condition for pure Cu_2O thin films, the oxygen flow rate was varied at a different target bias condition of 690 V. A deposition rate was doubled from ~25 to 50 nm/min with an increase in target bias voltage from 230 to 690 V. This is because a higher target bias voltage gives rise to an increase in accelerating energy of Ar ions that collide with the copper target, thereby leading to a rise in the number of copper atoms out per an incident Ar ion. The increase in deposition rate (i.e. the number of sputtered copper atoms) requires a higher oxygen flow rate for obtaining Cu_2O thin films. For this reason, higher oxygen flow rates (15–17 sccm) were provided for this target bias condition. As seen in Figure 4.6, the copper oxide films deposited at oxygen flow rates (15–16 sccm) show E_g^{opt} of ~2.3 eV which is in the range of the reported E_g^{opt} values of Cu_2O [13, 105–108]. Figure 4.7 shows an XRD pattern of the copper oxide film formed at

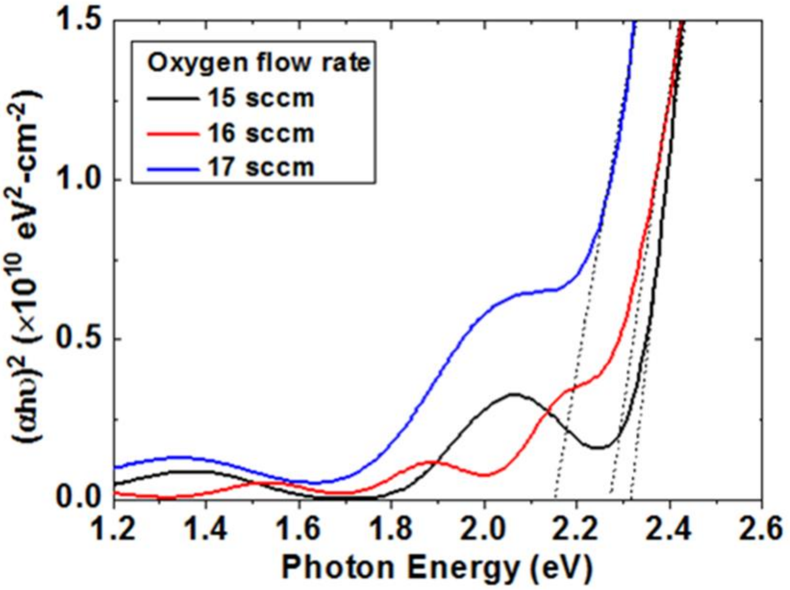

Figure 4.6. $(\alpha h\upsilon)^2$ versus photon energy plots of copper oxide films deposited at oxygen flow rates (15–17 sccm) and a fixed target bias voltage of 690 V for estimating the optical band gap.

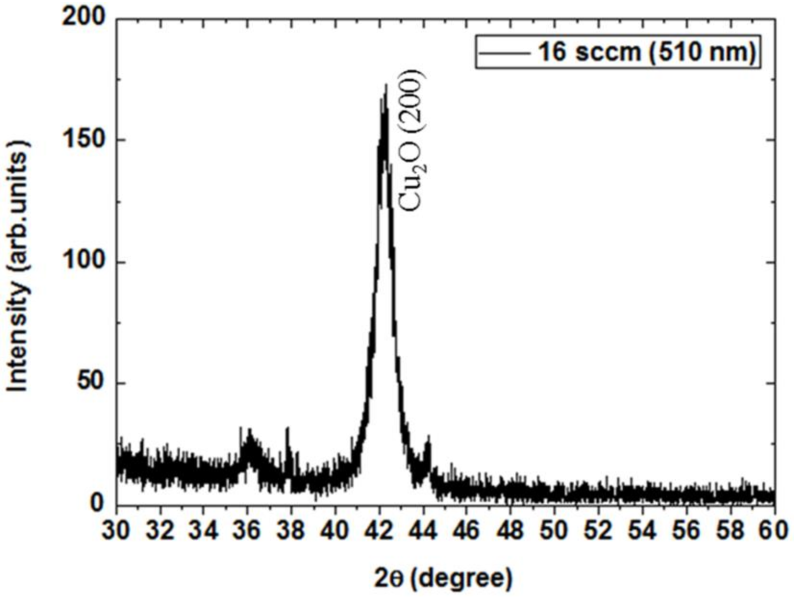

Figure 4.7. An X-ray diffraction pattern of Cu_2O formed at an oxygen flow rate of 16 sccm and a target voltage of 690 V.

an oxygen flow rate of 16 sccm. The XRD pattern shows an intense peak close to 42.33° which is related to the (200) diffraction peak of Cu_2O [JCPDS 04-007-9767] without other peaks associated with Cu and CuO phases, demonstrating the formation of a stoichiometric Cu_2O thin film. Finally, electrical characteristics of this film were examined by Hall measurements. This film exhibited a p-type characteristic with a Hall mobility of 0.14 $cm^2/V \cdot s$ and carrier density of 1.68×10^{16} cm^{-3}, and especially the Hall mobility significantly improved compared to that (~0.03 $cm^2/V \cdot s$) of the mixed-phase copper oxide film (7.5 sccm and 230 V). This sputtering condition (oxygen flow rate of 16 sccm and target bias voltage of 690 V) will be used to investigate annealing effects on Cu_2O film characteristics (Chapter 5) and form a Cu_2O active layer for p-type metal oxide TFTs (Chapter 7).

Chapter 5

Annealing effects on Cu_2O film characteristics

5.1 Motivation and background

The as-deposited p-type Cu_2O thin film shows a Hall-effect carrier mobility of ~0.14 $cm^2/V{\cdot}s$. Considering a carrier mobility (10~40 $cm^2/V{\cdot}s$) of n-type metal oxides [112–116], this mobility is unacceptably low for a p-type channel layer of CMOS and therefore it is required to enhance the carrier mobility of the Cu_2O thin film. Thermal annealing is a conventional method for improving the carrier mobility as it can reduce the defect density [33, 117, 118]. However, copper oxide films are also vulnerable to phase conversion (i.e. $Cu_2O \rightarrow CuO$ or vice versa) by either oxidation or oxide reduction according to the annealing environment (i.e. air or vacuum) [119]. Specifically, air annealing leads to Cu_2O oxidation ($Cu_2O \rightarrow CuO$) induced by oxygen in-diffusion into films and the following reaction, $2Cu_2O + O_2 \rightarrow 4CuO$ [106]. In contrast, vacuum annealing gives rise to oxide reduction ($CuO \rightarrow Cu_2O \rightarrow Cu$) resulting from oxygen out-diffusion under vacuum through the reactions of $4CuO \rightarrow 2Cu_2O + O_2$ and $2Cu_2O \rightarrow 4Cu + O_2$ [120, 121]. For this reason, although few groups have fabricated p-type Cu_2O TFTs using thermal annealing, their TFT performance is still poor and the phase conversion of Cu_2O was observed [13, 122, 123]. To be specific, Cu_2O TFTs annealed at 200 ℃ in air showed a field-effect mobility (μ_{FE}) of ~1.2×10^{-3} $cm^2/V{\cdot}s$ [122] and a CuO peak was observed in the XRD pattern [13]. μ_{FE} of ~0.06 $cm^2/V{\cdot}s$ was reported from Cu_2O TFTs annealed at 800 ℃ in vacuum and the XRD pattern showed Cu peaks along with Cu_2O peaks [123]. Wang *et al.* examined annealing effects on Cu_2O films only at a low temperature range up to 280 ℃ since above 300 ℃, phase conversion to CuO occurred by annealing in air [124].

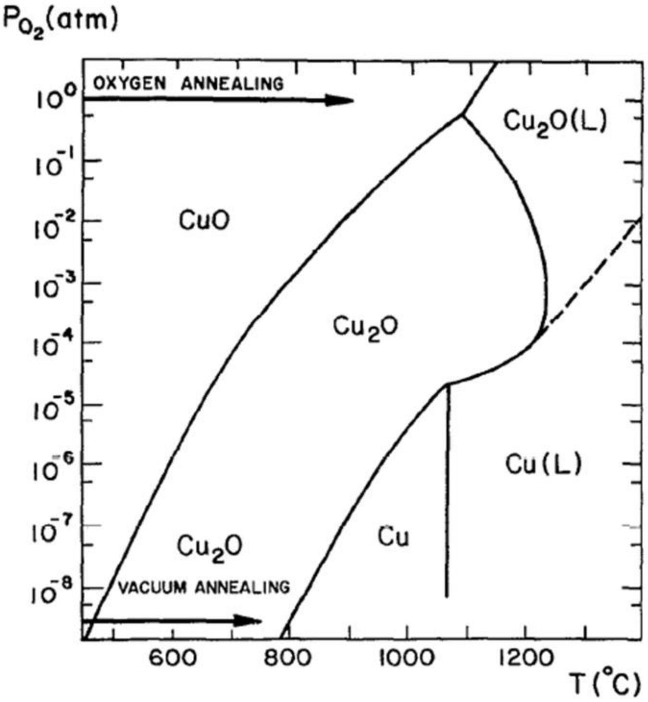

Figure 5.1. Pressure-temperature diagram in the copper-oxide system. Image reproduced from [119].

In this chapter, it is demonstrated that it is possible to anneal Cu_2O thin films in vacuum up to 700 °C without any phase conversion. Here, the oxidation is prevented by annealing in vacuum, and the Cu_2O films are also screened from oxide reduction since it requires a higher temperature ≥ 800 °C in vacuum (see Figure 5.1). This allows an investigation of the pure annealing effects on Cu_2O film characteristics without phase conversion at a much higher temperature range applied here (500–700 °C) than previously studied [124]. In addition, for an in-depth discussion on the main causes of the very low carrier mobility in as-deposited films and the mobility improvement by vacuum annealing, a quantitative and analytical investigation on the conduction mechanism is performed based on analysis of the relative dominance of trap-limited and grain-boundary-limited conduction. In the last part of this chapter, a simple extraction method for the density of copper vacancies is proposed in order to provide a quantitative insight into the annealing effect on the copper vacancy density in Cu_2O thin films.

5.2 Experimental details

For an investigation of annealing effects on Cu_2O film properties, the as-deposited Cu_2O films (sputtering condition: RF launch power of 1.2 kW, process pressure of 1.5×10^{-3} mbar, oxygen flow rate of 16 sccm and DC bias power of 0.95 kW with a DC bias voltage of ~690 V) were annealed in vacuum (~9.5×10^{-4} mbar) in an Aixtron Cambridge Nanoinstruments Black Magic 2 system at temperatures of 500, 600 and 700 ℃ for 10 min. The annealing temperature was monitored with an infrared (IR) radiation pyrometer (Infratherm IGA8 plus). The temperature ramp rate, cooling time and unloading temperature were 5 ℃/s, 20 min and 50 ℃, respectively. In order to conduct Hall measurements using the van der Pauw method, Au electrodes were formed at the four corners of the Cu_2O thin films deposited on 8 mm×8 mm glass (Corning 7059) substrates using a thermal evaporator (Edwards E306A) and a shadow mask. Crystallographic, optical and electrical characteristics of the Cu_2O films were examined using the characterisation techniques (i.e. XRD, UV-visible spectroscopy, Hall measurements and SEM) described in Chapter 3.

5.3 Film properties

5.3.1 Crystallographic characteristics

As seen in Figure 5.2, the Cu phase is not detected in any of the annealed Cu_2O films, showing that it is possible to perform the thermal treatment of Cu_2O films up to 700 ℃ in vacuum without a concern about phase conversion. In addition, a significant increase in the intensity of the Cu_2O (200) peak is observed: 95 cps (as-deposited), 650 cps (500 ℃), 3200 cps (600 ℃) and 4175 cps (700 ℃). Here, cps means counts per sec and the peak intensity was obtained by subtracting each baseline (i.e. background noise) from the peak maximum value. This clearly indicates that film crystallinity improves significantly with an increase in annealing temperature.

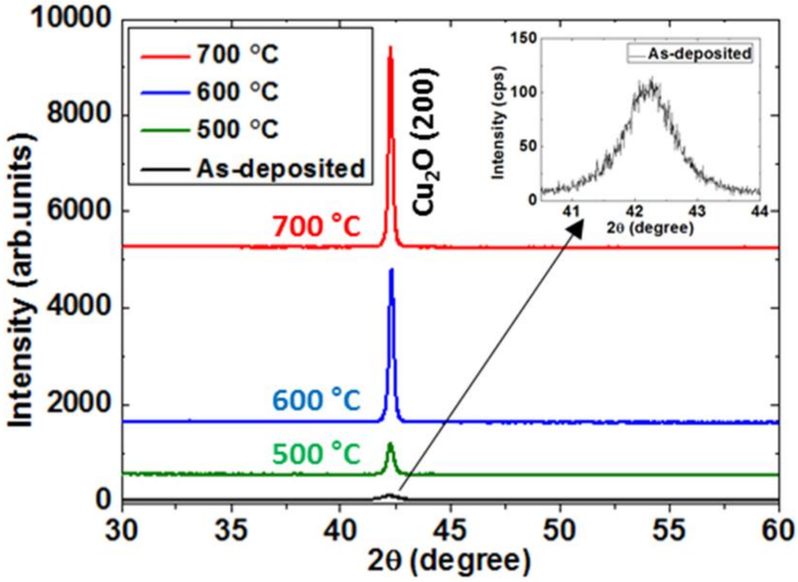

Figure 5.2. XRD patterns of Cu_2O films before and after annealing in vacuum at 500, 600 and 700 °C. Inset indicates an enlarged XRD pattern of the as-deposited thin film [125].

5.3.2 Optical band gap and Urbach energy

As seen in Figure 5.3, the optical band gap is simply extracted from the x-intercept of the linear part of the Tauc plot as explained in section 4.3. This clearly shows widening of the optical band gap with an increase in annealing temperature: 2.28 eV (as-deposited), 2.36 eV (500 °C), 2.39 eV (600 °C) and 2.43 eV (700 °C).

Wang *et al.* [124] also observed the widening of the optical band gap at a low annealing temperature range (180–280 °C), and they interpreted this as a reduction in the valence band tail width as seen in Figure 5.4. To be specific, a high density of tail states near the VBM in the as-deposited film leads to a narrowing of the optical band gap (see Figure 5.4 (a)). The band tail decreases by thermal annealing, which results in the optical band gap widening (see Figure 5.4 (b)). This interpretation was supported by a reduction in Urbach energy which is a parameter reflecting the width of the band tail. The author agrees with this interpretation based on the highly disordered nature of the VBM in Cu_2O. Specifically, as seen in Figure 5.5, while the CBM in Cu_2O consists of spherical

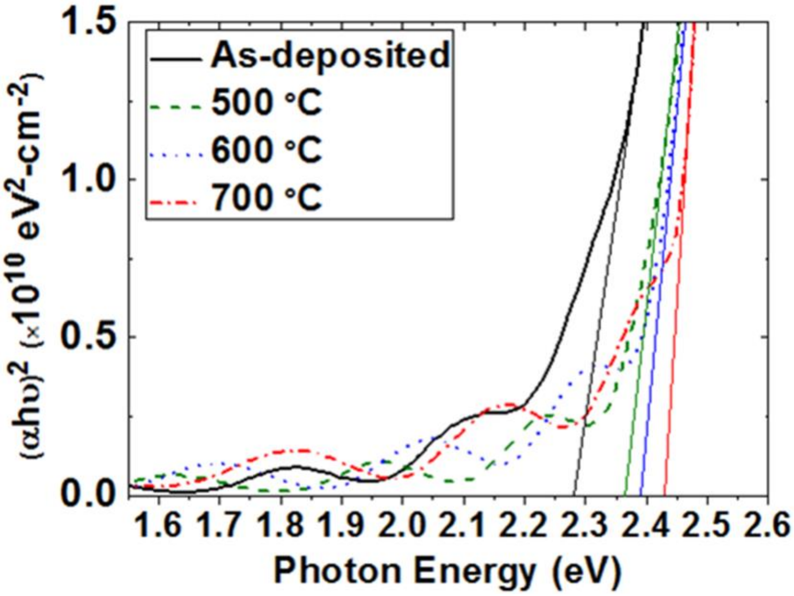

Figure 5.3. $(\alpha h\upsilon)^2$ versus photon energy plots of Cu_2O films with different annealing temperatures for extracting the optical band gap [125].

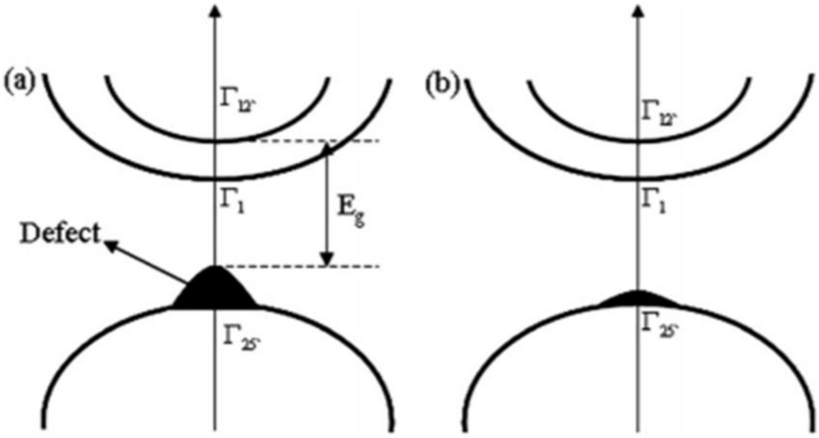

Figure 5.4. Schematic band structures of (a) as-deposited and (b) annealed Cu_2O films. Image reproduced from [124].

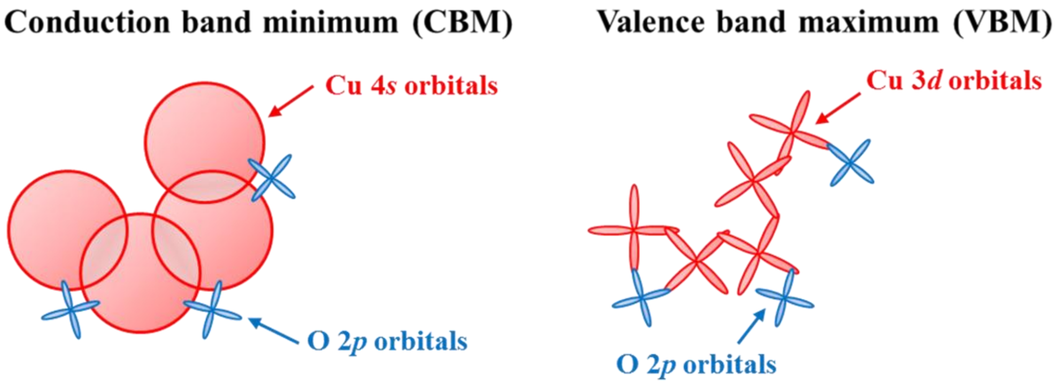

Figure 5.5. Schematic bonding structures of the conduction band minimum and valence band maximum in Cu_2O.

overlapping Cu 4*s* orbitals, the VBM is formed from non-spherical Cu 3*d* orbitals with spatial directivity causing a variation in bonding angle [13]. This is a strong source of disorder in the VBM, which causes a broad distribution of localised tail states (i.e. a strong tailing) near the VBM [47]. It is also known that a high density of tail states in disordered materials can be reduced by thermal annealing [126, 127].

In order to verify this, the Urbach energy (E_u) was extracted using the following method. The optical absorption tail empirically follows an exponential law represented by

$$\alpha(\upsilon) = \alpha_0 \exp\left(\frac{h\upsilon}{E_u}\right), \tag{5.1}$$

where α, α_0, h and υ are the optical absorption coefficient, a constant, the Planck constant and the photon frequency, respectively [128, 129]. Equation (5.1) can be rewritten as

$$\ln(\alpha) = \left(\frac{1}{E_u}\right) h\upsilon - \ln(\alpha_0), \tag{5.2}$$

and therefore E_u is estimated from the reciprocal of the slope of the linear region in the ln(α) versus $h\upsilon$ (i.e. photon energy) plot as seen in Figure 5.6. This shows a reduction in

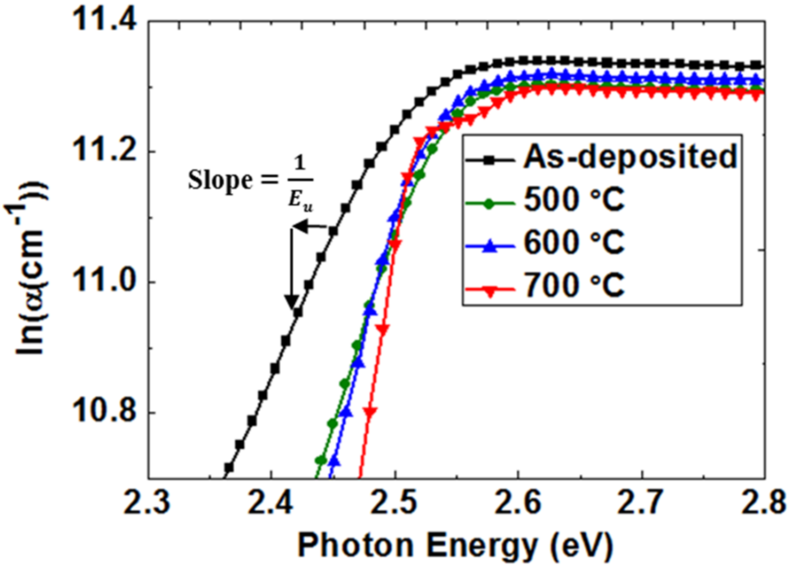

Figure 5.6. ln(α) versus photon energy plots of Cu_2O films with different annealing temperatures for extracting the Urbach energy [125].

E_u with an increase in annealing temperature: 223 meV (as-deposited), 166 meV (500 °C), 128 meV (600 °C) and 78 meV (700 °C), which quantitatively demonstrates that the widening of the optical band gap results from a decrease in the band tail.

Figure 5.7 also shows that there is a linear relation between the Urbach energy and the optical band gap. This allows extraction of the optical band gap in the absence of the band tail (i.e. E_u = 0) from the y-intercept of the linear fit. Using this method, the value of about 2.52±0.02 eV is expected for the optical band gap at E_u = 0 eV. In fact, as seen in Figure 5.4 (a), this extracted optical band gap represents the energy gap between the VBM ($\Gamma_{25'}$) and the second lowest conduction band ($\Gamma_{12'}$) at the Γ-point. This is because, as described in subsection 2.3.3, the lowest absorption transition is not allowed because of the same parity of the Γ_7^+ (the highest valence-band state derived from $\Gamma_{25'}$) and Γ_6^+ (the lowest conduction-band state derived from Γ_1), and therefore strong light absorption occurs at the optical transition between the $\Gamma_{25'}$ and the second lowest conduction band ($\Gamma_{12'}$) with the allowed parity (Γ_8^-). Thus, considering the energy difference between the first CBM (Γ_1) and the second CBM ($\Gamma_{12'}$) is ~0.51 eV calculated by density-functional theory (DFT)

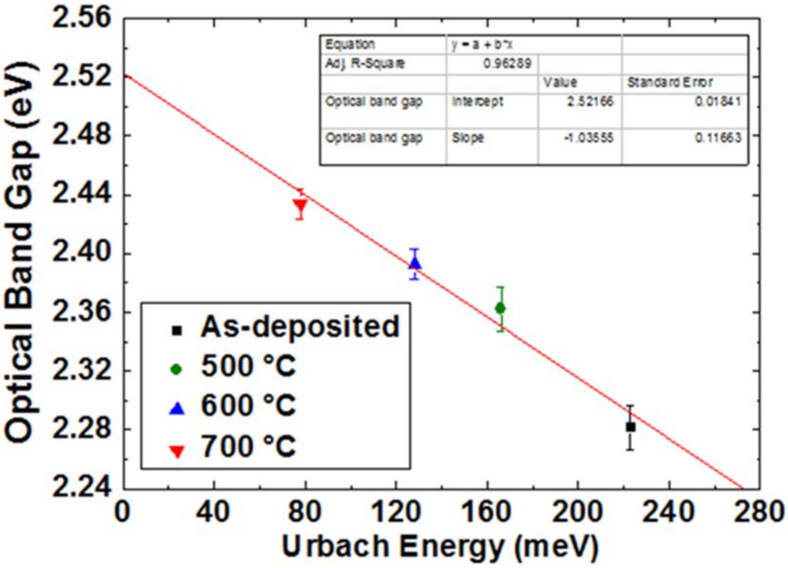

Figure 5.7. The relation between the optical band gap and the Urbach energy for Cu_2O thin films annealed at different temperatures.

[130], the actual band gap of Cu_2O (i.e. the energy gap between the VBM and the first CBM) in the absence of the band tail is evaluated to be ~2.01±0.02 eV. This value is consistent with the theoretical value of 2.01 eV calculated by DFT [130] and the estimated value (2.00 ~ 2.06 eV) from the optical band gap [124].

5.3.3 Hall mobility and carrier density

Figure 5.8 (a) shows a significant improvement in Hall mobility (μ_{Hall}) from ~0.14 to 28 $cm^2/V \cdot s$ with an increase in annealing temperature. Compared to the work of Wang (μ_{Hall} = 2.67 $cm^2/V \cdot s$ for Cu_2O annealed at 280 ℃ in air) [124], an increase in annealing temperature, enabled by vacuum annealing, allows a much more considerable mobility enhancement. The main causes of the μ_{Hall} improvement will be discussed in detail in the following sections (5.4 and 5.5). In addition, as seen in Figure 5.8 (b), an increase in annealing temperature leads to a significant reduction in carrier density from 1.68×10^{16} to 1.85×10^{13} cm^{-3}, which results in an increase in electrical resistivity from 2.7×10^3 to

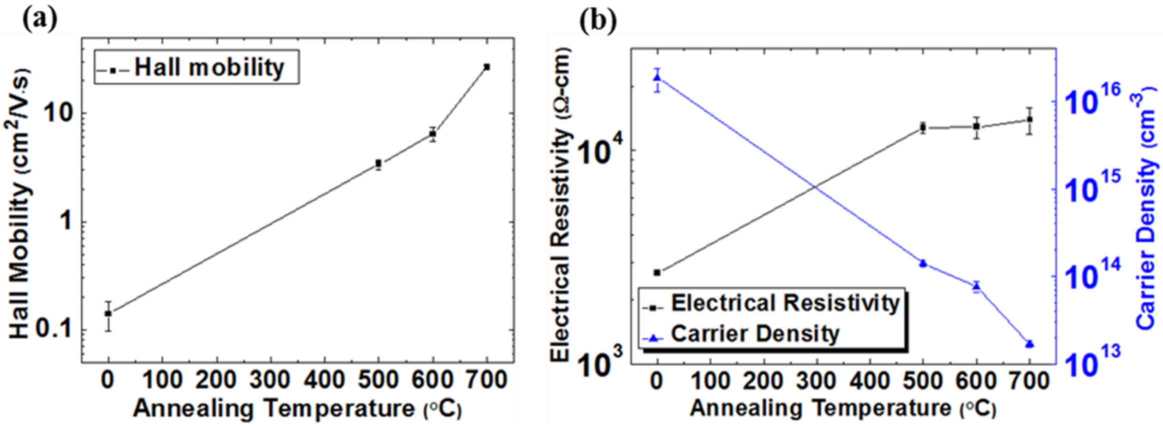

Figure 5.8. (a) Hall mobility and (b) electrical resistivity and carrier density of Cu_2O films as a function of annealing temperature [125].

1.4×10^4 Ω·cm. The reduction in carrier density suggests a decrease in copper vacancies, which is the main origin of holes in Cu_2O. In section 5.6, the annealing effect on the copper vacancy density will be quantitatively examined. The changes in μ_{Hall}, carrier density (i.e. free hole concentration, p_{free}) and E_u according to annealing temperature (T_A) are summarised in Table 5.1.

Table 5.1. Summary of parameters (μ_{Hall}, p_{free} and E_u) for different annealing temperatures [67].

T_A [°C]	As-deposited	500	600	700
μ_{Hall} [cm²/V·s]	0.14	3.75	7.42	28
p_{free} [cm⁻³]	1.68×10^{16}	1.30×10^{14}	7.34×10^{13}	1.85×10^{13}
E_u [meV]	223	166	128	78

5.4 Interpretation of Hall mobility enhancement

5.4.1 Two main conduction mechanisms

The carrier transport in nanocrystalline materials such as Cu_2O is mainly governed by two conduction mechanisms: grain-boundary-limited conduction related to the potential barrier at the grain boundary and trap-limited conduction associated with localised band tail states, as described in section 2.4. To be more specific, Cu_2O thin films have a nanocrystalline structure, which suggests the presence of potential energy barriers at grain boundaries as seen in Figure 5.9. This impedes hole transport in Cu_2O films [61, 131]. Furthermore, if

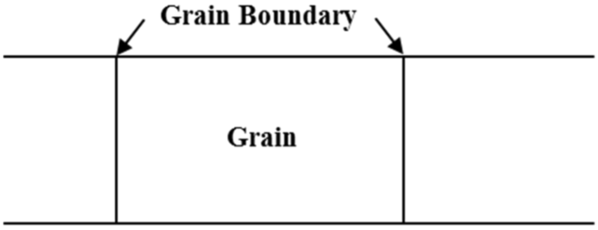

(a) Crystalline Structure

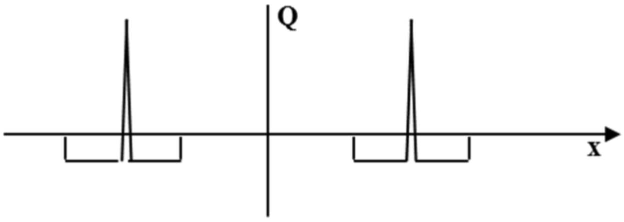

(b) Charge Distribution

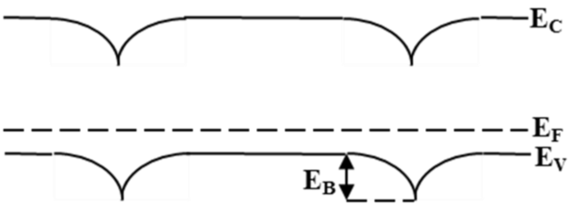

(c) Energy Band Structure

Figure 5.9. (a) The schematic crystal structure; (b) the charge distribution of a depletion region within grains and at grain boundaries; (c) the energy band diagram of Cu_2O films.

the band tail width in nanocrystalline materials is larger than the thermal energy, kT, a large portion of thermally excited carriers are trapped at the band tail states [132], and the carrier transport is significantly degraded by multiple carrier trapping and thermal release at the tail states (i.e. trap-limited conduction) [65, 66]. Since Cu_2O thin films have a much larger valence band tail width than the thermal energy based on the highly disordered nature of the VBM in Cu_2O (see subsection 5.3.2) and the extracted E_u (see Table 5.1), trap-limited conduction can also significantly degrade a hole mobility in Cu_2O films [123]. For this reason, in this section, the main causes of the carrier mobility enhancement by annealing are discussed in terms of the two conduction mechanisms.

5.4.2 The density of tail states and trapped hole concentration

First of all, in order to explain the μ_{Hall} improvement with an increase in T_A from the trap-limited conduction perspective, a change in the density of tail states at the valence band ($N_{VBtail}(E)$) was examined. $N_{VBtail}(E)$ can be approximated as an exponential distribution using O'Leary's empirical model for the distribution of electronic states of disordered semiconductors as follows [133],

$$N_{VBtail}(E) = N_{tv}\exp\left(\frac{E_V - E}{E_u}\right), \tag{5.3}$$

$$N_{tv} = \frac{\sqrt{2}{m_h^*}^{3/2}}{\pi^2 h^3}\sqrt{\frac{E_u}{2}}\exp\left(-\frac{1}{2}\right). \tag{5.4}$$

Here, E_V, N_{tv}, E_u and m_h^* denote the energy of the valence band edge, the tail state density at $E = E_V$, the Urbach energy reflecting the width of the valence band tail and the density-of-states effective mass of holes in the valence band, respectively. The majority of holes are produced from the light hole band since the band is situated at the top of the valence band (see subsection 2.3.3). Therefore, m_h^* can be regarded as the band mass of light holes (m_{lh}), which is about $0.56m_0$ [55], where m_0 is the electron rest mass. Using this value, the extracted E_u and Equations (5.3) and (5.4), $N_{VBtail}(E)$ and N_{tv} were estimated as shown in Figure 5.10.

As for the carrier density trapped at the tail states (n_{trap}), it was demonstrated that n_{trap} has an exponential dependence on kT rather than kT_t in the case of the tail state energy $kT_t < kT$ (T_t is the characteristic temperature of the tail states) and an exponential dependence on kT_t in the case of $kT_t > kT$ as seen in Table 5.2 [66]. In the p-type case (i.e. the majority carrier is a hole), the hole concentration trapped at the tail states (p_{trap}) can

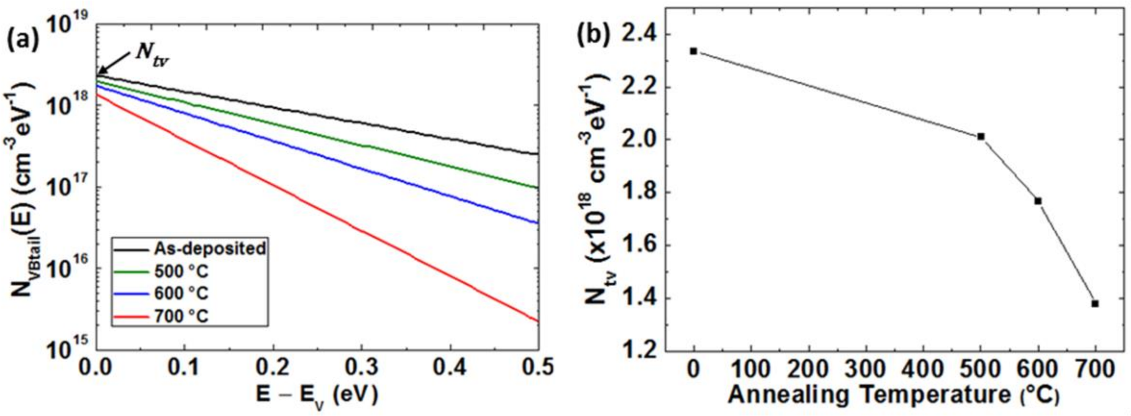

Figure 5.10. The extracted density of (a) tail states at the valence band ($N_{VBtail}(E)$) and (b) tail states at $E = E_V$ (N_{tv}) in Cu$_2$O thin films as a function of annealing temperature [67].

Table 5.2. The carrier concentration trapped at the tail states (n_{trap}) according to the conditions ($kT_t < kT$ and $kT_t > kT$). Here, E_C and N_{tc} denote the energy of the conduction band edge and the tail state density at $E = E_C$, and this is the n-type case (i.e. the majority carrier is an electron) [66].

Conditions	$kT_t < kT$	$kT_t > kT$
Trapped carrier concentration	$n_{trap} \approx \frac{1}{2} N_{tc} kT_t \left(\frac{2(E_C - E_F)}{kT_t}\right)^{kT_t/kT} \exp\left(\frac{E_F - E_C}{kT}\right)$	$n_{trap} \approx N_{tc} kT_t \exp\left(\frac{E_F - E_C}{kT_t}\right)$

be estimated by integrating Equation (5.3) weighted by the Fermi-Dirac distribution function (i.e. the probability of occupation of the donor-like tail states by an electron), $F(E) = 1/[1 + \exp\{(E - E_F)/kT\}]$ where E_F is the Fermi energy, as follows,

$$p_{trap} \approx \int_{E_V}^{\infty} N_{VBtail}(E)[1 - F(E)]dE. \tag{5.5}$$

Here, it is assumed that all ionised donor-like tail states filled with a hole (i.e. p_{trap}) are located above E_F (i.e. $F(E) = 0$ at $E > E_F$, $F(E) = 1$ at $E < E_F$), corresponding to the condition $kT_t \cong E_u > kT$ (see Table 5.1) [65, 134]. This yields an analytical expression for p_{trap} as

$$p_{trap} \approx N_{tv}E_u \exp\left(\frac{E_V - E_F}{E_u}\right). \tag{5.6}$$

$E_V - E_F$ can be estimated using the measured p_{free} (see Table 5.1) and its formula given by the Boltzmann approximation [135],

$$p_{free} = N_V \exp\left(\frac{E_V - E_F}{kT}\right). \tag{5.7}$$

Here, N_V denotes the effective density of states for free carriers in the valence band and is given by [135]

$$N_V \equiv 2\left(\frac{2\pi m_h^* kT}{h^2}\right)^{3/2}. \tag{5.8}$$

Using the calculated N_V (1.05×10^{19} cm^{-3} for $m_h^* = 0.56m_0$) and Equation (5.7), $E_V - E_F$ was obtained: −0.166 eV (as-deposited), −0.29 eV (500 °C), −0.31 eV (600 °C) and −0.34 eV (700 °C). Finally, p_{trap} was analytically estimated using the extracted parameters (N_{tv}, E_u and $E_V - E_F$) and Equation (5.6) as seen in Figure 5.11. This shows a reduction in p_{trap} with an increase in T_A, which quantitatively demonstrates that the μ_{Hall} enhancement

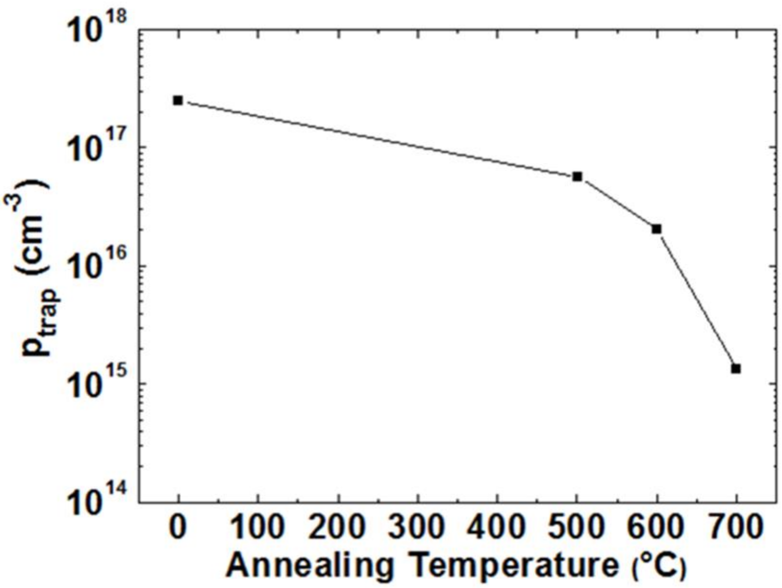

Figure 5.11. Extracted trapped hole concentration (p_{trap}) as a function of annealing temperature.

is due to a reduction in hole trapping events resulting from a decrease in valence band tail states.

5.4.3 Scanning electron microscopy images

In this subsection, in order to provide an interpretation of the μ_{Hall} enhancement from the grain-boundary-limited conduction point of view, a change in the grain size was examined using scanning electron microscopy. Figure 5.12 shows that an increase in T_A leads to an increase in the grain size (i.e. a reduction in the number of grain boundaries), which can also result in the μ_{Hall} enhancement. The changes in the grain size and energy barrier height at grain boundaries will be quantitatively discussed in subsection 5.5.4.

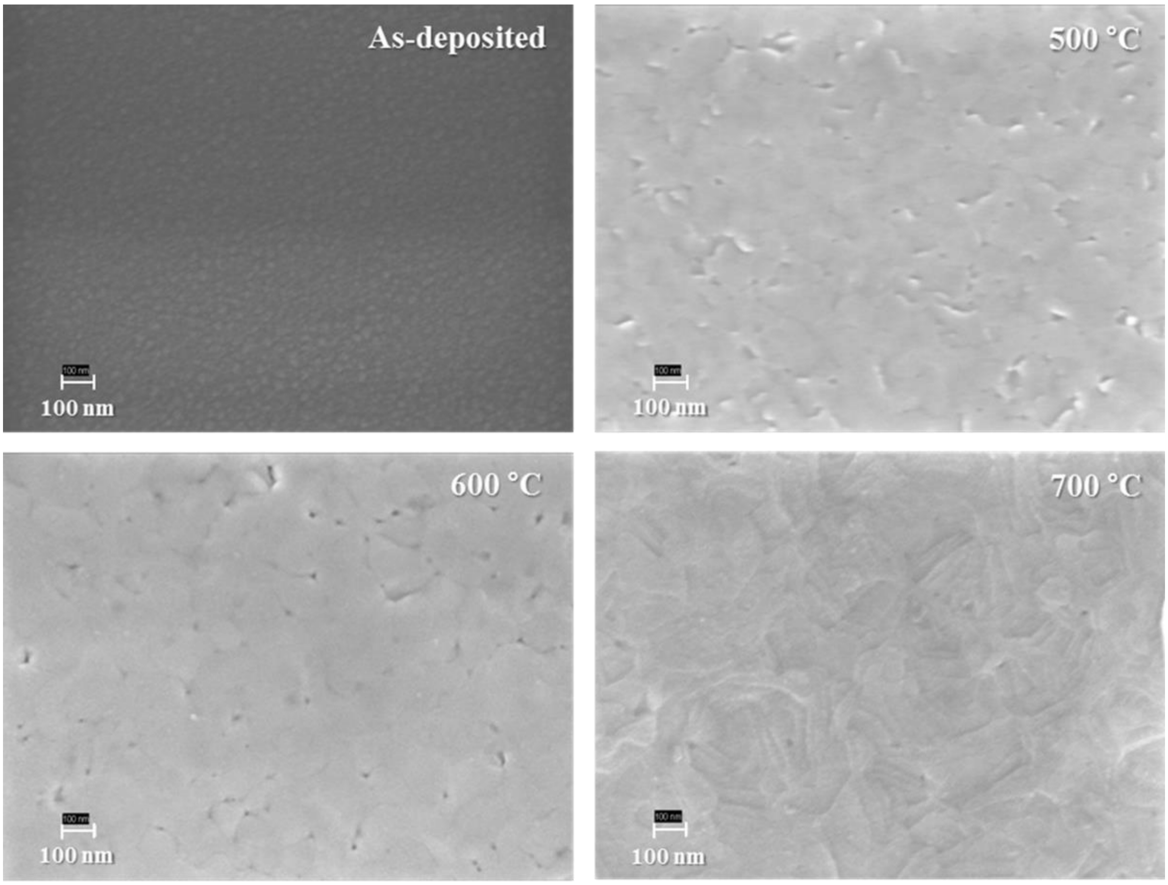

Figure 5.12. SEM images of Cu_2O film surfaces before and after annealing at 500, 600 and 700 ℃ [67].

5.5 Relative dominance of conduction mechanisms

For an in-depth discussion on the main causes of the very low μ_{Hall} of the as-deposited Cu_2O as well as the μ_{Hall} enhancement by annealing, a quantitative and analytical study on the relative dominance of trap-limited conduction (TLC) and grain-boundary-limited conduction (GLC) is presented in this section.

5.5.1 Hall mobility definition

If there are several mobility degradation mechanisms and they are mutually independent, then the effect of the individual degradation mechanisms on the measured carrier mobility can be easily visualised using Matthiessen's rule as follows,

$$\mu^{-1} = \sum_i \mu_i^{-1}, \tag{5.9}$$

where μ_i is a mobility limited by an individual degradation mechanism. Using this rule, the effects of TLC and GLC can be incorporated into μ_{Hall} as

$$\frac{1}{\mu_{Hall}} = \frac{1}{\mu_0} + \frac{1}{\mu_{TLC}} + \frac{1}{\mu_{GLC}} = \frac{1}{\mu_{0,TLC}} + \frac{1}{\mu_{GLC}}, \tag{5.10}$$

$$\frac{1}{\mu_0} = \frac{1}{\mu_{ph}} + \frac{1}{\mu_{ii}} + \cdots, \tag{5.11}$$

where μ_0 is the free carrier mobility determined by several intrinsic scattering mechanisms such as phonon (lattice) scattering (μ_{ph}) and ionised impurity scattering (μ_{ii}), and μ_{TLC} and μ_{GLC} denote the mobilities limited by TLC and GLC, respectively. Here, $\mu_0^{-1} + \mu_{TLC}^{-1}$ can be expressed as $\mu_{0,TLC}^{-1}$ (i.e. $\mu_0^{-1} + \mu_{TLC}^{-1} = \mu_{0,TLC}^{-1}$, where $\mu_{0,TLC}$ denotes the effective carrier mobility degraded by TLC). Using trap-limited conduction theory, $\mu_{0,TLC}$ is given by μ_0 weighted by β_{TLC} which is the ratio of p_{free} to the total carrier concentration (i.e. $p_{free} + p_{trap}$) as follows [63, 132],

$$\mu_{0,TLC} = \mu_0 \beta_{TLC}, \tag{5.12}$$

$$\beta_{TLC} = \left(\frac{p_{free}}{p_{free} + p_{trap}} \right). \tag{5.13}$$

Using Equations (5.10) and (5.12), μ_{Hall} is then given by

$$\mu_{Hall} = \frac{\mu_0 \beta_{TLC} \mu_{GLC}}{\mu_0 \beta_{TLC} + \mu_{GLC}} = \mu_0 \alpha_{GLC} \beta_{TLC}, \tag{5.14}$$

$$\alpha_{GLC} = \frac{\mu_{GLC}}{\mu_0 \beta_{TLC} + \mu_{GLC}}, \tag{5.15}$$

where α_{GLC} $(0 < \alpha_{GLC} \leq 1)$ denotes the GLC coefficient quantifying the effect of GLC on μ_{Hall}. Here, $\alpha_{GLC} = 1$ (i.e. $\mu_{GLC} \gg \mu_0 \beta_{TLC}$) represents the condition when μ_{Hall} is affected by only TLC.

5.5.2 Analytical calculation of mobility parameters

GLC coefficient (α_{GLC})

The GLC effect on μ_{Hall} was first quantified by extraction of α_{GLC}. The α_{GLC} can be determined based on the difference between $p_{trap(Hall)}$ (p_{trap} calculated from measured μ_{Hall} including the effects of TLC and GLC) and $p_{trap(DOS)}$ (p_{trap} calculated from the extracted $N_{VBtail}(E)$ including only the TLC effect). To be specific, using Equations (5.13) and (5.14), p_{trap} is given by

$$p_{trap} = p_{free} \left(\frac{\alpha_{GLC} \mu_0}{\mu_{Hall}} - 1 \right). \tag{5.16}$$

If α_{GLC} is not deliberately considered in Equation (5.16), $p_{trap(Hall)}$ can be analytically obtained from

$$p_{trap(Hall)} = p_{free}\left(\frac{\mu_0}{\mu_{Hall}} - 1\right). \tag{5.17}$$

If there is the GLC effect on μ_{Hall}, then the calculated $p_{trap(Hall)}$ is overestimated since α_{GLC} $(0 < \alpha_{GLC} < 1)$. This is reflected in the degradation of μ_0 by GLC, and is not considered in Equation (5.17). This leads to the discrepancy between $p_{trap(Hall)}$ and $p_{trap(DOS)}$. Including the $p_{trap(Hall)}$ and $p_{trap(DOS)}$ in Equation (5.16) allowing for α_{GLC} as follows,

$$\begin{aligned} p_{trap(DOS)} &= p_{free}\left[\left(\frac{\alpha_{GLC}\mu_0}{\mu_{Hall}} - 1\right) + \frac{\mu_0}{\mu_{Hall}} - \frac{\mu_0}{\mu_{Hall}}\right] \\ &= p_{free}\left[\left(\frac{\mu_0}{\mu_{Hall}} - 1\right) - \frac{\mu_0}{\mu_{Hall}}(1 - \alpha_{GLC})\right] \\ &= p_{trap(Hall)} - \frac{p_{free}\mu_0}{\mu_{Hall}}(1 - \alpha_{GLC}), \end{aligned} \tag{5.18}$$

means that α_{GLC} can then be estimated by

$$\alpha_{GLC} = 1 - \frac{\mu_{Hall}}{\mu_0}\left(\frac{p_{trap(Hall)} - p_{trap(DOS)}}{p_{free}}\right). \tag{5.19}$$

Here, μ_0 is assumed to be 270 $\text{cm}^2/\text{V}\cdot\text{s}$ (the theoretical mobility limit by longitudinal-optical (LO) phonon scattering at room temperature) since phonon scattering is dominant above 200 K [55, 60]. In addition, α_{GLC} for T_A = 700 °C is assumed to be $\alpha_{GLC} = 1$ (i.e. $p_{trap(Hall)}$(700 °C) = $p_{trap(DOS)}$(700 °C)) based on the fact that a Cu_2O TFT annealed at 700 °C obeys the Meyer-Neldel (MN) rule indicating that carrier transport is governed by trap-limited conduction [123, 136, 137]. Specifically, Figure 5.13 shows an exponential relation between the prefactor ($|I_{D0}|$) and activation energy (E_a) extracted from $I_{DS} = I_{D0}\exp(-E_a/kT)$, where I_{DS} is a measured drain-source current of a Cu_2O TFT annealed at 700 °C, which follows the Meyer-Neldel (MN) rule. It has been demonstrated that trap-

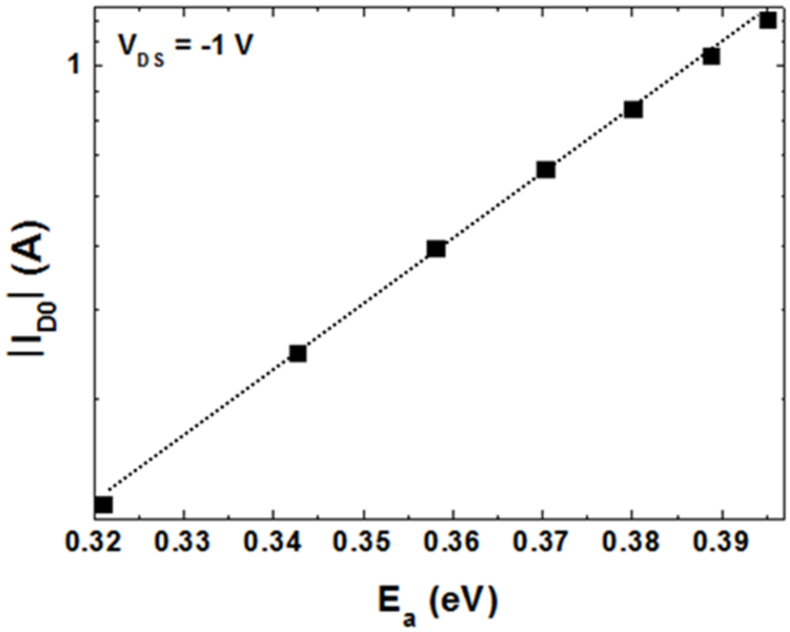

Figure 5.13. Prefactor ($|I_{D0}|$) (log scale) versus activation energy (E_a) for the Cu_2O TFT annealed at 700 °C.

limited conduction always exhibits the MN rule [136], which allows the assumption of α_{GLC} = 1 for T_A = 700 °C (i.e. carrier transport is governed by only TLC). In order to determine the extent of the discrepancy between $p_{trap(Hall)}$ and $p_{trap(DOS)}$ (i.e. $p_{trap(Hall)} - p_{trap(DOS)}$), p_{trap} calculated from the extracted $N_{VBtail}(E)$ (see Figure 5.11) was corrected by the product of p_{trap} (normalised to the value at T_A = 700 °C) and $p_{trap(Hall)}$(700 °C) (see $p_{trap(DOS)}$ in Figure 5.14 (a)). Figure 5.14 (a) shows a large discrepancy between $p_{trap(Hall)}$ and $p_{trap(DOS)}$ for the as-deposited Cu_2O thin film; the discrepancy decreases significantly after annealing at $T_A \geq 500$ °C. Using Equation (5.19) and the difference between $p_{trap(Hall)}$ and $p_{trap(DOS)}$, α_{GLC} was finally estimated as seen in Figure 5.14 (b). This shows that a very low α_{GLC} (significant grain-boundary-limited conduction) of the as-deposited Cu_2O film increases considerably after annealing at 500 °C and α_{GLC} approaches unity (no grain-boundary-limited conduction) as T_A increases further: 0.0014 (as- deposited), 0.76 (500 °C), 0.96 (600 °C), 1 (700 °C). This suggests that while

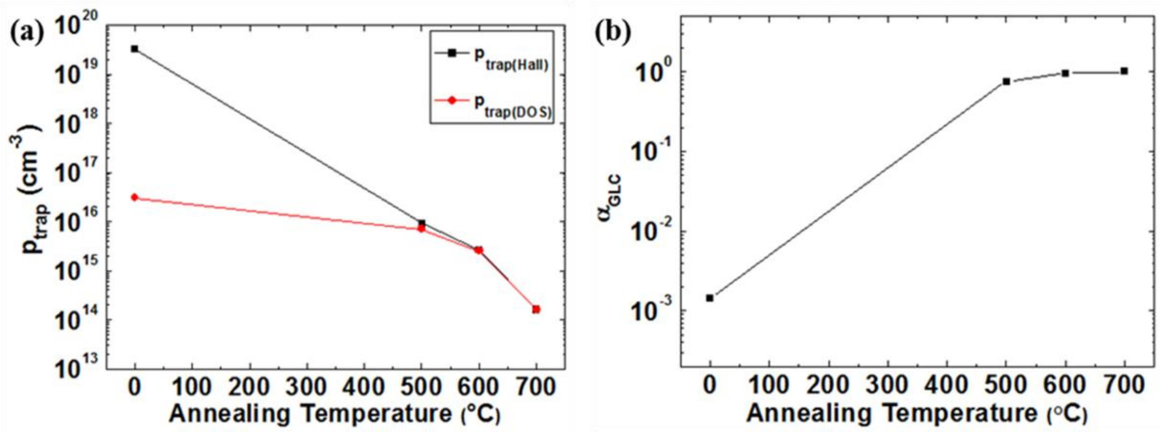

Figure 5.14. (a) $p_{trap(Hall)}$ and $p_{trap(DOS)}$ and (b) α_{GLC}, estimated from the extent of the discrepancy between $p_{trap(Hall)}$ and $p_{trap(DOS)}$, as a function of annealing temperature [67].

GLC has a significant effect on carrier transport in the as-deposited thin film, the GLC effect on carrier transport becomes insignificant after high-temperature annealing.

Extraction of $\mu_{0,GLC}$ and μ_{TLC}

The relative dominance of TLC and GLC was quantitatively investigated by extraction of $\mu_{0,GLC}$ (the effective carrier mobility degraded by GLC) and μ_{TLC}. Using Equations (5.14) and (5.15), μ_{GLC} is first given by

$$\mu_{GLC} = \frac{\mu_0 \alpha_{GLC} \beta_{TLC}}{1 - \alpha_{GLC}} = \frac{\mu_{Hall}}{1 - \alpha_{GLC}}. \tag{5.20}$$

The assumption ($\alpha_{GLC} = 1$ for T_A = 700 °C, i.e. GLC has no effect on μ_{Hall}) results in $\mu_{GLC} = \infty$, which physically means the relative insignificance of GLC compared to TLC (i.e. $\mu_{GLC} \gg \mu_{TLC}$), not actually infinite μ_{GLC}. For this reason, in order to provide a quantitative comparison with μ_{TLC}, $\mu_{0,GLC}$ was calculated using the following equation derived from $\mu_{0,GLC}^{-1} = \mu_0^{-1} + \mu_{GLC}^{-1}$ and Equation (5.20),

$$\mu_{0,GLC} = \frac{\mu_0 \mu_{Hall}}{\mu_0 (1 - \alpha_{GLC}) \mu_{Hall}}. \tag{5.21}$$

Using Matthiessen's rule (i.e. $\mu_{Hall}^{-1} = \mu_0^{-1} + \mu_{GLC}^{-1} + \mu_{TLC}^{-1} = \mu_{0,GLC}^{-1} + \mu_{TLC}^{-1}$), μ_{TLC} is given by

$$\mu_{TLC} = \frac{\mu_{0,GLC} \mu_{Hall}}{\mu_{0,GLC} - \mu_{Hall}}. \tag{5.22}$$

The calculated results along with measured μ_{Hall} (see Figure 5.15) show that μ_{Hall} is entirely determined by $\mu_{0,GLC}$ for the as-deposited film, while μ_{Hall} is limited by μ_{TLC} after annealing at $T_A \geq 500$ ℃. This means that carrier transport in the as-deposited film is governed by GLC, whereas GLC becomes insignificant and TLC dominates after high-temperature annealing, suggesting that the very low as-deposited μ_{Hall} results from the significant GLC, and the μ_{Hall} improvement by annealing is determined by TLC.

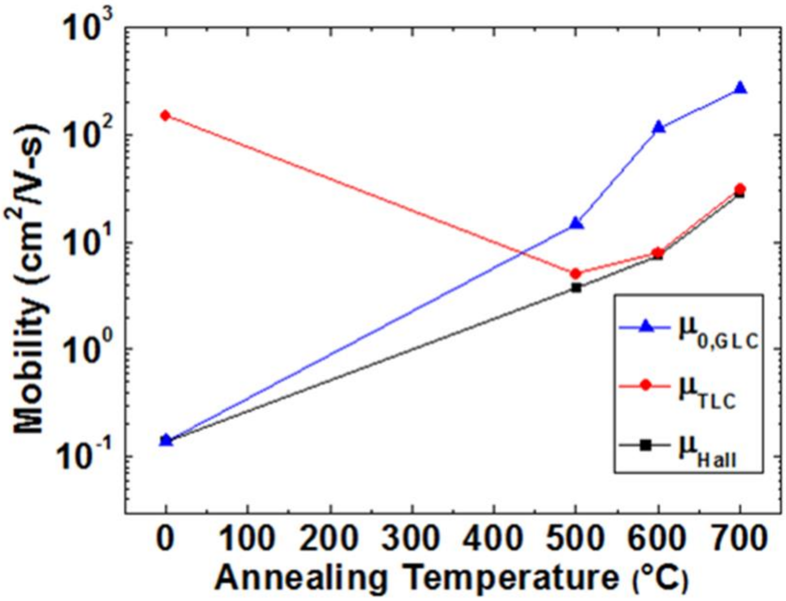

Figure 5.15. Measured μ_{Hall}, extracted μ_{TLC} and $\mu_{0,GLC}$ as a function of annealing temperature [67].

5.5.3 Grain size and energy barrier height at grain boundaries

In this subsection, in order to explain the significant reduction in the GLC effect by annealing, changes in the grain size (L_g) and the potential energy barrier height (E_B) at grain boundaries were quantitatively investigated. Using the line broadening of the intense Cu_2O (200) peak of the XRD patterns (see Figure 5.2), L_g can be estimated by the Scherrer equation (Equation 3.2). $\mu_{0,GLC}$ is given by $\mu_{0,GLC} = L_g q\sqrt{1/2\pi m^* kT}\exp(-E_B/kT)$, where q denotes the elementary charge [61]. Using this equation, the E_B is given as

$$E_B = -kT\ln\left(\frac{\mu_{0,GLC}\sqrt{2\pi m^* kT}}{L_g q}\right). \tag{5.23}$$

L_g and E_B were extracted using Equations (3.2) and (5.23), respectively, as seen in Figure 5.16. This quantitatively shows an increase in L_g and a reduction in E_B with an increase in T_A, providing a clear explanation for the decrease in the GLC effect. In addition, E_B is

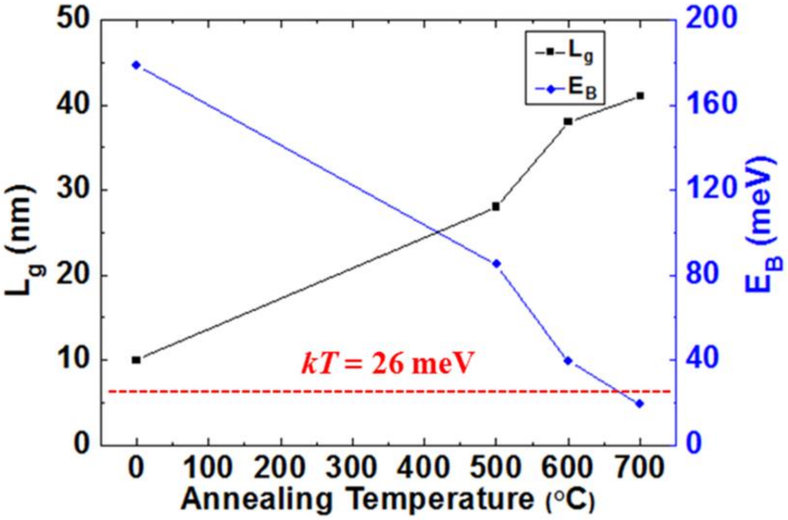

Figure 5.16. The estimated grain size (L_g) and potential barrier height (E_B) as a function of annealing temperature. Here, the red dot line shows the thermal energy kT at room temperature [67].

reduced to $E_B < kT$ (~26 meV) at T_A = 700 °C, which is considered to be the main reason for the insignificance of the GLC effect in the Cu$_2$O film annealed at 700 °C.

5.5.4 Fermi energy effect on trap-limited conduction

Although the as-deposited thin film has the largest E_u, it exhibits the highest μ_{TLC} (i.e. a relatively insignificant TLC effect in the as-deposited film) as seen in Figure 5.15. This can be explained by the E_F effect on TLC. Figure 5.17 (a) shows calculated values for p_{free}, $p_{trap} = p_{trap(DOS)}$, $p_{total} = p_{free} + p_{trap}$ and β_{TLC} (i.e. the ratio of p_{free} to $p_{free} + p_{trap}$) of the as-deposited Cu$_2$O film with E_u = 223 meV as a function of $E_F - E_V$. This shows that since the gradient of p_{free} is higher than that of p_{trap} (i.e. $(kT)^{-1} > (E_u)^{-1}$), β_{TLC} approaches unity with a decrease in $E_F - E_V$. Based on trap-limited

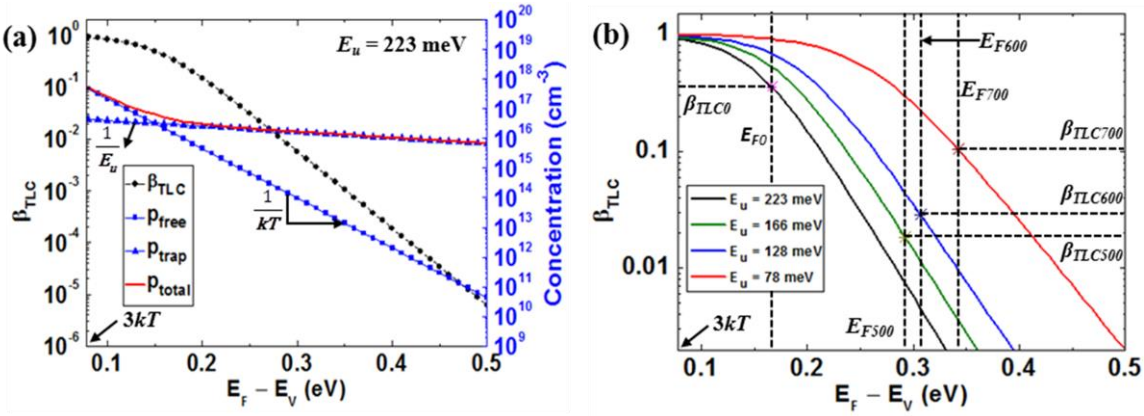

Figure 5.17. (a) calculated p_{free}, p_{trap}, p_{total} and β_{TLC} of as-deposited Cu$_2$O with E_u = 223 meV and **(b)** β_{TLC} of all the samples with E_u = 223 meV (as-deposited), 166 meV (500 °C), 128 meV (600 °C), 78 meV (700 °C) as a function of $E_F - E_V$. In (a), p_{free} was estimated using Equation (5.7) given by the Boltzmann approximation which is valid for $E_F - E_V \geq 3kT$. In (b), E_{F0}, E_{F500}, E_{F600} and E_{F700} denote the Fermi energy before and after annealing at 500, 600 and 700 °C, and the corresponding β_{TLC} values are $\beta_{TLC0} = 0.36$, $\beta_{TLC500} = 0.018$, $\beta_{TLC600} = 0.029$ and $\beta_{TLC700} = 0.1$, respectively [67].

conduction theory (see Equation (5.12)), this means that the TLC effect decreases as E_F approaches to E_V. This suggests that not only E_u but also the position of E_F have an effect on μ_{TLC}. In order to help understanding of this, Figure 5.17 (b) shows the calculated β_{TLC} values of all the samples with E_u = 223 meV (as-deposited), 166 meV (500 °C), 128 meV (600 °C) and 78 meV (700 °C) as a function of $E_F - E_V$. If E_F of all the samples lay at the same energy, as-deposited Cu_2O with the largest E_u would have the lowest β_{TLC} value (i.e. the most significant TLC effect). However, since the as-deposited film has a much smaller $(E_F - E_V)$ value than those of annealed films, it has the highest β_{TLC} value as seen in Figure 5.17 (b). This is the reason for the relative insignificance of the TLC effect (i.e. high μ_{TLC}) in the as-deposited Cu_2O film.

5.6 The density of copper vacancies

Figures 5.8 (b) and 5.13 (a) show a decrease in the total hole concentration ($p_{total} = p_{free} + p_{trap}$) with an increase in T_A. This suggests that an increase in T_A leads to a reduction in copper vacancies (V_{Cu}) which are the main origin of holes in Cu_2O [9, 124]. In this section, a simple method for extracting the density of copper vacancies ($N_{V_{Cu}}$) is proposed in order to provide a quantitative insight into the decrease in V_{Cu}. This model begins with the charge neutrality condition (i.e. $p + N_D^+ = n + N_A^-$) [135]. Here, p and n denote free hole and free electron concentrations, and N_D^+ and N_A^- are the densities of ionised donors and ionised acceptors, respectively. Since there is a broad distribution of localised tail states at the valence band (i.e. donor-like states) in Cu_2O films and holes are trapped at the tail states, this charge neutrality condition should include the density of ionised tail states (N_{TS}^+), $p + N_D^+ + N_{TS}^+ = n + N_A^-$. Considering that N_D^+ and n are negligible (i.e. $p + N_{TS}^+ \gg N_D^+$, $N_A^- \gg n$) [135], this condition becomes $p + N_{TS}^+ \approx N_A^-$. Additionally, contrary to the shallow V_{Cu} acceptor level, oxygen interstitials (O_i) are another possible hole producer and have deep acceptor levels [9]. For this reason, it can be assumed that the majority of holes are produced by V_{Cu}, and therefore the density of ionized copper vacancies ($N_{V_{Cu}}^{-}$) can be substituted for N_A^-. Substituting p_{trap} for N_{TS}^{+}, the final form of the charge neutrality condition is obtained as follows,

$$N_{V_{Cu}}^{-} \approx p_{free} + p_{trap}. \tag{5.24}$$

Using the formula for the ionised acceptor concentration [135], $N_{V_{Cu}}^{-}$ could be given by

$$N_{V_{Cu}}^{-} = \frac{N_{V_{Cu}}}{1 + g_A \exp\left(\frac{E_{V_{Cu}} - E_F}{kT}\right)}, \tag{5.25}$$

where g_A and $E_{V_{Cu}}$ denote the acceptor-site degeneracy factor and the energy level of copper vacancies, respectively. Here, representing $E_{V_{Cu}} - E_F$ as $\left(E_{V_{Cu}} - E_V\right) + (E_V - E_F)$, Equation (5.25) can be written as

$$N_{V_{Cu}}^{-} = \frac{N_{V_{Cu}}}{1 + g_A \exp\left(\frac{E_{V_{Cu}} - E_V}{kT}\right) \exp\left(\frac{E_V - E_F}{kT}\right)}. \tag{5.26}$$

Using Equations (5.7), (5.24) and (5.26), $N_{V_{Cu}}$ is finally given by

$$N_{V_{Cu}} = \left(p_{free} + p_{trap}\right) \left[1 + g_A \exp\left(\frac{E_{V_{Cu}} - E_V}{kT}\right) \frac{p_{free}}{N_V}\right]. \tag{5.27}$$

Here, $E_{V_{Cu}} - E_V = 0.28$ eV is used; this has been calculated by DFT [9]. Since the valence band ($\Gamma_{25'}$) of Cu$_2$O is split into an upper band (Γ_7^+) and a lower band (Γ_8^+) by spin-orbit interaction (see subsection 2.3.3) [55], Cu$_2$O has one degenerate valence band (i.e. Γ_7^+) at the VBM. This means that each copper vacancy state (i.e. each acceptor state) can accept one hole with either spin or can have no hole [135], and thus $g_A = 2$. Using these parameters and Equation (5.27) along with the measured p_{free} and extracted $p_{trap(DOS)}$ for p_{trap}, $N_{V_{Cu}}$ was analytically estimated as shown in Figure 5.18. This quantitatively shows that an increase in T_A gives rise to a significant decrease in V_{Cu}.

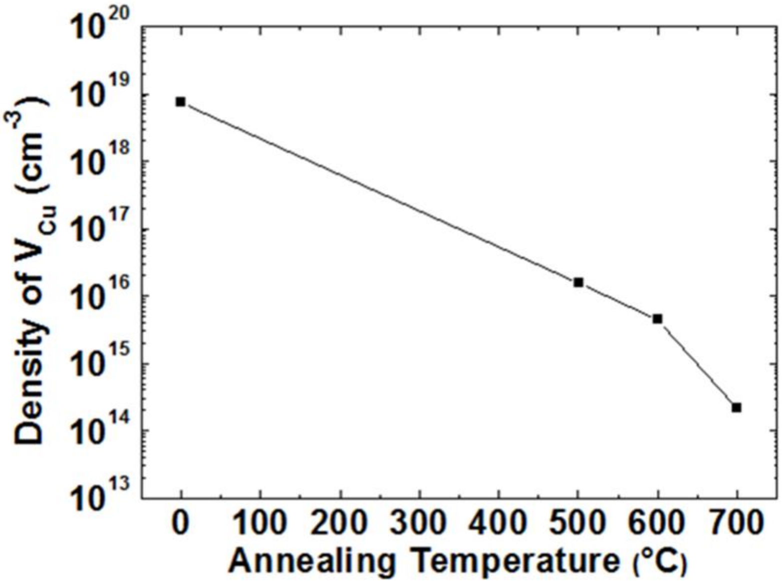

Figure 5.18. The extracted density of copper vacancies as a function of annealing temperature [67].

5.7 Conclusions

In this chapter, it was demonstrated that Cu_2O thin films can be annealed in vacuum without any phase conversion, such as oxidation (CuO) or oxide reduction (Cu). Using vacuum annealing, annealing effects on Cu_2O films were investigated based on the crystallographic, optical and electrical characteristics. This shows that an increase in annealing temperature leads to (1) an enhancement of film crystallinity, (2) widening of the optical band gap, (3) a significant improvement in carrier mobility and (4) a considerable reduction in carrier density. The widening of the optical band gap is explained by a reduction in the band tail based on the extracted Urbach energy.

In order to provide insights into the very low carrier mobility in as-deposited Cu_2O and the mobility enhancement by thermal annealing, a quantitative analysis of the relative dominance of the main conduction mechanisms (i.e. grain-boundary-limited and trap-limited conduction) in Cu_2O films was performed based on the analytical calculation using

Matthiessen's rule and the difference between $p_{trap(Hall)}$ and $p_{trap(DOS)}$. This shows that GLC is a dominant mobility degradation mechanism in as-deposited thin films, whereas after annealing at $T_A \geq 500$ °C, GLC becomes insignificant due to a significant decrease in the potential barrier height at grain boundaries, and thus carrier transport in annealed thin films is governed by TLC. This suggests that the significant GLC leads to the very low carrier mobility in as-deposited Cu_2O films, and the mobility improvement by annealing is due to a considerable reduction in the GLC effect. However, the carrier mobility in annealed Cu_2O films is still limited by TLC, which also suggests that research for a further improvement in the carrier mobility should focus on a reduction in localised tail states leading to TLC. In particular, the analysis method proposed here can be widely used for identifying the dominant conduction mechanism in nanocrystalline materials with a high density of localised tail states (i.e. $kT_t > kT$).

Lastly, an increase in annealing temperature leads to a reduction in the total hole concentration (i.e. $p_{free} + p_{trap}$), which suggests a decrease in copper vacancies in Cu_2O thin films. This was quantitatively confirmed by the analytical calculation using the charge neutrality condition, allowing for ionised valence band tail states, and the formula for the ionised acceptor concentration.

Chapter 6

Control of grain orientation and its impact on carrier mobility

6.1 Introduction

Most of the existing literature on control of the Cu_2O grain orientation is based on the electrodeposition technique and it was demonstrated that the film growth orientation is controllable by its several deposition parameters (e.g. electrolyte pH and potential applied to the electrode) [138–142]. However, the conductive substrate that is required for electrodeposition leads to difficulty in accurately measuring electrical characteristics of a Cu_2O film itself, which hinders a systematic study on the effect of the grain orientation on the carrier mobility in Cu_2O thin films. This problem can be easily solved through control of the grain orientation by reactive sputtering allowing the use of an insulating substrate such as glass.

This chapter shows that using reactive sputtering, the grain orientation in Cu_2O thin films can be controlled in the direction of either [111] or [100] normal to the surface by adjusting the ion-to-metal flux ratio incident at the growing film surface. This allows a systematic investigation to determine which grain orientation is more favourable for a p-type Cu_2O channel layer in terms of the carrier mobility. Conduction is not isotropic in polycrystalline Cu_2O thin films because grain boundaries impede in-plane carrier transport. This chapter focuses on the in-plane carrier mobility in Cu_2O thin films since this is the direction of current flow in TFTs. Furthermore, the grain orientation impact on the in-plane carrier mobility in annealed Cu_2O thin films will be discussed from the viewpoint of the Urbach energy, crystallinity and surface morphology.

6.2 Cu_2O (111) and (100) surfaces

The atomic structure and surface energy (E_S) of Cu_2O (111) and (100) are briefly discussed in this section. An ideal Cu_2O (111) surface has hexagonal symmetry. Single atomic layer does not consist of both copper cations and oxygen anions. Each copper plane

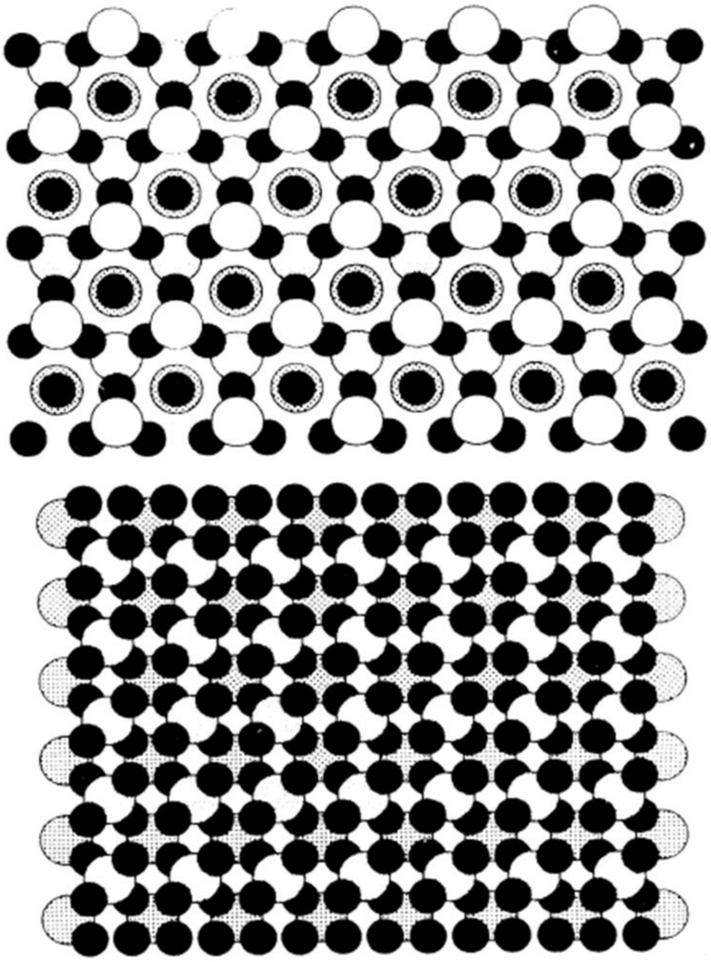

Figure 6.1. Ball-model illustrations of (a) the ideal nonpolar Cu_2O (111) surface and (b) the ideal polar Cu-terminated Cu_2O (100) surface. The large open circles show O^{2-} anions, whereas the small solid circles show Cu^+ ions. Image reproduced from [143].

is sandwiched between two oxygen planes. The copper plane has four Cu^+ cations per surface unit cell with a 4+ charge, whereas the oxygen plane contains one anion per unit cell with a 2- charge [143]. Therefore, the sum of the potential over the three-plane repeat unit is zero and so there is no dipole moment normal to the surface. This is classified as a Tasker class II surface which is nonpolar [144]. It has been demonstrated by DFT calculations that the nonpolar (111) surface has the lowest surface energy of 0.677 $J \cdot m^{-2}$ [145]. Figure 6.1(a) shows a ball-model illustration of the ideal, stoichiometric Cu_2O (111) surface.

The ideal Cu_2O (100) surface possesses square symmetry. As on the (111) surface, single atomic layer does not contain both copper cations and oxygen anions. The copper plane consists of two Cu^+ cations per unit cell with a total 2+ charge, while the oxygen plane has one anion per unit cell with a 2- charge. The structural arrangement alternates between the copper and oxygen planes [143], which produces a dipole moment perpendicular to the surface. This is classified as a Tasker class III surface which is polar [144]. The polar (100) surface has a higher surface energy of 1.194 $J \cdot m^{-2}$ [145]. Figure 6.1(b) shows a ball-model illustration of the ideal, stoichiometric Cu_2O (100) surface.

6.3 Control of grain orientation

Considering the surface energy, the preferred grain orientation of Cu_2O thin films is expected to be [111] since films generally tend to grow with the crystal plane of the lowest surface energy parallel to the substrate to minimise the surface energy [146].

In a recent report by Wang *et al.* [147], it was demonstrated that the preferred grain orientation in sputtered Cu_2O films can be controlled from the [111] direction to the [100] direction (which has the highest surface energy) by an increase in kinetic energy of adatoms through adjusting the process pressure. In addition to the process pressure, varying the ion-to-metal flux ratio (J_i/J_{me}) incident at the growing film during sputter deposition is known to be an effective method for controlling kinetic energy of adatoms [148, 149]. For instance, an increase in J_i/J_{me} means that more energetic ions collide with each metal adatom at the growing film surface, thereby leading to an increase in ion-adatom momentum transfer (i.e. higher kinetic energy of adatoms). For this reason, it is worth examining the effect of J_i/J_{Cu} on the grain orientation in Cu_2O thin films.

The HiTUS system used for Cu_2O deposition enables a precise control of J_i/J_{Cu} by simply adjusting the ion current i_c (a sputtering parameter related to an Ar plasma density at the surface of a Cu target). To be specific, the dominant sources of the ion flux (J_i) incident at the growing film are the ions generated by the Ar and O_2 plasma near to the grounded substrate holder. An increase in i_c means an increase in the Ar plasma density at the Cu target surface and this results in more Cu atoms coming out from the target (i.e. a higher Cu flux, J_{Cu}). On the other hand, the change in i_c has a negligible effect on the Ar plasma density near to the substrate and the O_2 plasma can remain constant by using the same oxygen flow rate, allowing the assumption of a constant J_i. As a result, an increase in i_c leads to a decrease in J_i/J_{Cu} (i.e. i_c is inversely related to J_i/J_{Cu}). Therefore, in order to investigate the J_i/J_{Cu} dependence on the Cu_2O grain orientation, i_c was varied from 1.38 to 1.52 ampere (A) under a constant process condition: process pressure of 1.5×10^{-3} mbar, target bias voltage of 690 V, oxygen flow rate of 16 sccm and no intentional substrate heating.

The XRD patterns of Cu_2O thin films deposited at different ion currents are shown in Figure 6.2. For $i_c \geq 1.5$ A (i.e. a lower J_i/J_{Cu}), the intense diffraction peak related to the (111) plane of Cu_2O is detected, while the (200) diffraction peak of Cu_2O is observed for $i_c < 1.5$ A (i.e. a higher J_i/J_{Cu}). The small peak close to 38° does not match any of the reference peaks of Cu_2O, CuO and Cu. The same peak is also observed in XRD patterns of Cu_2O films in reference [55], and the authors mentioned that the peak is due to the sample holder. Based on this, the small peak seems to be an experimental artefact caused by the sample holder. The result from Figure 6.2 clearly shows a change in the preferred grain orientation of Cu_2O thin films from [111] with low surface energy to [100] with high surface energy by an increase in J_i/J_{Cu}. Considering the fact that an increase in J_i/J_{Cu} leads to higher kinetic energy of adatoms, this result is consistent with Wang's result showing that the high surface energy configuration (i.e. [100] orientation) can be obtained

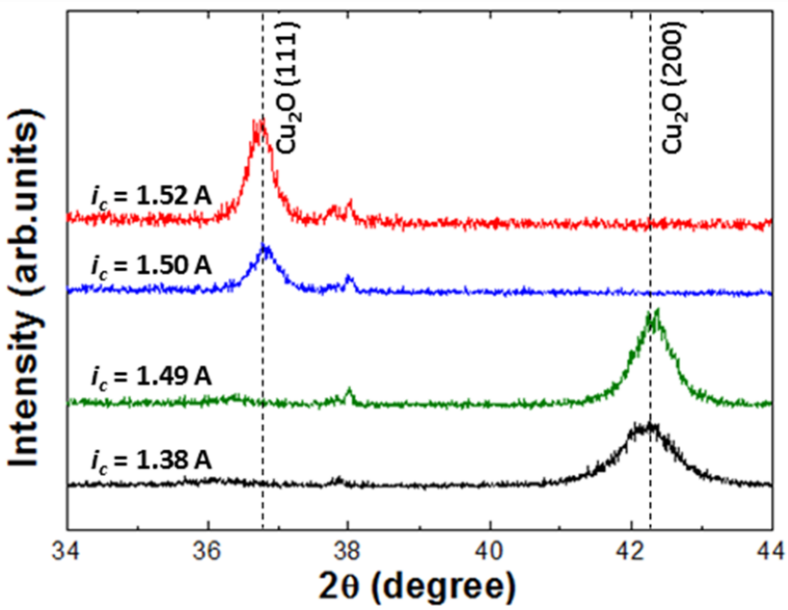

Figure 6.2. XRD patterns of as-deposited Cu_2O films formed at various ion currents.

by an increase in kinetic energy of adatoms [147]. Petrov *et al.* also showed that the preferred orientation in polycrystalline TaN films can be controlled by the ion-to-metal flux ratio (J_i/J_{Ta}) using a magnetron sputter deposition system [150]. Contrary to their result showing a gradual transition of grain orientation in TaN films from [111] to [111] + [001] and to complete [001] with an increase in J_i/J_{Ta} (see Figure 12 in reference [150]), Cu_2O films deposited by the HiTUS system show a sharp transition from [111] to [100] with an increase in J_i/J_{Cu} as seen in Figure 6.1.

6.4 Grain orientation effect on carrier mobility

In order to examine the effect of the grain orientation on the carrier mobility in Cu_2O films, the samples deposited at i_c = 1.38 A and i_c = 1.52 A were chosen as the [100] and [111]-oriented Cu_2O films, respectively, and the Hall mobility (μ_{Hall}) of their as-deposited and annealed films was measured. Here, the post-deposition annealing was performed at the same condition as in section 5.2 (i.e. base pressure of 9.5×10^{-4} mbar and annealing time of

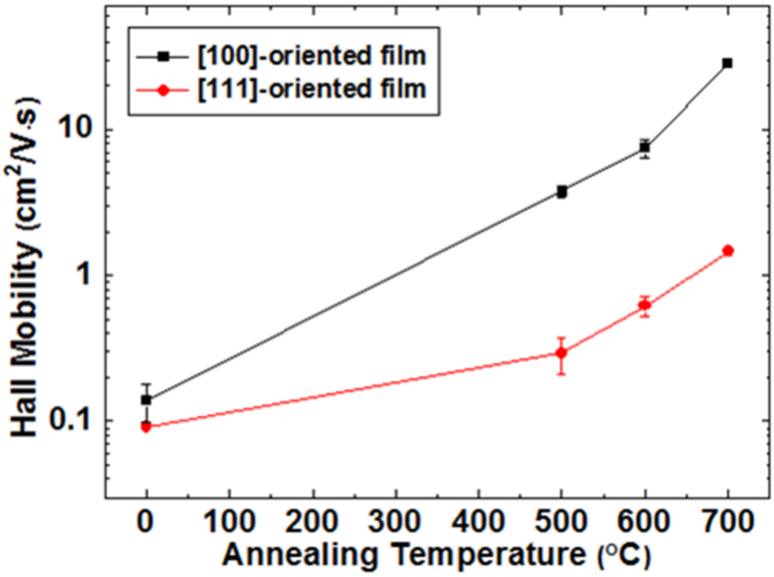

Figure 6.3. Hall mobility of [100] and [111]-oriented Cu_2O films as a function of annealing temperature.

10 min). As seen in Figure 6.3, μ_{Hall} in as-deposited films is similar for both grain orientations, while a distinct difference in the extent of mobility enhancement occurs after annealing (i.e. the [100]-oriented film shows a much more significant improvement in μ_{Hall}).

The hole effective mass for the light hole state was found to be isotropic (see Table 2.1) by DFT calculations based on the assumption that Cu_2O has a perfect crystal structure [57]. However, an actual Cu_2O film includes grain boundaries with a high degree of structural disorder causing many defects, which leads to a significant degradation of the carrier mobility. For this reason, in order to interpret the result (Figure 6.3), the degree of structural disorder in the films should be considered. It is well-known that Urbach energy (E_u) is a measure of the structural disorder in films [151, 152]. Thus, E_u was extracted using optical absorption coefficients measured by UV-visible spectroscopy and Equation (5.2) (see subsection 5.3.2 for a detailed extraction method) for comparing the level of structural disorder in the films. As seen in Figure 6.4, while E_u of the as-deposited films is

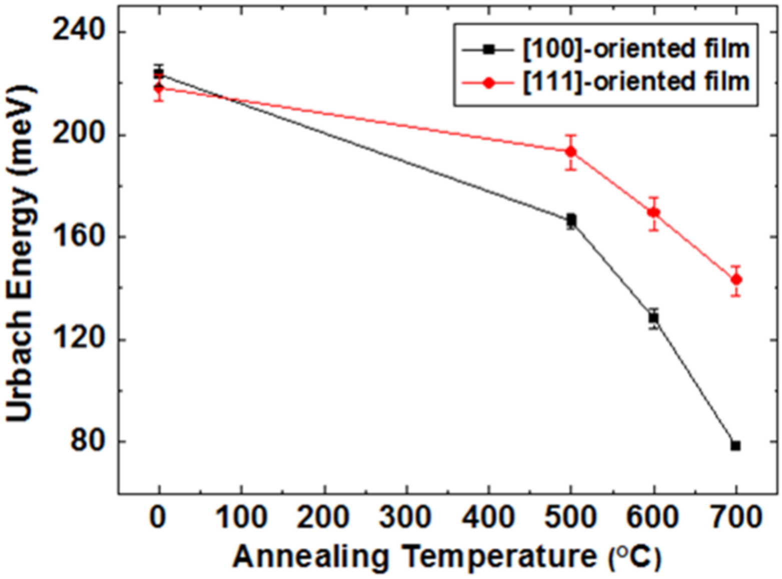

Figure 6.4. Extracted Urbach energy of [100] and [111]-oriented Cu_2O films as a function of annealing temperature.

similar for both orientations, E_u of the [100]-oriented film is reduced more significantly compared to that of the [111]-oriented film after annealing.

The similar μ_{Hall} in the as-deposited films can be explained by the isotropic hole effective mass (i.e. the same mobility in defect-free grains in the direction of [100] and [111]) and a similar E_u (i.e. a similar degree of disorder in the films). For the annealed films, based on the extracted E_u, a more significant reduction in disorder in the [100]-oriented film is considered to be the main reason that the [100]-oriented film exhibits a much higher μ_{Hall} compared to that of the [111]-oriented film.

In order to identify the main cause of the difference in the extent of the reduction in disorder by annealing between the [100] and [111]-oriented films, the crystallographic characteristic and surface morphology of the 700 ℃-annealed films were examined by XRD and SEM. As seen in Figure 6.5, annealing leads to an increase in the intensity (I) of each diffraction peak of the [100] and [111]-oriented Cu_2O films (i.e. $I_{(200)}$: 95 cps (as-deposited) → 4175 cps (700 ℃) and $I_{(111)}$: 188 cps (as-deposited) → 298 cps (700 ℃)).

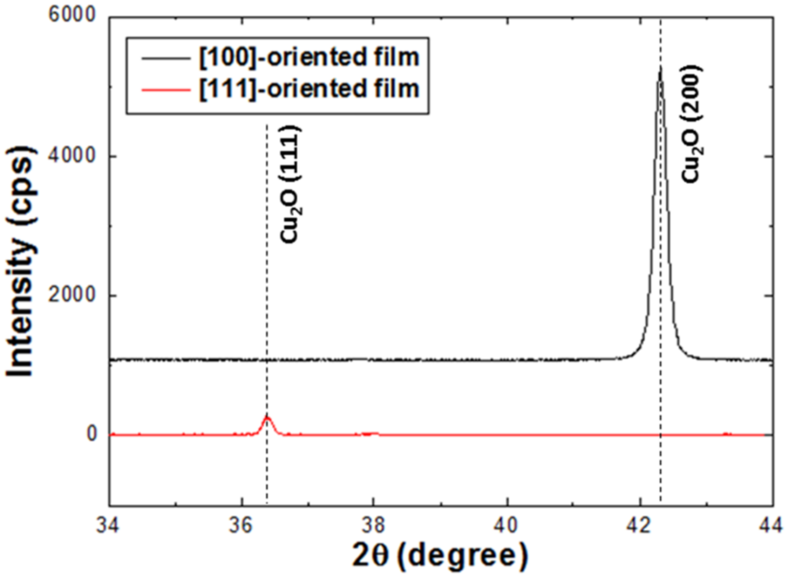

Figure 6.5. XRD patterns of [100] and [111]-oriented Cu_2O films annealed at 700 ℃.

Here, all the XRD patterns were obtained from the same XRD system (Bruker D8 Discover X-ray diffractometer) and same measurement set-up: the X-ray generator power (40 kV and 40 mA), monochromator slit size of 0.2 mm and scanspeed of 1.5 sec/step. This result indicates that crystallinity of the [100]-oriented film tends to improve more significantly than that of the [111]-oriented film after annealing, which is consistent with the extracted result of E_u (i.e. the more considerable reduction in disorder in the [100]-oriented film). In addition, it is observed that annealing leads to a slight shift of the (111) peak of the [111]-oriented Cu_2O film from 36.74° (as-deposited) to 36.46° (700 ℃) which is closer to the reference peak of 36.44° [JCPDS 04-007-9767]. This can be explained by the release of the compressive stress in the film by annealing given that the compressive stress in a film leads to a reduction in the lattice constant and this in turn results in a shift of the position of its diffraction peak to a higher angle based on Bragg's law (Equation 3.1).

As seen in the SEM images (Figure 6.6), interestingly, contrary to the [111]-oriented film, grains in the [100]-oriented film seem to be completely coalesced by annealing at 700 ℃. This suggests that the [100] grain orientation is a favourable texture for grain growth (i.e. grain coalescence) by thermal annealing. This is considered to be the main

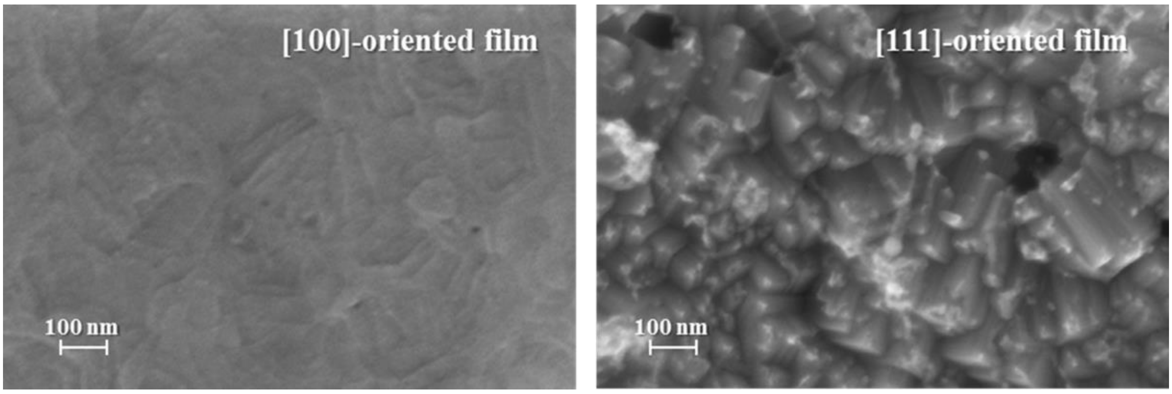

Figure 6.6. SEM images of [100] and [111]-oriented Cu_2O films annealed at 700 °C.

cause of the higher crystallinity and lower degree of disorder in the [100]-oriented Cu_2O film after annealing, which in turn results in a much higher carrier mobility compared to that of the [111]-oriented film.

6.5 Conclusions

In this chapter, it was demonstrated that the grain orientation in sputtered Cu_2O films can be controlled in the direction of either [111] or [100] by adjusting the ion-to-Cu flux ratio (J_i/J_{Cu}) incident at the growing film. Specifically, a low J_i/J_{Cu} yields Cu_2O films with the [111] grain orientation of the lowest surface energy, while an increase in J_i/J_{Cu} leads to a change in the preferred grain orientation to [100] with the highest surface energy.

In addition, a systematic investigation on the effect of the grain orientation on the carrier mobility in Cu_2O thin films was performed. This shows that the carrier mobility in as-deposited films is similar for both grain orientations due to the isotropic hole effective mass and a similar degree of disorder in the films. In contrast, after annealing, the [100]-oriented film exhibits a much higher carrier mobility due to the more enhancement of film crystallinity (i.e. more reduction in disorder in the film) compared to the [111]-oriented film. Lastly, it was found that the [100] grain orientation is favourable for grain coalescence by thermal annealing, which is believed to be the main reason for the higher crystallinity and lower degree of disorder in the [100]-oriented film after annealing. These experimental results suggest that the [100] preferred grain orientation is favourable for the Cu_2O channel layer of p-type metal oxide TFTs requiring a high carrier mobility.

Chapter 7

p-type Cu_2O thin film transistors

7.1 Introduction

A Cu_2O film level study on vacuum annealing effects was conducted in Chapter 5, which clearly showed that vacuum annealing significantly improves the carrier mobility in Cu_2O thin films without any phase conversion. In this Chapter, a TFT level investigation on the annealing effects is performed using the [100]-oriented Cu_2O thin film as an active layer based on the experimental result (Chapter 6) that the [100]-oriented Cu_2O film is more favourable than the [111]-oriented film in terms of the mobility enhancement by annealing.

In addition, most n-type metal oxide TFTs exhibit a similar μ_{FE} (10~40 $cm^2/V{\cdot}s$) to the metal oxide film mobility (i.e. μ_{Hall}) [112–116]. In contrast, p-type Cu_2O TFTs show a significantly lower μ_{FE} (<1 $cm^2/V{\cdot}s$) despite a comparable μ_{Hall} with that of n-type metal oxide films [12–14, 131], which is one of the significant challenges for developing the metal oxide-based CMOS technology. There are two possible factors behind the notable difference between μ_{FE} and μ_{Hall}: the contact resistance of source/drain (S/D) contacts and the interface traps between the channel layer and the gate insulator. Using the conventional S/D electrodes (Au) and gate insulator (thermal SiO_2), Section 7.4 studies the main origin of this effect based on the S/D contact resistance and the density of the interface traps.

Lastly, a high off-state current is widely observed in p-type Cu_2O TFTs, which leads to an unacceptably low on/off current ratio (typically $10{\sim}10^4$) [12–14, 108] compared to that ($>10^7$) of n-type metal oxide TFTs [2]. This is another significant challenge for realising

CMOS circuits using metal oxide TFTs, but the origin of the high off-state current in Cu_2O TFTs has not been identified yet. In the last part of this chapter, its main origin is identified based on capacitance-voltage (C-V) characteristics and the activation energy estimated from the temperature dependence of I_{DS} at various gate-source voltages (V_{GS}).

7.2 Experimental details

The p-type Cu_2O TFTs were fabricated in a bottom-gate staggered structure as seen in Figure 7.1 (a), where the p^+-Si (0.01~0.02 Ω·cm) and thermal SiO_2 (~260 nm) were used as a common gate electrode and a gate insulator, respectively.

Prior to Cu_2O deposition, a commercial 4 in. SiO_2/p^+-Si wafer was cleaned by solvent chemicals (acetone and IPA). After solvent cleaning, the wafer was subsequently cleaned with a sulphuric acid (H_2SO_4) and hydrogen peroxide (H_2O_2) mixture (SPM) in order to completely remove organic contaminants on the wafer surface. The volume ratio of the SPM was 4:1 (H_2SO_4:H_2O_2) and the SPM cleaning was performed for 10 min. This is an essential cleaning step for bottom-gate TFT fabrication since the organic contaminants are not completely eliminated by the solvent cleaning and this leads to high-density trap states at the Cu_2O/SiO_2 interface. However, after SPM cleaning, hygroscopic sulphur (S) residues remain on the surface and absorb moisture, which leads to sulphur-related defects on the surface [153]. In order to prevent the residues from remaining on the wafer surface, the wafer was thoroughly rinsed with DI water for 10 min. A dehydration step was then performed on a hot plate at 150 °C for 5 min to remove moisture from the surface.

Cu_2O (~130 nm) was deposited on the cleaned SiO_2/p^+-Si substrates with AZ5214E photoresist patterns to define active layers using the [100]-orientation sputtering condition (see sections 6.2 and 6.3) without intentional substrate heating. This was followed by a lift-off process in order to obtain the patterned Cu_2O active layers. The as-deposited Cu_2O

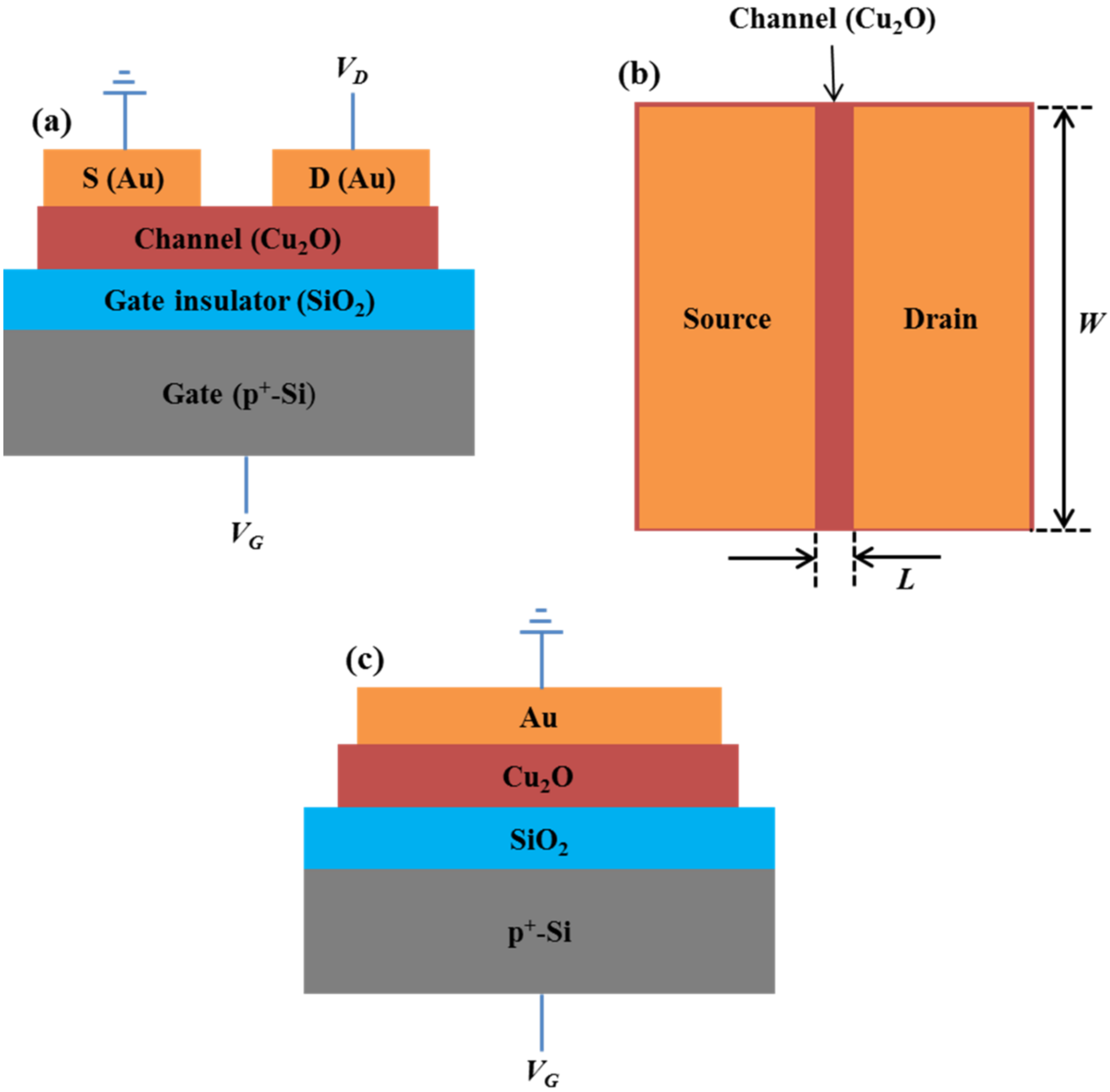

Figure 7.1. (a) A schematic cross-sectional view and (b) a top view of the Cu_2O TFT fabricated in a bottom-gate staggered structure, and (c) a schematic structure of the Cu_2O MOS capacitor. Here, V_G and V_D denote the gate and drain voltage, and L and W are the channel length and width of the fabricated TFT.

active layers were subsequently annealed in vacuum (9.5×10^{-4} mbar) at 500, 600 and 700 °C for 10 min. Au of ~100 nm thickness (without an adhesion layer) was deposited on the annealed Cu_2O active layers by a thermal evaporator, and S/D electrodes were formed by the lift-off process as seen in Figure 7.1 (b). For applying the gate voltage signal to

TFTs, Al foil was attached to the backside of the p^+-Si substrate using silver paste. The electrical characteristics were measured using an HP 4140B pA meter/DC voltage source in a dark box.

For C-V measurements of the Cu_2O active layer, metal-oxide-semiconductor (MOS) capacitors using a p^+-Si/SiO_2/Cu_2O structure with an Au top contact were simultaneously fabricated as seen in Figure 7.1 (c). The C-V characteristics were obtained by an Agilent B1500A semiconductor parameter analyzer at room temperature, where a voltage was applied to the p^+-Si through the Al foil and the Au electrode was grounded.

7.3 Annealing effects on Cu_2O TFT characteristics

7.3.1 Transfer and output characteristics

Figure 7.2 (a) shows the transfer characteristics of Cu_2O TFTs annealed at 500, 600 and 700 ℃. Here, V_{GS} was swept from –100 to +80 V at a fixed V_{DS} of –5 V. The measured TFTs have a channel width-to-length ratio (*W/L*) of 10 with a channel width of 1000 μm, and $|I_{DS}|$ is scaled by the channel width. All the TFTs show p-channel behaviour yielding an increase in $|I_{DS}|$ (i.e. channel conductivity) with an increase in the magnitude of the negative V_{GS}. In addition, an increase in annealing temperature leads to enhancement of the transfer characteristic (i.e. I_{DS} modulation by V_{GS}) in the on-state region and a decrease in an off-state current from ~1.35 nA/μm (500 °C) to ~0.1 nA/μm (700 ℃). The improvement in the transfer characteristic in the on-state regime and the reduction in the off-state current result in enhancement of the on/off current ratio from ~3 (500 ℃) to 340 (700 ℃). However, the off-state current is very high compared to the required value (< 1 pA/μm) for display applications [100]. The main origin of the high off-state current will be discussed in section 7.5. The output characteristics are shown in Figures 7.2 (b)–(d), where V_{DS} was swept from 0 to –50 V and V_{GS} was varied from +10 to –60 V in steps of –10 V. They show that the linear and saturation regions become more distinct with an increase in annealing temperature, and especially the 700 ℃-annealed sample exhibits a clear pinch-

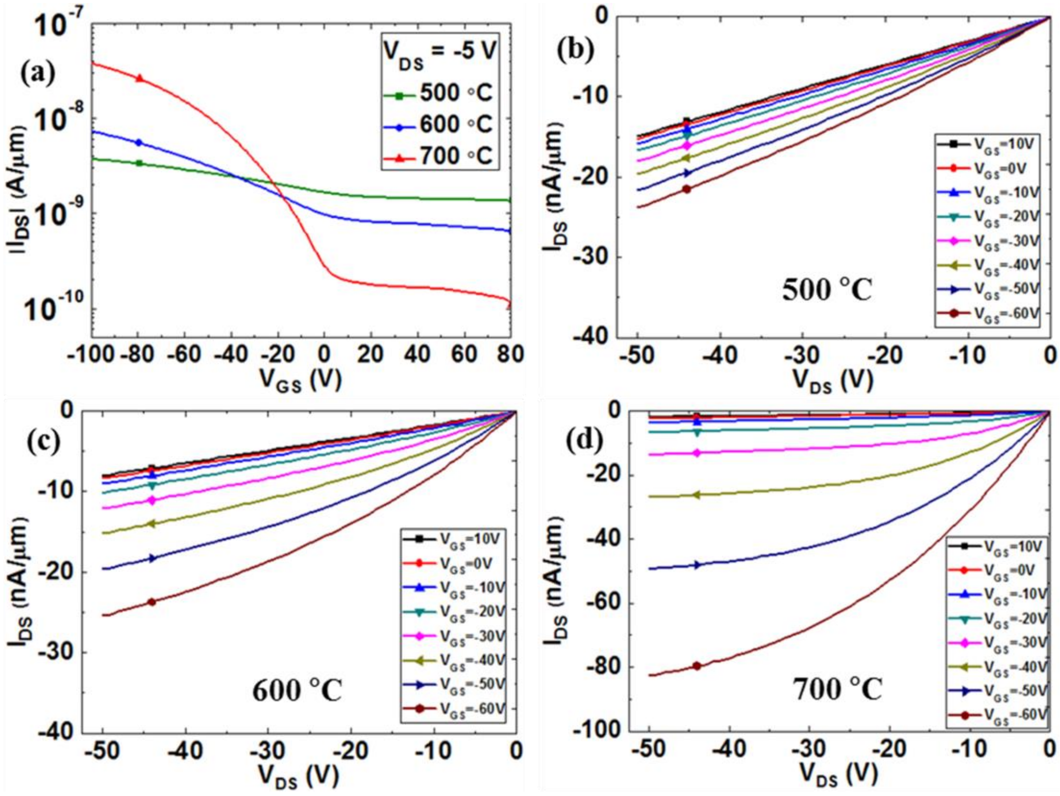

Figure 7.2. (a) Transfer characteristics of fabricated Cu_2O TFTs at V_{DS} = –5 V and output characteristics of the TFTs annealed at (b) 500, (c) 600 and (d) 700 °C. The channel length and width of the measured TFTs are 100 and 1000 µm, respectively [125].

off behaviour. This indicates that the channel controllability by V_{GS} and V_{DS} improves as annealing temperature increases. Additionally, the output characteristics in the low V_{DS} region show linear curves, indicating that S/D contacts have Ohmic-like behaviour. The S/D contact quality will be discussed in detail in the following section 7.4.

7.3.2 Field-effect mobility

In this work, since Cu_2O TFTs annealed at 500 and 600 °C do not show clear saturation regions, μ_{FE} in the linear operating region of the TFTs was estimated using the transfer curves at V_{DS} = –5 V and Equation (7.1) derived from the I_{DS} equation in the linear region (see subsection 3.3.2),

$$\mu_{FE} = \frac{\partial |I_{DS}|}{\partial V_{GS}} \frac{L}{W C_i V_{DS}}. \tag{7.1}$$

The extracted μ_{FE} as a function of V_{GS} is shown in Figure 7.3. This shows that μ_{FE} increases linearly with an increase in $|V_{GS}|$, and then saturates at high $|V_{GS}|$. The μ_{FE} dependence on the gate bias is widely observed in field-effect transistors [154–158]. Additionally, the maximum μ_{FE} improves considerably from ~0.03 $cm^2/V{\cdot}s$ (500 °C) to ~0.9 $cm^2/V{\cdot}s$ (700 °C), and especially the 700 °C-annealed sample exhibits a much higher μ_{FE} of 0.9 $cm^2/V{\cdot}s$ compared to those (10^{-3}~10^{-2} $cm^2/V{\cdot}s$) of sputter-deposited Cu_2O TFTs using post-deposition annealing [122, 131, 159].

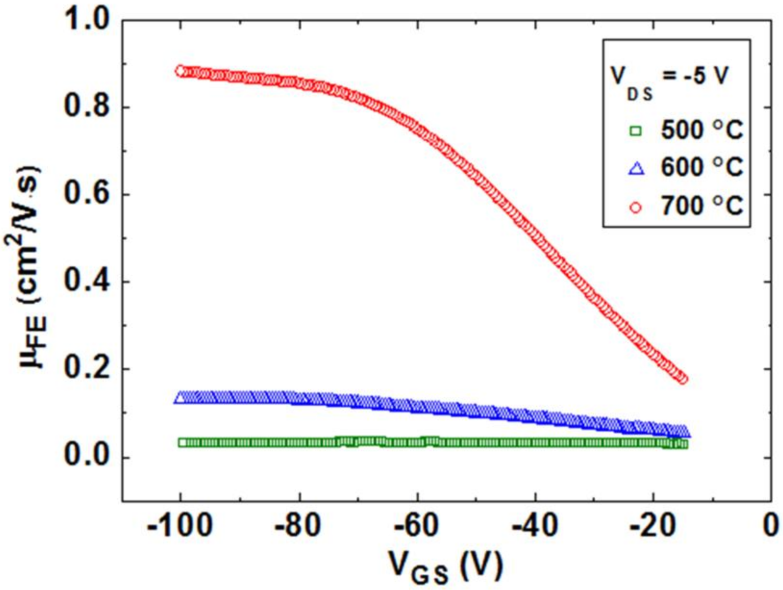

Figure 7.3. The extracted field-effect mobility of fabricated Cu_2O TFTs as a function of V_{GS} at V_{DS} = –5 V.

7.4 The origin of low field-effect mobility

The extracted μ_{FE} (~0.9 $cm^2/V{\cdot}s$) is much lower compared to the Cu_2O film mobility (μ_{Hall} = 28 $cm^2/V{\cdot}s$). This is similar to previously-reported Cu_2O TFTs [12–14, 131]. In this section, its main cause is discussed based on the S/D contact resistance and the trap density at the Cu_2O/SiO_2 interface.

7.4.1 Contact resistance

It is well known that the contact resistance (R_C) of the S/D contacts has a significant effect on μ_{FE} [98, 99]. To be specific, a TFT can be considered as a channel resistance (R_{CH}) in series with the S/D contact resistances (i.e. $2R_C$) as seen in Figure 7.4. The S/D contact resistances lead to a decrease in the effective V_{DS} ($V_{DS,eff}$) and effective V_{GS} ($V_{GS,eff}$) applied to the channel as follows [157],

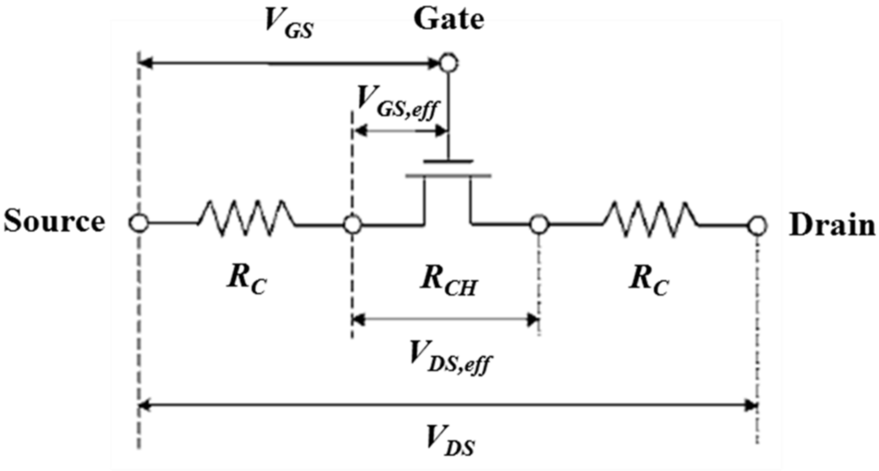

Figure 7.4. An equivalent circuit of a TFT allowing for the source and drain contact resistances. Here, R_C and R_{CH} are the contact resistance of the S/D contacts and intrinsic channel resistance, and $V_{GS,eff}$ and $V_{DS,eff}$ denote the effective V_{GS} and V_{DS} applied to the channel, respectively.

$$V_{DS,eff} = V_{DS} - I_{DS}2R_C, \tag{7.2}$$

$$V_{GS,eff} = V_{GS} - I_{DS}R_C. \tag{7.3}$$

The reduction in $V_{DS,eff}$ and $V_{GS,eff}$ by the parasitic R_C results in the degradation of an apparent μ_{FE}.

Figure 7.5 represents the extracted μ_{FE} of 700℃-annealed Cu_2O TFTs with different channel lengths as a function of V_{GS} at a fixed V_{DS} of –5 V. This shows that the μ_{FE} decreases with a reduction in the channel length. This is due to the fact that a reduction in the channel length leads to an increase in the ratio of the S/D contact resistances relative to the total resistance (i.e. $2R_C/(R_{CH}+2R_C)$) because of a decrease in R_{CH}, and thus a relatively larger fraction of the applied V_{DS} drops over the S/D contact regions for shorter channel lengths [98, 157]. Considering a much longer distance between Au contacts (e.g.

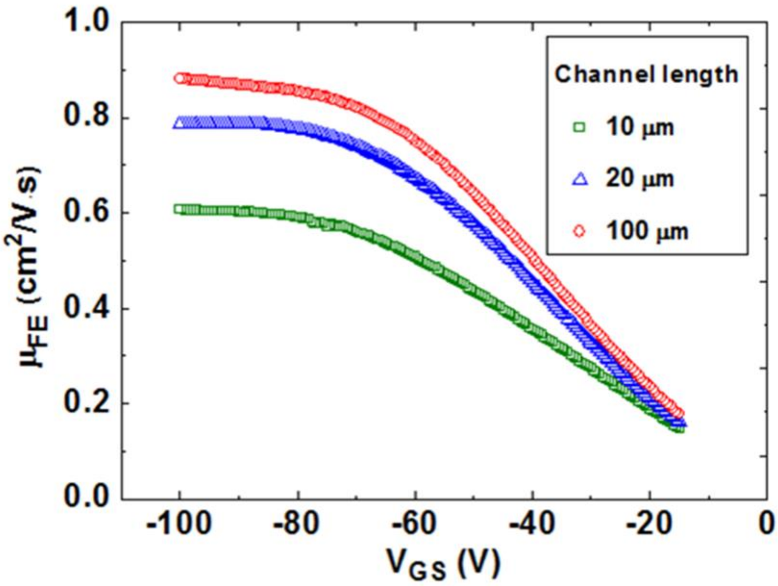

Figure 7.5. The extracted field-effect mobility of 700℃-annealed Cu_2O TFTs with different channel lengths as a function of V_{GS} at V_{DS} = –5 V.

the diagonal dimension of ~8 mm) of the van der Pauw geometry for the μ_{Hall} measurement (see Figure 3.7) compared to the channel lengths (10~100 μm) of the fabricated TFTs, the R_C effect on the measured μ_{Hall} can be negligible. Therefore, part of the significant difference between μ_{FE} and μ_{Hall} can be due to the S/D contact resistances.

As explained in subsection 3.3.3, the R_C and the channel resistance per unit channel length (R_{ch}) can be estimated using the transmission line method (TLM). Here, TFT structures with W = 1 mm and a different L (10~100 μm) were used as the TLM patterns. Additionally, contrary to silicon based field-effect transistors where the R_C is determined by a heavily doped S/D contact region, metal oxide based TFTs have the R_C dependence on V_{GS} since S/D electrodes are directly contacted with the active layer without highly doped S/D contact regions [160, 161]. For this reason, R_C as well as R_{ch} were examined for various V_{GS}.

The total resistance (R_T) was first obtained as a function of L for different V_{GS} as seen in Figure 7.6 (a). A straight line was fitted for each V_{GS}, and R_{ch} and $2R_C$ were extracted

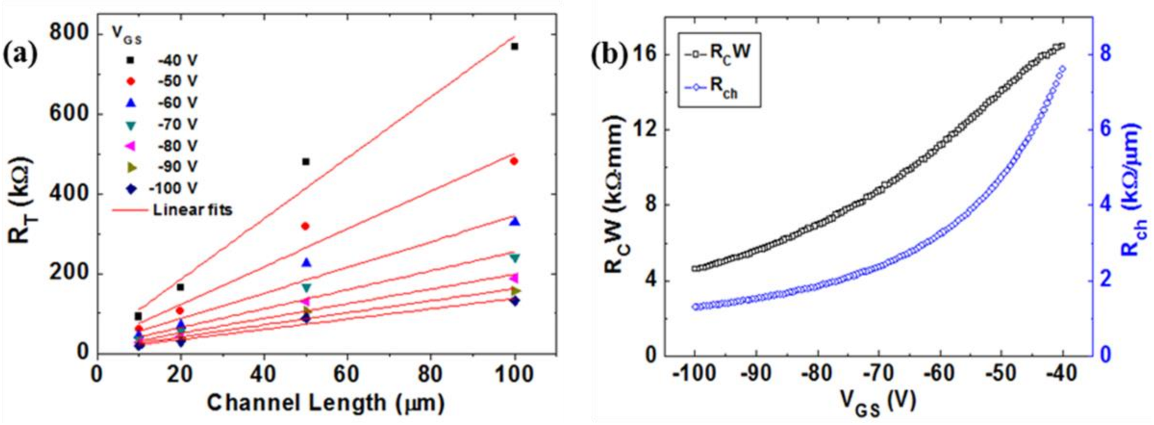

Figure 7.6. (a) The total resistance (R_T) as a function of the channel length (L) for various V_{GS} and V_{DS} = –5 V, and (b) width normalised contact resistance $R_C W$ (left-axis) and channel resistance per unit channel length R_{ch} (right-axis) extracted from the R_T-intercept and the slope, respectively, of the linear fits in (a).

from the slope and intercept on L = 0, respectively, of the linear fits of the R_T versus L plot based on $R_T = R_{ch}L + 2R_C$. The extracted R_{ch} and width normalised R_C (i.e. R_CW) as a function of V_{GS} are shown in Figure 7.6 (b). This shows that both R_{ch} and R_C decrease with an increase in $|V_{GS}|$. The decrease in R_{ch} is because as $|V_{GS}|$ increases, more holes are accumulated in the channel and this leads to an increase in the channel conductivity. Additionally, the reduction in R_C can be explained by narrowing of the Schottky barrier width resulting from an increase in the effective carrier concentration of the S/D contact regions. Specifically, based on the Schottky-Mott rule (i.e., $\Phi_B = (\chi_s + E_g) - \Phi_m$ for a metal/p-type semiconductor contact, where Φ_B, χ_s, E_g and Φ_m are the Schottky barrier height, the electron affinity and band gap of the semiconductor, and the work function of the metal, respectively) [162], it can be assumed that there is a Schottky barrier at the Au/Cu_2O contacts with $\chi_s + E_g \approx 3.2 + 2.1 = 5.3$ eV [13, 108, 163] and $\Phi_m \approx 5.1$ eV [93]. The accumulated carriers flow via the thermionic emission over the Schottky barrier, and tunneling through the thin barrier [157]. As $|V_{GS}|$ increases, more accumulated carriers flow into the S/D contact regions and this leads to an increase in the effective carrier

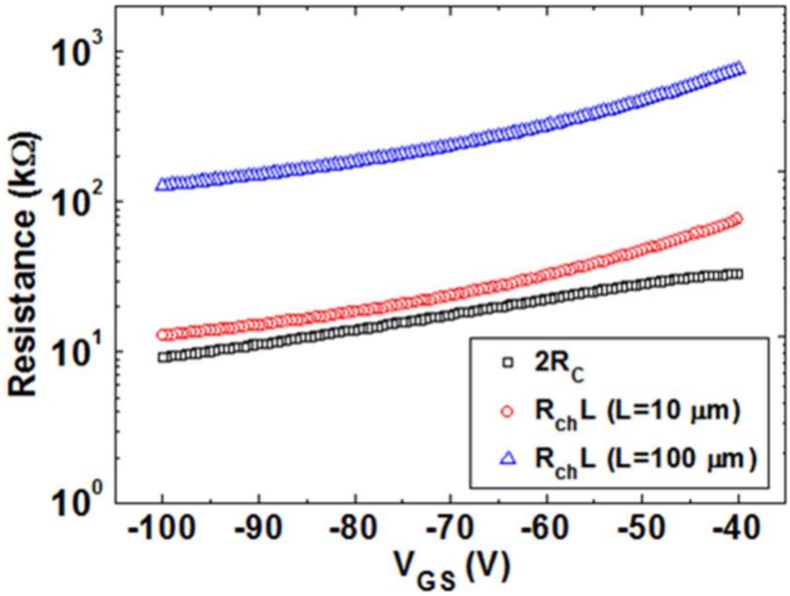

Figure 7.7. $2R_C$ and $R_{ch}L$ when L = 10 and 100 µm as a function of V_{GS}.

concentration of the contact regions, thereby narrowing the Schottky barrier width. The narrower barrier results in an increase in the tunneling current (i.e. a reduction in R_C) [157, 164].

In order to quantitatively examine the change in the ratio of the S/D contact resistances ($2R_C$) to the total resistance ($R_{ch}L + 2R_C$) according to the channel length, $2R_C$ and the channel resistances ($R_{ch}L$) when L = 10 and 100 μm as a function of V_{GS} were plotted as seen in Figure 7.7. For L = 100 μm, the channel resistance is dominant, suggesting that the R_C effect on μ_{FE} is insignificant. In contrast, the channel resistance is comparable to the S/D contact resistances for the shorter channel length of 10 μm, indicating that as a channel length decreases, the R_C effect on μ_{FE} becomes significant (see Figure 7.5).

Lastly, μ_{FE} corrected for R_C can be estimated from the derivative of the $(\Delta R_T/\Delta L)^{-1}$ versus V_{GS}. To be specific, in the linear operating region of the TFTs, the channel resistance per unit channel length is given approximately as [165, 166]

$$\frac{\Delta R_T}{\Delta L} = R_{ch} = \frac{1}{W\mu_{i,FE}C_i(V_{GS} - V_T)}, \tag{7.4}$$

where $\mu_{i,FE}$ is the intrinsic channel field-effect mobility that the R_C effect is excluded. Using Equation (7.4), $\mu_{i,FE}$ can be obtained as follows [98, 99],

$$\mu_{i,FE} = \frac{1}{WC_i}\frac{\partial\left[\left(\frac{\Delta R_T}{\Delta L}\right)^{-1}\right]}{\partial V_{GS}}. \tag{7.5}$$

The maximum $\mu_{i,FE}$ was estimated to be ~0.94 cm^2/V·s as seen in Figure 7.8. This value is similar to the apparent μ_{FE} (~0.9 cm^2/V·s) of the TFT with L = 100 μm since the channel resistance is dominant (i.e. the R_C effect is insignificant) for the channel length of 100 μm (see Figure 7.7). Thus, it can be concluded that the S/D contact resistance is not the factor causing the significant difference between μ_{FE} and μ_{Hall}.

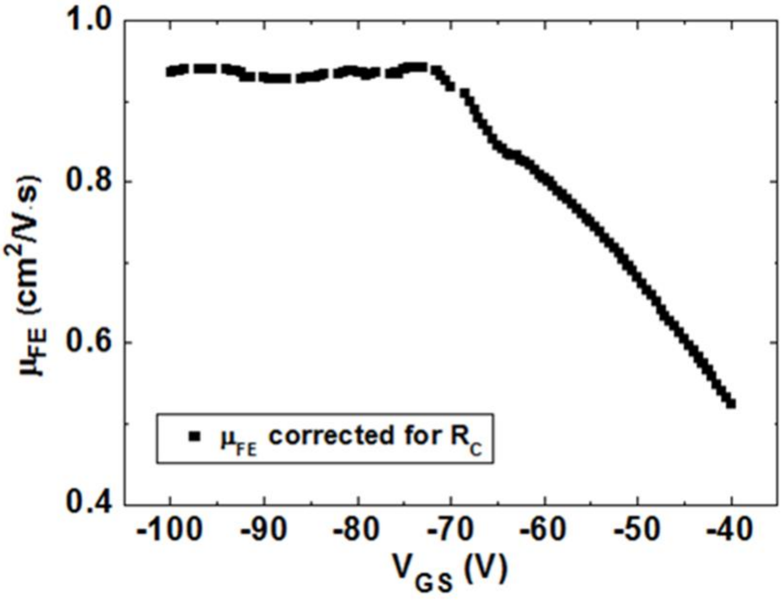

Figure 7.8. Field-effect mobility corrected for the contact resistance as a function of V_{GS}.

7.4.2 The density of interface trap states

A much higher density of trap states at the Cu_2O/SiO_2 interface than the density of Cu_2O channel bulk traps can be another possible reason causing the considerable difference between μ_{FE} and μ_{Hall} [167]. In order to confirm this quantitatively, the densities of interface traps and channel bulk traps are examined in this subsection.

It is well known that there is a correlation between the sub-threshold slope (S) and the total trap density in the bulk channel layer and at the channel/gate insulator interface as follows [101, 168, 169],

$$S = \frac{kT\ln 10}{q}\left[1 + \frac{q^2(N_{SS}t_{ch} + D_{it})}{C_i}\right] \approx \frac{qkT\ln 10(N_{SS}t_{ch} + D_{it})}{C_i}, \tag{7.6}$$

where N_{SS} and D_{it} denote the trap density in the bulk channel layer (per unit volume and unit energy) and at the channel/gate insulator interface (per unit area and unit energy), respectively. t_{ch} and $kT\ln 10/q$ are the channel layer thickness and the minimum S value (e.g. ~60 mV/dec at room temperature). Here, since the S (~26 V/dec) of the fabricated TFT is much larger than the minimum S value (60 mV), the relation between S and the total trap density can be approximated as seen in Equation (7.6). Thus, the density of the total traps (N_T) can be given as

$$N_T = N_{SS}t_{ch} + D_{it} = \frac{C_i \log(e) S}{qkT}. \tag{7.7}$$

Using Equation (7.7), N_{SS} and D_{it} can be estimated from the slope and intercept on t_{ch} = 0, respectively [115]. S values (26 V/dec for t_{ch} = 130 nm, 29.5 V/dec for t_{ch} = 260 nm) were used for extraction of N_{SS} and D_{it}, which provided N_{SS} = 3.73×10^{17} $\text{cm}^{-3}\cdot\text{eV}^{-1}$ and D_{it} = 3.12×10^{13} $\text{cm}^{-2}\cdot\text{eV}^{-1}$. Using the N_{SS} value, the area density of the traps in the channel bulk region ($N_{SS}t_{ch}$) was estimated to be 4.85×10^{12} $\text{cm}^{-2}\cdot\text{eV}^{-1}$ for t_{ch} = 130 nm, which shows that the density of interface trap states is one order higher than the density of channel bulk traps. This suggests that μ_{FE} is predominantly determined by severe carrier trapping at the Cu_2O/SiO_2 interface and this leads to the notable difference between μ_{FE} and μ_{Hall} in Cu_2O TFTs. Furthermore, considering n-type metal oxide TFTs showing a comparable μ_{FE} with μ_{Hall} [112–116], a much lower μ_{FE} of p-type Cu_2O TFTs compared to that of n-type metal oxide TFTs is mainly due to a very poor interface quality between the Cu_2O channel and gate insulator. Therefore, if the interface quality improves significantly (i.e. the interface traps are reduced to $D_{it} \ll N_{SS}t_{ch}$), it is expected that it is possible to obtain a p-channel μ_{FE} as high as that of n-type metal oxide TFTs.

7.5 The origin of high off-state current

In order to achieve full depletion of the Cu_2O channel layer, t_{ch} must be thinner than the maximum depletion width (x_{dT}) [135, 170],

$$t_{ch} < x_{dT} = \left(\frac{4\varepsilon_0 \varepsilon_{Cu2O} \Phi_b}{qN_{ch}}\right)^{1/2}, \tag{7.8}$$

where ε_0, ε_{Cu2O} and N_{ch} denote the vacuum permittivity, the dielectric constant of Cu_2O and the carrier density in the channel layer, and Φ_b (in volts) is the Cu_2O bulk potential which is defined by $\{E_g/2 - (E_F - E_V)\}/q$. The Cu_2O static dielectric constant at 293 K is 7.5 [171]. N_{ch} is 1.85×10^{13} cm^{-3} (see the Hall measurement result in Table 5.1) and the resultant Φ_b is 0.71 V. Using these parameters and Equation (7.8), x_{dT} is estimated to be ~8 μm, which is much larger than t_{ch} = 130 nm. Thus, the fabricated TFTs are expected to be fully depleted in the off-state. However, as seen in Figure 7.2 (a), the fabricated Cu_2O TFTs suffer from an unacceptably high off-state current like previously-reported Cu_2O TFTs [12–14, 108].

7.5.1 Minority carrier accumulation

In order to investigate the origin of the high off-state current in Cu_2O TFTs, the C-V characteristic of the Cu_2O channel layer was measured using a Cu_2O MOS capacitor as seen in Figure 7.9. In contrast to the C-V characteristics of n-type metal oxides such as IGZO where minority carrier (hole) accumulation does not occur [172, 173], surprisingly, Figure 7.9 shows that minority carriers (electrons) are accumulated in the off-state regime. The formation energy versus E_F plot for intrinsic defects in Cu_2O (see Figure 2.8) provides a possible explanation for where the electrons come from. Specifically, there are two potential donors for the minority carriers (electrons) in p-type Cu_2O: oxygen vacancies (V_O) and copper interstitials (Cu_i). The V_O are only stable in the charge-neutral state considering the fact that there is no charge transition level in the band gap, and therefore they cannot act as donors [9, 54]. By contrast, Cu_i exhibit the amphoteric characteristic with both $\varepsilon(+/0)$

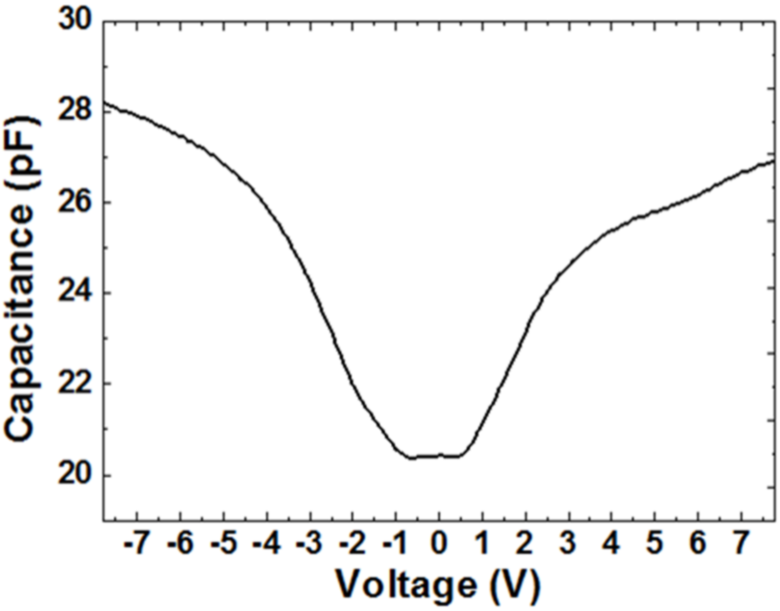

Figure 7.9. The low frequency (500 kHz) capacitance-voltage characteristics of a Cu_2O MOS capacitor [174].

and ε(0/-) charge transition points in the band gap. The ε(+/0) is at E_V + 1.3 eV [54], meaning that when $E_F - E_V$ < 1.3 eV, Cu_i become positively charged (i.e. they act as donors for minority carriers in p-type Cu_2O. This suggests that the electrons come from Cu_i defects in Cu_2O.

7.5.2 Fermi energy pinning

In order to confirm that the accumulated electrons are the source of the high off-state current in p-type Cu_2O TFTs, a change in the E_F position within the channel according to V_{GS} is examined in this subsection. The thermally activated I_{DS} is described as follows,

$$I_{DS} = I_{DS0} \exp\left(\frac{-E_a}{kT}\right). \tag{7.9}$$

Here, E_a is the activation energy which represents the position of E_F relative to either the valence band (i.e. $E_F - E_V$) for a p-type channel or the conduction band (i.e. $E_C - E_F$) for an n-type channel [175, 176]. Equation (7.9) may be expressed as

$$\ln(|I_{DS}|) = \frac{-E_a}{kT} + \ln(|I_{DS0}|), \tag{7.10}$$

and thus E_a can be estimated from the slope of an $\ln(|I_{DS}|)$ versus $1/kT$ plot (see Figure 7.10 (a)). Figure 7.10 (b) shows the extracted E_a as a function of V_{GS}. Contrary to n-type IGZO TFTs showing an increase in E_a in the off-state regime [176], this shows that E_a is reduced abruptly in the off-state regime. This indicates that E_F becomes closer to the conduction band (i.e. the channel inverts from p-type to n-type), which is consistent with the C-V characteristic of Figure 7.9.

Furthermore, interestingly, E_F is not modulated by V_{GS} in the off-state regime as seen in Figure 7.10 (b). This normally indicates that E_F is pinned in subgap states [177], which in this case is due to subgap states in the upper half of the band gap. It was demonstrated

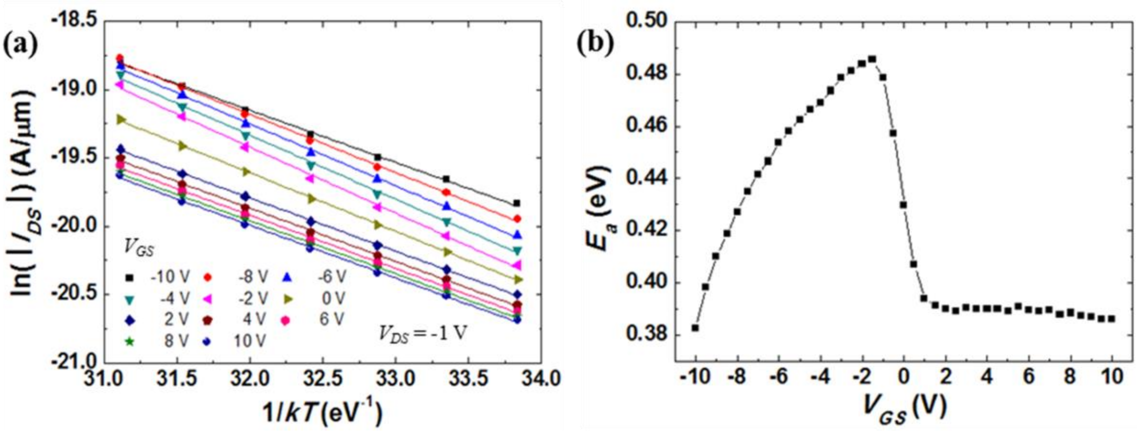

Figure 7.10. (a) Temperature dependence of I_{DS} at V_{DS} = –1 V for various V_{GS} and (b) activation energy extracted from the slopes in (a) as a function of V_{GS} [174].

that there exist subgap states at ~0.38 eV below the conduction band in Cu_2O based on photoconductivity [178] and photoluminescence [179] measurements. As for the origin of the subgap states, the authors [178, 179] argued that the subgap states originate from V_O, but Scanlon *et al.* strongly suggested that the V_O level is actually located below the valence band and therefore V_O cannot be the origin of the subgap states based on DFT analysis [54]. Although the source of these subgap states is not certain, it is likely that they cause the E_F pinning near 0.38 eV below the conduction band observed in the Cu_2O TFTs in this work. The conduction mechanism of the accumulated electrons in the off-state can be explained by variable range hopping (VRH) conduction between the localised subgap states near the Fermi energy (i.e. 0.38 eV below the CBM).

In the VRH model [180, 181], the conductivity (σ) of materials where VRH is the dominant conduction mechanism is given by [182]

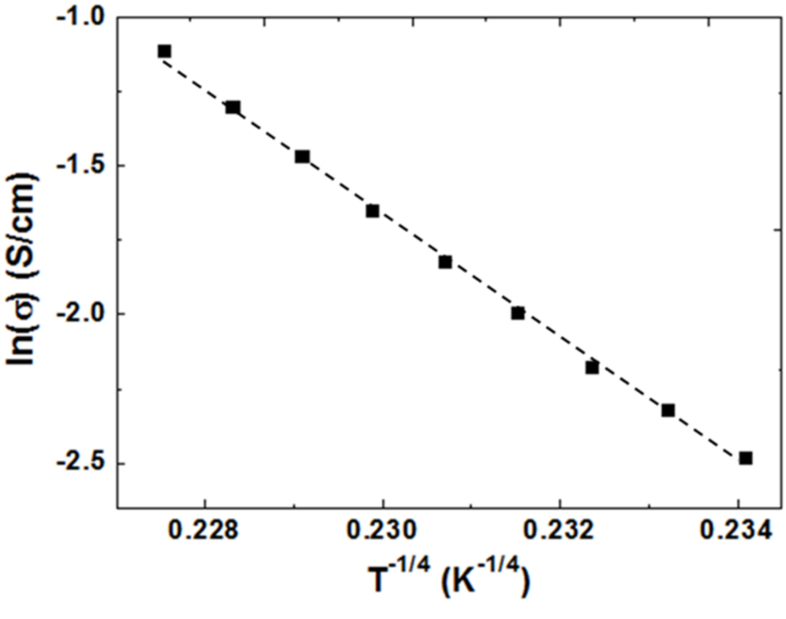

Figure 7.11. Temperature dependence of the conductivity plotted as $\ln\sigma$ versus $T^{-1/4}$, showing a linear relation between $\ln\sigma$ and $T^{-1/4}$ (i.e. a variable range hopping conduction).

$$\sigma = \sigma_0 \exp\left[-\left(\frac{T_0}{T}\right)^{1/4}\right], \tag{7.11}$$

where σ_0 and T_0 denote a pre-exponential factor and a characteristic temperature coefficient, respectively. Based on Equation (7.11) (Mott law), a linear relation between $\ln\sigma$ and $T^{-1/4}$ is indicative of the VRH conduction [123, 182, 183]. Figure 7.11 shows the $\ln\sigma$ versus $T^{-1/4}$ plot where σ was obtained from the off-state current at V_{GS} = 5 V and V_{DS} = –1 V. The linear dependence of $\ln\sigma$ and $T^{-1/4}$ in Figure 7.11 indicates that the VRH conduction of the accumulated electrons causes the high off-state current in p-type Cu_2O TFTs.

Using Mott's model of the VRH conduction, the hopping probability (P) between localised states with distance l and energy ΔE is given as

$$\begin{aligned} P &= v_0 \exp\left(\frac{-2l}{l_0} - \frac{\Delta E}{kT}\right) \quad \text{for } \Delta E > 0, \\ P &= v_0 \exp\left(\frac{-2l}{l_0}\right) \qquad\qquad \text{for } \Delta E \leq 0, \end{aligned} \tag{7.12}$$

where l is the distance between localised states, and v_0 and l_0 denote an attempt-to-escape frequency and the spatial extent of the wavefunction [132, 182]. Equation (7.12) shows the dependence of the hopping probability and the distance between localised states (i.e. hopping sites). Based on this, the high off-state current in Cu_2O TFTs can decrease by reducing the subgap states near 0.38 eV below the conduction band.

Lastly, transfer characteristics as a function of V_{DS} and the channel length are shown in Figure 7.12. In contrast to n-type IGZO TFTs, where minority carrier accumulation does not occur in the off-state, showing no dependence of the off-state current on V_{DS} [184] and the channel length [185], Figure 7.12 shows that as $|V_{DS}|$ increases and the channel length decreases, the off-state current increases. This can be explained by the off-state channel resistance attributable to the accumulated electrons. Specifically, because of the off-state

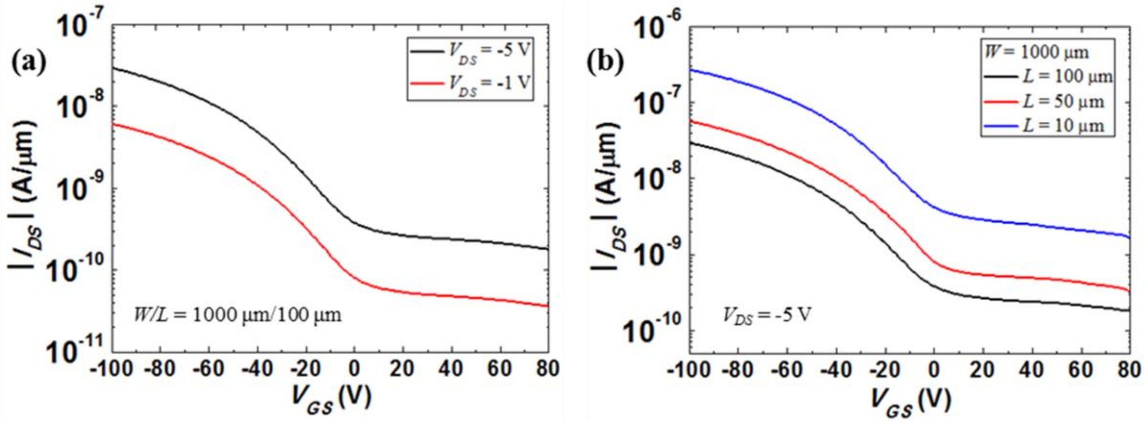

Figure 7.12. Transfer characteristics as a function of (a) V_{DS} of Cu_2O TFTs with a channel length of 100 μm, and (b) the channel length at a fixed V_{DS} of –5 V [174].

channel resistance, the off-state current increases with an increase in $|V_{DS}|$ based on Ohm's law (see Figure 7.12 (a)). In addition, a decrease in the channel length means a reduction in the off-state channel resistance, thereby increasing the off-state current as seen in Figure 7.12 (b). The dependence of the off-state current on V_{DS} and the channel length further supports the finding that the accumulated electrons cause the high off-state current in Cu_2O TFTs.

7.6 Conclusions

By vacuum annealing, the performance of p-type Cu_2O TFTs improves significantly: both in terms of μ_{FE} and the on/off current ratio. Cu_2O TFTs annealed at 700 °C exhibited μ_{FE} of ~0.9 $cm^2/V{\cdot}s$ and an on/off current ratio of ~3.4×10^2.

However, a significant difference between μ_{FE} and μ_{Hall} was observed, and this has been previously reported for Cu_2O TFTs. Its main origin was discussed on the basis of the S/D contact resistance and the density of Cu_2O/SiO_2 interface traps. It was demonstrated that although the R_C effect on μ_{FE} becomes significant with a decrease in the channel length, the R_C effect on μ_{FE} in a long-channel TFT with a channel length of 100 μm is insignificant since the channel resistance is dominant, which was quantitatively confirmed by an extracted intrinsic channel field-effect mobility similar to an apparent μ_{FE}. Instead, it was found that the density of Cu_2O/SiO_2 interface traps is one order higher than the density of Cu_2O channel bulk traps. This indicates that the considerable difference between μ_{FE} and μ_{Hall} in Cu_2O TFTs is because μ_{FE} is significantly degraded by severe carrier trapping at the Cu_2O/SiO_2 interface. Considering a similar μ_{FE} to μ_{Hall} in n-type metal oxide TFTs, a very poor interface quality between the Cu_2O channel and gate insulator is considered to be the main reason why p-type Cu_2O TFTs exhibit a much lower μ_{FE} than that of n-type metal oxide TFTs even though Cu_2O films have a comparable μ_{Hall} with that of n-type metal oxide films. Thus, if the interface quality enhances considerably, it is expected to obtain a comparable p-channel μ_{FE} with that of n-type metal oxide TFTs.

In the last part of this chapter, the main origin of the high off-state current in p-type Cu_2O TFTs was investigated based on the activation energy, extracted from the temperature dependence of I_{DS}, as a function of V_{GS} along with the C-V characteristics. This shows minority carrier (electron) accumulation and pinning of the Fermi energy in the off-state. The electron accumulation and E_F pinning are considered to be due to minority carriers coming from Cu_i defects in Cu_2O and the subgap states near 0.38 eV below the conduction band, respectively. The linear relation between $\ln\sigma$ and $T^{-1/4}$ in the off-state indicates that the electron hopping conduction among the subgap states causes the high off-state current in Cu_2O TFTs. Therefore, reducing the subgap states is critical for lessening the off-state current (i.e. enhancing the switching ratio) in Cu_2O TFTs.

The findings in this chapter provide the understanding of the main origins of the significantly low field-effect mobility and unacceptably high off-state current in Cu_2O TFTs. These also suggest the research direction (i.e. improvement in the interface quality between the Cu_2O channel and gate insulator, and a reduction in the subgap states near 0.38 eV below the CBM) for achieving high-quality p-type Cu_2O TFTs comparable to n-type metal oxide TFTs.

Chapter 8

Conclusions and future work

This chapter briefly recounts the significant contributions presented in this thesis and suggests the future research direction for realising high quality p-type Cu_2O TFTs.

8.1 Summary of key findings

The first major contribution of this thesis was to provide detailed insight into annealing effects on nanocrystalline Cu_2O thin film characteristics with particular focus on an in-depth discussion of the effect on the carrier mobility. To be specific, it was observed that an increase in annealing temperature gives rise to (1) an improvement in film crystallinity, (2) widening of the optical band gap, (3) a decrease in Urbach energy, (4) an increase in carrier mobility and (5) a significant reduction in carrier density. Based on the reduction in Urbach energy, the increase in the optical band gap can be understood as a decrease in the band tail width. Through a quantitative analysis of the relative dominance of the main conduction mechanisms (i.e. grain-boundary-limited and trap-limited conduction) in nanocrystalline Cu_2O thin films, it was found that the low carrier mobility of as-deposited Cu_2O is mainly due to grain-boundary-limited conduction. In contrast, after high-temperature annealing, grain-boundary-limited conduction becomes insignificant because of a significant reduction in the energy barrier height at grain boundaries, leading to an increase in the carrier mobility. However, it was found that the carrier mobility in the annealed films is still limited by carrier trapping at localised tail states (i.e. trap-limited conduction), suggesting that more effort to reduce the tail states is required for a further improvement in the carrier mobility.

The second major contribution was to demonstrate that the grain orientation in sputtered Cu_2O films can be varied in the direction of either [111] or [100] by controlling the incident ion-to-Cu flux ratio. This allowed a systematic study on the effect of the grain orientation on the carrier mobility in Cu_2O films. It was found that the as-deposited films exhibit a similar carrier mobility for both grain orientations because of the isotropic hole effective mass and a similar degree of disorder in the films. In contrast, a more significant reduction in disorder occurs in the [100]-oriented film by annealing, thereby resulting in a much higher carrier mobility than that of the [111]-oriented films after similar annealing. This finding indicates that the [100] preferred orientation is more suitable for the Cu_2O channel layer where a high carrier mobility is desired.

The third major contribution was to throw light on the main origins of the considerably degraded field-effect mobility (μ_{FE}) relative to Hall mobility (μ_{Hall}) and high off-state current; these are the two most significant challenges for the development of high performance Cu_2O TFTs. Specifically, using the conventional source/drain (S/D) electrodes (Au) and gate insulator (thermal SiO_2), the former cause was discussed based on the S/D contact resistance and the density of Cu_2O/SiO_2 interface traps. It was found that the effect of the contact resistance (R_C) on μ_{FE} is insignificant in the case of long-channel TFTs, which was confirmed by a similar value of the apparent μ_{FE} and intrinsic channel field-effect mobility that the R_C effect is excluded. On the contrary, the density of Cu_2O/SiO_2 interface traps was found to be one order higher than the density of Cu_2O channel bulk traps. This suggests that the significant reduction in μ_{FE} compared to μ_{Hall} is mainly due to severe carrier trapping at the Cu_2O/SiO_2 interface. As for the main cause of the high off-state current in p-type Cu_2O TFTs, minority carrier (i.e. electron) accumulation and pinning of the Fermi energy at around 0.38 eV below the conduction band were observed in the off-state. The electrons are considered to come from copper interstitials acting as donors for minority carriers in p-type Cu_2O. It was already demonstrated by photoconductivity and photoluminescence measurements that there exist subgap states at ~0.38 eV below the conduction band in Cu_2O. Considering this, the subgap states near 0.38 eV below the conduction band are believed to cause the E_F pinning observed in the Cu_2O TFTs in this work. The off-state current was found to follow Mott's model of the variable range hopping conduction (i.e. a linear relation between $\ln\sigma$ and $T^{-1/4}$), indicating that electron hopping conduction among the subgap states causes the high off-state current in Cu_2O TFTs.

8.2 Future work

These findings suggest the future research direction for solving the two significant challenges (i.e. very low field-effect mobility and high off-state current) to the development of high quality p-type Cu_2O TFTs comparable to n-type metal oxide TFTs.

1) Low field-effect mobility: Given that n-type metal oxide TFTs generally exhibit a similar μ_{FE} to μ_{Hall} and Cu_2O films can have a comparable μ_{Hall} with that of n-type oxide films, it is expected that the improvement in the poor quality of the Cu_2O channel/gate insulator interface allows the realisation of a p-channel μ_{FE} as high as that of n-type TFTs. Therefore, more effort to improve the interface quality (i.e. reduce the interface trap density) is required.

   The interface quality can be engineered by several methods:

   (1) Chemical treatments on the gate insulator surface prior to deposition of the Cu_2O channel layer;

   (2) Plasma treatments on the gate insulator surface;

   (3) The use of the buffer layer between the gate insulator and the Cu_2O channel layer.

   Considering a small lattice mismatch of only 1.4 % between MgO and Cu_2O [12], MgO is expected to provide a high quality interface with the Cu_2O channel layer, and therefore it seems to be the best candidate for either the buffer layer or the gate insulator.

2) High off-state current: The experimental results indicate that electron hopping conduction among the subgap states near 0.38 eV below the conduction band causes

the high off-state current in Cu_2O TFTs, and therefore reducing the subgap states is critical for lessening the high off-state current.

Based on the experimental results, the high off-state current might be reduced by the following methods.

(1) It is well known that thermal annealing can reduce the density of subgap states in disordered materials. Thus, although the origin of the subgap states at around 0.38 eV below the conduction band is not certain, their density is expected to decrease by optimisation of the annealing condition (e.g. the temperature ramp rate and annealing time).

(2) In the case of a-Si:H TFTs, although minority carriers (holes) are accumulated in the off-state, the hole flow is blocked by n^+-doped S/D contact regions [27, 175], and thus the effect of holes on the off-state current is negligible. Considering this, the high off-state current in p-type Cu_2O TFTs might be significantly reduced by forming p^+-doped S/D contact regions since it is expected that the p^+-doped S/D regions block the electron flow in the off-state.

References

[1] Nathan, A. *et al.* Flexible electronics: The next ubiquitous platform. *Proc. IEEE* **100**, 1486–1517 (2012).

[2] Fortunato, E., Barquinha, P., and Martins, R. Oxide semiconductor thin-film transistors: A review of recent advances. *Adv. Mater.* **24**, 2945–2986 (2012).

[3] Lee, S. and Nathan, A. Subthreshold Schottky-barrier thin-film transistors with ultralow power and high intrinsic gain. *Science* **354**, 302–304 (2016).

[4] Presley, R. E. *et al*. Transparent ring oscillator based on indium gallium oxide thin-film transistors. *Solid-State Electron.* **50**, 500–503 (2006).

[5] Kim, K. H., Kim, Y. H., Kim, H. J., Han, J. I., and Park, S. K. Fast and stable solution processed transparent oxide thin-film transistor circuits. *IEEE Electron Device Lett.* **32**, 524–526 (2011).

[6] Huang, T-C. Pseudo-CMOS: A design style for low-cost and robust flexible electronics. *IEEE Trans. Electron Devices* **58**, 141–150 (2011).

[7] Na, J. H., Kitamura, M., and Arakawa, Y. Organic/inorganic hybrid complementary circuits based on pentacene and amorphous indium gallium zinc oxide transistors. *Appl. Phys. Lett.* **93**, 213505 (2008).

[8] Kris, MYNY. Organic digital circuits by technology improvement and robust digital design. PhD Thesis, *Katholieke Universiteit Leuven* (2013).

[9] Raebiger, H., Lany, S., and Zunger, A. Origins of the p-type nature and cation deficiency in Cu_2O and related materials. *Phys. Rev. B* **76**, 045209 (2007).

[10] Yanagi, H., Kawazoe, H., Kudo, A., Yasukawa, M., and Hosono, H. Chemical design and thin film preparation of *p*-Type conductive transparent oxides. *J. Electroceram.* **4**, 407–414 (2000).

[11] Kawazoe, H., Yanagi, H., Ueda, K., and Hosono, H. Transparent *p*-Type conducting oxides: Design and fabrication of *p-n* heterojunctions. *MRS Bull.* **25**, 28–36 (2000).

[12] Matsuzaki, K. *et al*. Epitaxial growth of high mobility Cu_2O thin films and applications to p-channel thin film transistor. *Appl. Phys. Lett*. **93**, 202107 (2008).

[13] Fortunato, E. *et al*. Thin-film transistors based on p-type Cu_2O thin films produced at room temperature. *Appl. Phys. Lett.* **96**, 192102 (2010).

[14] Kim, S. Y. *et al*. p-channel oxide thin film transistors using solution-processed copper oxide. *ACS Appl. Mater. Interfaces* **5**, 2417–2421 (2013).

[15] Flewitt, A. J. *et al.* Stability of thin film transistors incorporating a zinc oxide or indium zinc oxide channel deposited by a high rate sputtering process. *Semicond. Sci. Technol.* **24**, 085002 (2009).

[16] Lilienfield, J. E. *U.S. Patent* 1745175 (1930).

[17] Lilienfield, J. E., *U.S. Patent* 1900018 (1933).

[18] Weinser, P. K. The TFT–a new thin-film transistor. *Proc. IRE* **50**, 1462–1469 (1962).

[19] Klasens, H. A. and Koelmans, H. A tin oxide field-effect transistor. *Solid-State Electron.* **7**, 701–702 (1964).

[20] Boesen, G. F., Jacobs, J. E. ZnO field-effect transistor. *Proceedings of the IEEE* **56**, 2094–2095 (1968).

[21] Fortunato, E. *et al*. Recent advances in ZnO transparent thin film transistors. *Thin Solid Films* **487**, 205–211 (2005).

[22] Brody, T. P., Asars, J. A., and Dixon, G. D. A 6×6 inch 20 lines-per-inch liquid crystal display panel. *IEEE Trans. Electron Devices* **20**, 995–1001 (1973).

[23] LeComber, P. G., Spear, W. E., and Gaith, A. Amorphous-silicon field-effect device and possible application. *Electron. Lett.* **15**, 179–181 (1979).

[24] Kuo, Y. *Thin Film Transistors–Materials and Processes*, vol. 1 (Kluwer Academic Publishers, 2004).

[25] Kamiya, T. and Hosono, H. Material characteristics and applications of transparent amorphous oxide semiconductors. *NPG Asia Mater.* **2**, 15–22 (2010).

[26] Kamiya, T., Nomura, K., and Hosono, H. Present status of amorphous In–Ga–Zn–O thin-film transistors. *Sci. Technol. Adv. Mater.* **11**, 044305 (2010).

[27] Liu, T. *Stability of Amorphous Silicon Thin Film Transistors and Circuits*, PhD Thesis, Princeton University (2013).

[28] Jeong, J. K., Mo Y.-G., Ryu M. K., and Yang S., in *Int. Workshop on Transparent Amorphous Oxide Semiconductors 2010*, Tokyo, Japan, 25–26 January 2010.

[29] Nishii, J. *et al.* High mobility thin film transistors with transparent ZnO channels. *Jpn J. Appl. Phys.* **42**, L347–L349 (2003).

[30] Masuda, S., Kitamura, K., Okumura, Y., and Miyatake, S. Transparent thin film transistors using ZnO as an active channel layer and their electrical properties. *J. Appl. Phys.* **93**, 1624–1630 (2003).

[31] Hoffman, R. L., Norris, B. J., and Wager, J. F. ZnO-based transparent thin-film transistors. *Appl. Phys. Lett.* **82**, 733–735 (2003).

[32] Carcia, P. F., McLean, R. S., Reilly, M. H., and Nunes, G. Transparent ZnO thin-film transistor fabricated by rf magnetron sputtering. *Appl. Phys. Lett.* **82**, 1117–1119 (2003).

[33] Nomura, K. *et al*. Thin-film transistor fabricated in single-crystalline transparent oxide semiconductor. *Science* **300**, 1269–1272 (2003).

[34] Kamiya, T., Nomura, K., and Hosono, H. Origins of high mobility and low operation voltage of amorphous oxide TFTs: Electronic structure, electron transport, defects and doping. *J. Display Technol.* **5**, 273–288 (2009).

[35] Nomura, K. *et al*. Room-temperature fabrication of transparent flexible thin-film transistors using amorphous oxide semiconductors. *Nature* **432**, 488–492 (2004).

[36] Suresh, A., Wellenius, P., Dhawan, A., and Muth, J. Room temperature pulsed laser deposited indium gallium zinc oxide channel based transparent thin film transistors. *Appl. Phys. Lett.* **90**, 123512 (2007).

[37] Park, J.-S., Jeong, J. K., Mo, Y.-G., Kim, H. D., and Kim, S.-I. Improvements in the device characteristics of amorphous indium gallium zinc oxide thin-film transistors by Ar plasma treatment. *Appl. Phys. Lett.* **90**, 262106 (2007).

[38] Barquinhaz, P., Pereira, L., Gonçalves, G., Martins, R., and Fortunato, E. Toward high-performance amorphous GIZO TFTs. *J. Electrochem. Soc.* **156**, H161–H168 (2009).

[39] Niang, K. M. *et al.* A thermalization energy analysis of the threshold voltage shift in amorphous indium gallium zinc oxide thin film transistors under positive gate bias stress. *Appl. Phys. Lett.* **108**, 093505 (2016).

[40] Yaglioglu, B., Yeom, H. Y., Beresford, R., and Paine, D. C. High-mobility amorphous In_2O_3–10 wt %ZnO thin film transistors. *Appl. Phys. Lett.* **89**, 062103 (2006).

[41] Paine, D. C., Yaglioglu, B., Beiley, Z., and Lee, S. Amorphous IZO-based transparent thin film transistors. *Thin Solid Films* **516**, 5894–5898 (2008).

[42] Chiang, H. Q., Wager, J. F., Hoffman, R. L., Jeong, J., and Keszler, D. A. High mobility transparent thin-film transistors with amorphous zinc tin oxide channel layer. *Appl. Phys. Lett.* **86**, 013503 (2005).

[43] Jackson, W. B., Hoffman, R. L., and Herman, G. S. High-performance flexible zinc tin oxide field-effect transistors. *Appl. Phys. Lett.* **87**, 193503 (2005).

[44] Hoffman, R. L. Effects of channel stoichiometry and processing temperature on the electrical characteristics of zinc tin oxide thin-film transistors. *Solid State Electron.* **50**, 784–787 (2006).

[45] Niang, K. M., Cho, J., Heffernan, S., Milne, W. I., and Flewitt, A. J. Optimisation of amorphous zinc tin oxide thin film transistors by remote-plasma reactive sputtering. *J. Appl. Phys.* **120**, 085312 (2016).

[46] Niang, K. M. *et al*. Zinc tin oxide thin film transistors produced by a high rate reactive sputtering: Effect of tin composition and annealing temperatures. *Phys. Status Solidi A* **214**, 1600470 (2017).

[47] Robertson, J. and Falabretti, B. *Handbook of Transparent Conductors* (ed. Ginley, D. S.). Chap. 2 (Springer, 2011).

[48] Zhang, S. B., Wei, S.-H., and Zunger, A. Intrinsic *n*-type versus *p*-type doping asymmetry and the defect physics of ZnO. *Phys. Rev. B* **63**, 075205 (2001).

[49] Park, C. H., Zhang, S. B., and Wei, S.-H. Origin of *p*-type doping difficulty in ZnO: The impurity perspective. *Phys. Rev. B* **66**, 073202 (2002).

[50] Janotti, A. and Van de Walle, C. G. Fundamentals of zinc oxide as a semiconductor. *Rep. Prog. Phys.* **72**, 126501 (2009).

[51] Lyons, J. L., Janotti, A., and Van de Walle, C. G. Why nitrogen cannot lead to *p*-type conductivity in ZnO. *Appl. Phys. Lett.* **95**, 252105 (2009).

[52] Yamamoto, T. and Yoshida, H. K. Solution using a codoping method to *unipolarity* for the fabrication of *p*-Type ZnO. *Jpn. J. Appl. Phys.* **38**, L166–L169 (1999).

[53] Joseph, M., Tabata, H., and Kawai, T. p-type electrical conduction in ZnO thin films by Ga and N codoping. *Jpn. J. Appl. Phys.* **38**, L1205–L1207 (1999).

[54] Scanlon, D. O. and Watson, G. W. Undoped *n*-type Cu_2O: fact or fiction?. *J. Phys. Chem. Lett.* **1**, 2582–2585 (2010).

[55] Meyer, B. K. *et al*. Binary copper oxide semiconductors: From materials towards devices. *Phys. Status Solidi B* **249**, 1487–1509 (2012).

[56] Biccari, F. *Defects and Doping in* Cu_2O, PhD Thesis, Sapienza – University of Rome (2009).

[57] Nie, X., Wei, S.-H., and Zhang, S. B. First-principles study of transparent *p*-type conductive $SrCu_2O_2$ and related compounds. *Phys. Rev. B* **65**, 075111 (2002).

[58] Hodby, J. W., Jenkins, T. E., Schwab, C., Tamura, H., and Trivich, D. Cyclotron resonance of electrons and of holes in cuprous oxide, Cu_2O. *J. Phys. C, Solid State Phys.* **9**, 1429–1439 (1976).

[59] Shimada, H. and Masumi, T. Hall mobility of positive holes in Cu_2O. *J. Phys. Soc. Jpn.* **58**, 1717–1724 (1989).

[60] Lee, Y., Winkler, M. T., Siah, S. C., Brandt, R., and Buonassisi, T. Hall mobility of cuprous oxide thin films deposited by reactive direct-current magnetron sputtering. *Appl. Phys. Lett.* **98**, 192115 (2011).

[61] Seto, J. Y. W. The electrical properties of polycrystalline silicon films. *J. Appl. Phys.* **46**, 5247–5254 (1975).

[62] Nomura, K. *et al*. Carrier transport in transparent oxide semiconductor with intrinsic structural randomness probed using single-crystalline $InGaO_3(ZnO)_5$ films. *Appl. Phys. Lett.* **85**, 1993–1995 (2004).

[63] Lee, S., Nathan, A., Ye, Y., Guo, Y., and Robertson, J. Localized tail states and electron mobility in amorphous ZnON thin film transistors. *Sci. Rep.* **5**, 13467 (2015).

[64] Anderson, P. W. Absence of diffusion in certain random lattices. *Phys. Rev.* **109**, 1492–1505 (1958).

[65] Street, R. A. *Hydrogenated Amorphous Silicon* (Cambridge University Press, 2005).

[66] Lee, S. and Nathan, A. Localized tail state distribution in amorphous oxide transistors deduced from low temperature measurements. *Appl. Phys. Lett.* **101**, 113502 (2012).

[67] Han, S. and Flewitt, A. J. Analysis of the conduction mechanism and copper vacancy density in p-type Cu_2O thin films. *Sci. Rep.* **7**:5766 (2017).

[68] Mondal, S. and Bhattacharyya, S. R. Performance of a size-selected nanocluster deposition facility and *in situ* characterization of grown films by x-ray photoelectron spectroscopy. *Rev. Sci. Instrum.* **85**, 065109 (2014).

[69] Vopsaroiu, M., Thwaites, M. J., Rand, S., Grundy, P. J., and O'Grady, K. Novel sputtering technology for grain-size control. *IEEE Trans. Magn.* **40**, 2443–2445 (2004).

[70] Seshan, K. *Handbook of Thin Film Deposition Processes and Techniques*. (Elsevier Science, 2013).

[71] Plasma Quest Limited. Description of the HiTUS technology. Available on the Plasma Quest Limited web site at https://www.plasmaquest.co.uk/the-technology/.

[72] Li, F. M. *et al*. Low temperature (<100 °C) deposited p-type cuprous oxide thin films: Importance of controlled oxygen and deposition energy. *Thin Solid Films* **520**, 1278–1284 (2011).

[73] Chan, K. Y. and Teo, B. S. Effect of Ar pressure on grain size of magnetron sputter-deposited Cu thin films. *IET Sci. Meas. Technol.* **1**, 87–90 (2007).

[74] Myers, H. P. *Introductory Solid State Physics* (Taylor & Francis, 1997).

[75] HyperPhysics (Georgia State University). Bragg's Law. http://hyperphysics.phy-astr.gsu.edu/hbase/quantum/bragg.html/.

[76] Cullity, B. D., *Elements of X-Ray Diffraction*. 2nd edn. (Addison-Wesley, 1978).

[77] Mir, F. A. and Batoo, K. M. Effect of Ni and Au ion irradiations on structural and optical properties of nanocrystalline Sb-doped SnO_2 thin films. *Appl. Phys. A* **122**, 418 (2016).

[78] Fox, M. *Optical Properties of Solid* (Oxford, 2001).

[79] Mugwang'a, F. K., Karimi P. K., Njoroge W. K., Omayio O., and Waita, S. M. Optical characterization of copper oxide thin films prepared by reactive dc

magnetron sputtering for solar cell applications. *Int. J. Thin Film Sci. Tec.* **2**, 15–24 (2013).

[80] Sardela, M. *Practical Materials Characterization*, Chapter 2 (Springer, 2014).

[81] Mohemmed Shanid, N. A., Abdul Khadar M., and Sathe, V. G. Frohlich interaction and associated resonance enhancement in nanostructured copper oxide films. *J. Raman Spectrosc.* **42**, 1769–1773 (2011).

[82] Fan, H., Zou, B., Liu, Y., and Xie, S. Size effect on the electron phonon coupling in CuO nanocrystals. *Nanotechnology* **17**, 1099–1103 (2006).

[83] Petroff, Y., Yu, P. Y., and Shen, Y. R. Study of photoluminescence in Cu_2O. *Phys. Rev. B* **12**, 2488–2495 (1975).

[84] Yu, P. Y. and Shen, Y. R. Resonance Raman studies in Cu_2O. I. The phonon-assisted 1s yellow excitonic absorption edge. *Phys. Rev. B* **12**, 1377–1394 (1975).

[85] van der Pauw, L. J. A method of measuring specific resistivity and Hall effect of discs of arbitrary shape. *Philips Res. Repts* **13**, 1–9 (1958).

[86] National Institute of Standards and Technology (NIST). Resistivity and Hall Measurements. https://www.nist.gov/pml/engineering-physics-division/popular-links/hall-effect/resistivity-and-hall-measurements/.

[87] Keysight Technologies. Sheet resistance/resistivity measurement using a source/measurement unit (SMU) – Application Note. https://literature.cdn.keysight.com/litweb/pdf/5992-1329EN.pdf?id=2693341/.

[88] Sze, S. M. and Lee, M. K. *Semiconductor Devices: Physics and Technology* (Wiley, 2010).

[89] National Institute of Standards and Technology (NIST). The Hall Effect. https://www.nist.gov/pml/engineering-physics-division/popular-links/hall-effect/hall-effect/.

[90] Chen, C.-Y. and Kanicki, J. Origin of series resistances in a-Si:H TFTs. *Solid-State Electron.* **42**, 705–713 (1998).

[91] Hong, D., Yerubandi, G., Chiang, H. Q., Spiegelberg, M. C., and Wager, J. F. Electrical modeling of thin-film transistors. *Crit. Rev. Solid State Mater. Sci.* **33**, 101–132 (2008).

[92] Shockley, W. A unipolar "field-effect" transistor. Proc. IRE **40**, 1365–1376 (1952)

[93] Zaumseil, J. and Sirringhaus, H. Electron and ambipolar transport in organic field-effect transistors. *Chem. Rev.* **107**, 1296–1323 (2007).

[94] Swart, J. W. *Solid State Circuits Technologies* (Intech, 2010).

[95] Khakzar, K. and Lueder, E. H. Modeling of amorphous-silicon thin-film transistors for circuit simulations with SPICE. *IEEE Trans. Electron Devices* **39**, 1428–1434 (1992).

[96] Dosev, D., Ytterdal, T., Pallares, J., Marsal, L. F., and Iñíguez, B. DC SPICE model for nanocrystalline and microcrystalline silicon TFTs. *IEEE Trans. Electron Devices* **49**, 1979–1984 (2002).

[97] Servati, P., Striakhilev, D., and Nathan, A. Above-threshold parameter extraction and modelling for amorphous silicon thin-film transistors. *IEEE Trans. Electron Devices* **50**, 2227–2235 (2003).

[98] Meijer, E. J. *et al.* Scaling behavior and parasitic series resistance in disordered organic field-effect transistors. *Appl. Phys. Lett.* **82**, 4576–4578 (2003).

[99] Hamadani, B. H. and Natelson, D. Temperature-dependent contact resistances in high-quality polymer field-effect transistors. *Appl. Phys. Lett.* **84**, 443–445 (2004).

[100] van der Zaag, P. J., Verheijen, M. A., Yoon, S. Y., and Young, N. D. Explanation for the leakage current in polycrystalline-silicon thin-film transistors made by Ni-silicide mediated crystallization. *Appl. Phys. Lett.* **81**, 3404–3406 (2002).

[101] Greve, D. W. *Field Effect Devices and Application: Devices for Portable, Low-power, and Imaging Systems* (Prentice-Hall, 1998).

[102] Tuttle, G. Dept. of Electrical and Computer Engineering, Iowa State University. Contact resistance and TLM measurements. http://tuttle.merc.iastate.edu/ee432/topics/metals/tlm_measurements.pdf/.

[103] Christian-Albrechts-Universität zu Kiel (CAU). Silicon Based Micro- and Nanosystems. http://www.tf.uni-kiel.de/matwis/mpn/siegen.html/.

[104] Ytterdal, T., Cheng, Y., and Fjeldly, T. A. *Device Modeling for Analog and RF CMOS Circuit Design* (John Wiley & Sons, 2003).

[105] Sung, S.-Y. *et al*. Fabrication of p-channel thin film transistors using CuO active layers deposited at low temperature. *Appl. Phys. Lett*. **97**, 222109 (2010).

[106] Johan, M. R., Suan, M. S. M., Hawari, N. L., and Ching, H. A. Annealing effects on the properties of copper oxide thin films prepared by chemical deposition. *Int. J. Electrochem. Sci.* **6**, 6094–6104 (2011).

[107] Isah, K. U. *et al*. Effect of oxidation temperature on the properties of copper oxide thin films prepared from thermally oxidised evaporated copper thin films. *IOSR-JAP* **3**, 61–66 (2013).

[108] Pattanasattayavong, P., Thomas, S., Adamopoulos, G., McLachlan, M. A., and Anthopoulos, T. D. p-channel thin-film transistors based on spray-coated Cu_2O films. *Appl. Phys. Lett.* **102**, 163505 (2013).

[109] Sanal, K. C., Vikas, L. S., Jayaraj, M. K. Room temperature deposited transparent p-channel CuO thin film transistors. *Appl. Surf. Sci.* **297**, 153–157 (2014).

[110] Tauc, J. Optical properties and electronic structure of amorphous Ge and Si. *Mat. Res. Bull.* **3**, 37–46 (1968).

[111] Elliott, R. J. Intensity of Optical Absorption by Excitons. *Phys. Rev.* **108**, 1384–1389 (1957).

[112] Hosono, H. Ionic amorphous oxide semiconductors: Material design, carrier transport, and device application. *J. Non-Cryst. Solids* **352**, 851–858 (2006).

[113] Nomura, K. *et al*. Subgap states in transparent amorphous oxide semiconductor, In–Ga–Zn–O, observed by bulk sensitive x-ray photoelectron spectroscopy. *Appl. Phys. Lett.* **92**, 202117 (2008).

[114] Kamiya, T. and Hosono, H. Material characteristics and applications of transparent amorphous oxide semiconductors. *NPG Asia Mater*. **2**, 15–22 (2010).

[115] Shao, L., Nomura, K., Kamiya, T., and Hosono, H. Operation characteristics of thin-film transistors using very thin amorphous In–Ga–Zn–O channels. *Electrochem. Solid State Lett.* **14**, H197–H200 (2011).

[116] Kim, H. *et al*. Anion control as a strategy to achieve high-mobility and high-stability oxide thin-film transistors. *Sci. Rep.* **3**:1459 (2013).

[117] Ye, Y., Lim, R., and White, J. M. High mobility amorphous zinc oxynitride semiconductor material for thin film transistors. *J. Appl. Phys.* **106**, 074512 (2009).

[118] Shin, Y. *et al*. The mobility enhancement of Indium Gallium Zinc Oxide transistors via low-temperature crystallization using a Tantalum catalytic Layer. *Sci. Rep.* **7**:10885 (2017).

[119] Li, J., Vizkelethy, G., Revesz, P., Mayer, J. W., and Tu, K. N. Oxidation and reduction of copper oxide thin films. *J. Appl. Phys.* **69**, 1020–1029 (1991).

[120] Lee, S. Y., Mettlach, N., Nguyen, N., Sun, Y. M., and White, J. M. Copper oxide reduction through vacuum annealing. *Appl. Surf. Sci.* **206**, 102–109 (2003).

[121] Yu, J. *et al*. Solution-processed p-type copper oxide thin-film transistors fabricated by using a one-step vacuum annealing technique. *J. Mater. Chem. C* **3**, 9509–9513 (2015).

[122] Fortunato, E. *et al*. Erratum: "Thin-film transistors based on p-type Cu_2O thin films produced at room temperature." *Appl. Phys. Lett.* **96**, 239902 (2010).

[123] Jeong, C. *et al*. Investigation of the charge transport mechanism and subgap density of states in p-type Cu_2O thin-film transistors. *Appl. Phys. Lett.* **102**, 082103 (2013).

[124] Wang, Y. *et al*. Transmittance enhancement and optical band gap widening of Cu_2O thin films after air annealing. *J. Appl. Phys.* **115**, 073505 (2014).

[125] Han, S., Niang, K. M., Rughoobur, G., and Flewitt, A. J. Effects of post-deposition vacuum annealing on film characteristics of p-type Cu_2O and its impact on thin film transistor characteristics. *Appl. Phys. Lett.* **109**, 173502 (2016).

[126] Watakabe, H., Tsunoda, Y., Andoh, N., and Sameshima, T. Characterization and control of defect states of polycrystalline silicon thin film transistor fabricated by laser crystallization. *J. Non-Cryst. Solids* **299–302**, 1321–1325 (2002).

[127] Kim, S. *et al*. Relation between low-frequency noise and subgap density of states in amorphous InGaZnO thin-film transistors. *IEEE Electron Device Lett.* **31**, 1236–1238 (2010).

[128] Natsume, Y., Sakata, H., and Hirayama, T. Low-temperature electrical conductivity and optical absorption edge of ZnO films prepared by chemical vapour deposition. *Phys. Status Solidi A* **148**, 485–495 (1995).

[129] Ikhmayies, S. J. and Ahmad-Bitar, R. N. A study of the optical bandgap energy and Urbach tail of spray-deposited CdS:In thin films. *J. Mater. Res. Technol.* **2**, 221–227 (2013).

[130] Lany, S. Band-structure calculations for the 3*d* transition metal oxides in *GW*. *Phys. Rev. B* **87**, 085112 (2013).

[131] Nam, D. *et al*. Active layer thickness effects on the structural and electrical properties of p-type Cu_2O thin-film transistors. *J. Vac. Sci. Technol. B* **30**, 060605 (2012).

[132] Konenkamp, R. *Photoelectric Properties and Applications of Low-Mobility Semiconductors* (Springer, 2000).

[133] O'Leary, S. K., Johnson, S. R., and Lim, P. K. The relationship between the distribution of electronic states and the optical absorption spectrum of an amorphous semiconductor: An empirical analysis. *J. Appl. Phys.* **82**, 3334–3340 (1997).

[134] Lee, S., Ahnood, A., Sambandan, S., Madan, A., and Nathan, A. Analytical field-effect method for extraction of subgap states in thin film transistors. *IEEE Electron Device Lett.* **33**, 1006–1008 (2012).

[135] Sze, S. M. *Physics of Semiconductor Devices* (Wiley, 1981).

[136] Jackson, W. B. Connection between the Meyer-Neldel relation and multiple-trapping transport. *Phys. Rev. B* **38**, 3595–3598 (1988).

[137] Guo, D., Miyadera, T., Ikeda, S., Shimada, T., and Saiki, K. Analysis of charge transport in a polycrystalline pentacene thin film transistor by temperature and gate bias dependent mobility and conductance. *J. Appl. Phys.* **102**, 023706 (2007).

[138] Teresa, D. *et al*. Electrochemical deposition of copper(I) oxide films. *Chem. Mater*. **8**, 2499-2504 (1996).

[139] Wang, L. C., de Tacconi, N. R., Chenthamarakshan, C. R., Rajeshwar, K., and Tao, M. Electrodeposited copper oxide films: Effect of bath pH on grain orientation and orientation-dependent interfacial behavior. *Thin Solid Films* **515**, 3090–3095 (2007).

[140] Bijani, S. *et al*. Low-temperature electrodeposition of Cu_2O thin films: modulation of micro-nanostructure by modifying the applied potential and electrolytic bath pH. *J. Phys. Chem. C* **113**, 19482–19487 (2009).

[141] Wu, W., Feng, K., Shan, B., and Zhang, N. Orientation and grain shape control of Cu_2O film and the related properties. *Electrochimica Acta* **176**, 59–64 (2015).

[142] Wang, C. *et al*. Structural, optical and photoelectrical properties of Cu_2O films electrodeposited at different pH. *RSC Adv*. **6**, 4422–4428 (2016).

[143] Schulz, K. H. and Cox, D. F. Photoemission and low-energy-electron-diffraction study of clean and oxygen-dosed Cu_2O (111) and (100) surfaces. *Phys. Rev. B* **43**, 1610–1621 (1991).

[144] Tasker, P. W. The stability of ionic crystal surfaces. *J. Phys. C: Solid State Phys.* **12**, 4977–4984 (1979).

[145] Zheng, Z. *et al*. Crystal faces of Cu_2O and their stabilities in photocatalytic reactions. *J. Phys. Chem. C* **113**, 14448–14453 (2009).

[146] Banerjee, R., Chandra, R., and Ayyub, P. Influence of the sputtering gas on the preferred orientation of nanocrystalline titanium nitride thin films. *Thin Solid Films* **405**, 64–72 (2002).

[147] Wang, Y. *et al*. Tuning the structure and preferred orientation in reactively sputtered copper oxide thin films. *Appl. Surf. Sci.* **335**, 85–91 (2015).

[148] Hultman, L., Sundgren, J.-E., Greene, J. E., Bergstrom, D. B., and Petrov, I. High-flux low-energy (20 eV) N_2^+ ion irradiation during TiN deposition by reactive magnetron sputtering: Effects on microstructure and preferred orientation. *J. Appl. Phys*. **78**, 5395–5403 (1995).

[149] Gall, D., Kodambaka, S., Wall, M. A., Petrov, I., and Greene, J. E. Pathways of atomistic processes on TiN(001) and (111) surfaces during film growth: an ab initio study. *J. Appl. Phys*. **93**, 9086–9094 (2003).

[150] Petrov, I., Barna, P. B., Hultman, L., and Greene, J. E. Microstructural evolution during film growth. *J. Vac. Sci. Technol. A* **21**, S117–S128 (2003).

[151] Nesheva, D., Levi, Z., Aneva, Z., Nikolova, V., and Hofmeister, H. Experimental studies on the defect states at the interface between nanocrystalline CdSe and amorphous SiOx. *J. Phys.: Condens. Matter*. **12**, 751–759 (2000).

[152] Ahmad, S., Asokan, K., and Zulfequar, M. Investigation of structural and optical properties of 100 MeV F^{7+} ion irradiated $Ga_{10}Se_{90-x}Al_x$ thin films. *Philos. Mag.* **95**, 1309–1320 (2015).

[153] Microtech Systems, Inc. *SPM Photoresist Stripping and Cleaning*. (2007).

[154] Brown, A. R., Jarrett, C. P., de Leeuw, D. M., and Matters, M. Field-effect transistors made from solution-processed organic semiconductors. *Synth. Met.* **88**, 37–55 (1997).

[155] Horowitz, G., Hajlaoui, R., Fichou, D., and Kassmi, A. E. Gate voltage dependent mobility of oligothiophene field-effect transistors. *J. Appl. Phys.* **85**, 3202–3206 (1999).

[156] Dimitrakopoulos, C. D., Purushothaman, S., Kymissis, J., Callegari, A., and Shaw, J. M. Low-voltage organic transistors on plastic comprising high-dielectric constant gate insulators. *Science* **283**, 822–824 (1999).

[157] Jo, G. *et al*. Channel-length and gate-bias dependence of contact resistance and mobility for nanowire field effect transistors. *J. Appl. Phys.* **102**, 084508 (2007).

[158] Ahnood, A. *et al*. Non-ohmic contact resistance and field-effect mobility in nanocrystalline silicon thin film transistors. *Appl. Phys. Lett.* **93**, 163503 (2008).

[159] Sohn, J. *et al*. Effects of vacuum annealing on the optical and electrical properties of p-type copper-oxide thin-film transistors. *Semicond. Sci. Technol.* **28**, 015005 (2013).

[160] Park, J. *et al*. Source/drain series-resistance effects in amorphous Gallium–Indium Zinc-Oxide thin film transistors. *IEEE Electron Device Lett.* **29**, 879–881 (2008).

[161] Nag, M. *et al*. Single-source dual-layer amorphous IGZO thin-film transistors for display and circuit applications. *J. Soc. Inf. Disp.* **21**, 129–136 (2013).

[162] Mönch, W. On the physics of metal-semiconductor interfaces. *Rep. Prog. Phys.* **53**, 221–278 (1990).

[163] Kramm, B. *et al*. The band alignment of Cu_2O/ZnO and Cu_2O/GaN heterostructures. *Appl. Phys. Lett.* **100**, 094102 (2012).

[164] Horowitz, G., Lang, P., Mottaghi, M., and Aubin, H. Extracting parameters from the current-voltage characteristics of organic field-effect transistors. *Adv. Funct. Mater.* **14**, 1069–1074 (2004).

[165] Luan, S. and Neudeck, G. W. An experimental study of the source/drain parasitic resistance effects in amorphous silicon thin film transistors. *J. Appl. Phys.* **72**, 766–772 (1992).

[166] Zaumseil, J., Baldwin, K. W., and Rogers, J. A. Contact resistance in organic transistors that use source and drain electrodes formed by soft contact lamination. *J. Appl. Phys.* **93**, 6117–6124 (2003).

[167] Choyke, W. J., Matsunami, H., Pensl, G. *Silicon Carbide: Recent Major Advances*, Chap. 3 (Springer, 2004).

[168] Ryu, M. K., Yang, S., Park, S.-H. K., Hwang, C.-S., and Jeong, J. K. High performance thin film transistor with cosputtered amorphous Zn–In–Sn–O channel: Combinatorial approach. *Appl. Phys. Lett.* **95**, 072104 (2009).

[169] Kalb, W. L. and Batlogg, B. Calculating the trap density of states in organic field-effect transistors from experiment: A comparison of different methods. *Phys. Rev. B* **81**, 035327 (2010).

[170] Su, L.-Y. *et al*. Characterizations of amorphous IGZO thin-film transistors with low subthreshold swing. *IEEE Electron Device Lett.* **32**, 1245–1247 (2011).

[171] Berger, L. I. *Semiconductor Materials* (CRC Press, 1997).

[172] Choi, H. *et al*. Bias-dependent effective channel length for extraction of subgap DOS by capacitance–voltage characteristics in amorphous semiconductor TFTs. *IEEE Trans. Electron Devices* **62**, 2689–2694 (2015).

[173] Tsao, Y.-C. *et al*. Abnormal hump in capacitance–voltage measurements induced by ultraviolet light in a-IGZO thin-film transistors," *Appl. Phys. Lett.* **110**, 023501 (2017).

[174] Han, S. and Flewitt, A. J. The origin of the high off-state current in p-type Cu_2O thin film transistors. *IEEE Electron Device Lett.* **38**, 1394–1397 (2017).

[175] Jackson, W. B., Marshall, J. M., and Moyer, M. D. Role of hydrogen in the formation of metastable defects in hydrogenated amorphous silicon. *Phys. Rev. B* **39**, 1164–1179 (1989).

[176] Chen, C., Abe, K., Kumomi, H., and Kanicki, J. Density of states of a-InGaZnO from temperature-dependent field-effect studies. *IEEE Trans. Electron Devices* **56**, 1177–1183 (2009).

[177] Takechi, K., Nakata, M., Eguchi, T., Yamaguchi, H., and Kaneko, S. Temperature-dependent transfer characteristics of amorphous $InGaZnO_4$ thin-film transistors. *Jpn. J. Appl. Phys.* **48**, 011301 (2009).

[178] Zouaghi, M., Prevot, B., Carabatos, C., and Sieskind, M. Near infrared optical and photoelectric properties of Cu_2O. III. Interpretation of experimental results. *Phys. Status Solidi A* **11**, 449–460 (1972).

[179] Garuthara, R. and Siripala, W. Photoluminescence characterization of polycrystalline n-type Cu_2O films. *J. Lumin.* **121**, 173–178 (2006).

[180] Mott, N. F. Conduction in glasses containing transition metal ions. *J. Non-Cryst. Solids* **1**, 1–17 (1968).

[181] Mott, N. F. The effect of electron interaction on variable-range hopping. *Philos. Mag.* **34**, 643-645 (1976).

[182] van Hapert, J. J. *Hopping conduction and chemical structure: a study on silicon suboxides*, PhD Thesis, Utrecht University (2002).

[183] Rubinger, R. M. *et al*. Temperature-dependent activation energy and variable range hopping in semi-insulating GaAs. *Semicond. Sci. Technol.* **21**, 1681–1685 (2006).

[184] Kang, W. *et al*. Expedient floating process for ultra-thin InGaZnO thin-film-transistors and their high bending performance. *RSC Adv.* **6**, 63418–63424 (2016).

[185] Wang, W. *et al*. Analysis of the contact resistance in amorphous InGaZnO thin film transistors. *Appl. Phys. Lett.* **107**, 063504 (2015).